Modeling and Simulation of Ablation-Controlled Plasmas

by Madhusudhan N. Kundrapu

Bachelor of Technology in Mechanical Engineering, April 2002, Jawaharlal Nehru Technological University, India
Master of Technology in Mechanical Engineering-Thermal Sciences, August 2004, National Institute of Technology Calicut, India

A dissertation submitted to

The Faculty of
The School of Engineering and Applied Science
of The George Washington University
in partial fulfillment of the requirements
for the degree of Doctor of Philosophy

January 31, 2012

Dissertation Directed by

Michael Keidar
Associate Professor of Engineering and Applied Science

The School of Engineering and Applied Science of The George Washington University certifies that Madhusudhan N. Kundrapu has passed the Final Examination for the degree of Doctor of Philosophy as of November 10th, 2011. This is the final and approved form of the dissertation.

Modeling and Simulation of Ablation-Controlled Plasmas

Madhusudhan N. Kundrapu

Dissertation Research Committee:

Michael Keidar, Associate Professor of Engineering and Applied Science, Dissertation Director

Chunlei Liang, Assistant Professor of Engineering and Applied Science, Committee Member

Philippe M. Bardet, Assistant Professor of Engineering and Applied Science, Committee Member

John Loverich, Research Scientist, Tech-X Corporation, Committee Member

Yevgeny Raitses, Principal Research Scientist, Princeton Plasma Physics Laboratory, Committee Member

Dedication

To the ubiquitous inner self

Acknowledgments

I am fortunate to have Prof. Michael Keidar as my dissertation advisor. I consider him among the best people I have ever worked with. I am deeply indebted to him for his guidance and intellectual discussions throughout the course of this work. I am grateful to him forever.

I am very thankful to my dissertation committee members Prof. Chunlei Liang, Prof. Philippe Bardet, Dr. Yevgeny Raitses, and Dr. John Loverich, for reviewing this work. Their comments were very useful in improving the quality of this work.

I thank each and every faculty member of the Department of Mechanical and Aerospace Engineering for their course lectures, which played a key role in this research.

I thank all the people of MicroPropulsion and Nanotechnology Laboratory for their timely help. Special thanks to Dr. Alexey Shashurin and Jian Li for their discussions on experimental setup and providing me with experimental data used for validating simulations. I thank my colleague and friend Lubos Brieda for the extensive discussions on physics and scientific computing.

Finally, I take this opportunity to gratefully acknowledge the financial support of the Air Force Office of Scientific Research, National Scientific Foundation, Department of Energy, The George Washington University Fellowship, and Louis P. Wagman Engineering Endowment Fellowship.

Abstract

Modeling and Simulation of Ablation-Controlled Plasmas

Ablation and plasma formation in high energy laser target interactions and arc discharges are studied numerically. Each of the two processes is modeled separately due to the type of energy source and the resulting flow field. Ablation of the target material and plasma formation are coupled to obtain evaporation rate, temperature distribution, velocity field, and species concentration self-consistently.

Laser ablation is studied in the perspective of directed energy applications, where beam size varies from few centimeters to tens of centimeters with energies extending up to 10 kW/cm^2. Because of this high energy deposition, the evaporated material expands to supersonic speeds into the free space. Due to the large spot sizes and associated supersonic flow, one dimensional Euler equations are considered to be sufficient for modeling the plume. Instead, more emphasis was given to evaporation model, by introducing Knudsen layer kinetics at the plume target interface, and plasma shielding. The evaporation rate is validated with results from the experiments and simulations are carried out to find the influence of laser beam frequency on evaporation rates. The evaporation model used in this work is found to be more accurate than the widely used model based on sonic speed assumption. The optimum beam wavelength for Al surfaces is found to be 850 nm. Attenuation of telemetry data by plasma is a concern for the testing of directed energy systems. Electrostatic

approach for the mitigation of communication attenuation is analyzed to obtain the fluency limits up to which the approach can be implemented. It is found from sheath calculations that uninterrupted telemetry can be achieved through Al plasma for fluences below 4 J/cm^2 at a background pressure of 1 atm, using a maximum bias voltage of 10 kV.

Arc discharge ablation is modeled for the synthesis of nanoparticles. The electric arc generated between the electrodes, placed inside a Helium chamber, evaporates the catalyst-filled carbon anode to form a web of nanoparticles. Conservative form of Navier-Stokes equations along with energy equation and species transport are solved in cylindrical coordinates using SIMPLER algorithm. Current continuity in electric potential form is solved to obtain the potential distribution. Current is then calculated from the potential, and from axial current, magnetic field is obtained using Amperes law. Anode sublimation rate and current voltage characteristics are compared with experiments for arc currents varying from 10 to 100 A. Nanoparticle formation is estimated using homogeneous nucleation and surface diffusion models. For an arc current of 60 A and inter-electrode gap of 4 mm with 68 kPa, the diameter of nickel cluster is found to be 9.2 nm, which agrees with the upper limit of TEM measurements. The length of single walled nanotube is found to be 3.5 μm for this case. Parametric studies carried out by varying arc current, background pressure, and electrode gap showed moderate influence on the growth rate. Hot chamber arc discharge method, proposed in this work, is found to be promising to maximize the growth of nanoparticles.

Table of Contents

List of Figures

Figure

List of Tables

Table

Nomenclature

A	Absorptivity
a_0	inter-atomic distance (m)
C_a	fraction of neutrals
C_e	fraction of electrons
C_Z	fraction of ions of degree Z $(Z = 1, 2, ..., l)$
c	speed of light (m/s)
c_l	mass fraction of material in the vapor
	specific heat of liquid material $(J/(kgK))$
c_s	specific heat of solid material $(J/(kgK))$
$\bar{cp}$	average specific heat $(J/(kgK))$
$c_{p,m}$	specific heat of mixture $(J/(kgK))$
D_l	diffusion coefficient of material vapor l (m^2/s)
D_s	surface diffusion coefficient (m^2/s)
d_{np}	diameter of nanoparticle
$\mathbf{E}$	electric field (E_r, E_z, and E_θ are the components in cylindrical coordinates)
E_l	ionization energy of an atom of a material l (J)
E_Z	ionization energy of degree Z $(Z = 1, 2, ..., l)$
e	unit charge
	internal energy (J)
F	laser fluence (J/cm^2)
g	acceleration due to gravity (m/s^2)

h enthalpy (J/kg)

Planck's constant

I irradiance of laser beam before reaching plasma (W/cm^2)

total current of arc (A)

I_0 irrandiance of laser beam at target surface (W/cm^2)

j current flux vector (j_r, j_z, and j_θ are the components in cylindrical coordinates)

j_c flux of atoms contributing to the growth of nanoparticle $(1/m^2)$

j_{th} flux of electrons at the edge of anode sheath $(1/m^2)$

k imaginary part of index of refraction

kinetic constant of incorporation

thermal conductivity $(W/(mK))$

k_B Boltzmann constant (J/K)

L length of single walled nanotube (m)

L_m latent heat of melting (J/kg)

l length along a line (m)

M molecular weight

M_1 Mach number at the outer edge of Knudsen Layer

M_2 Mach number at the outer edge of Hydrodynamic Layer

m mass of atom (kg)

m_e mass of electron (kg)

m_i mass of ion (kg)

N number of atoms in a cluster

n number density $(1/m^3)$

real part of index of refraction

n_0 number density at the evaporating surface $(1/m^3)$

n_1 number density at the outer edge of Knudsen Layer $(1/m^3)$

n_a	number density of neutrals $(1/m^3)$
$n_{a,l}$	number density of neutrals of a material l $(1/m^3)$
n_e	number density of electrons $(1/m^3)$
$n_{e,max}$	peak density of electrons $(1/m^3)$
$n_{i,l}$	number density of ions of material l $(1/m^3)$
$n_{i,Z}$	number density of ions of ionization state Z $(1/m^3)$
n_{rc}	number density of critical clusters $(1/m^3)$
p	pressure (N/m^2)
p_a	pressure due to neutrals (N/m^2)
p_e	pressure due to electrons (N/m^2)
p_i	pressure due to ions (N/m^2)
p_{sat}	equilibrium pressure of material (N/m^2)
p_v	pressure of the vapor (N/m^2)
q	charge (C)
$\dot{q}$	volumetric heat (W/m^3)
Q	photon absorption cross section
Q_c	flux of carbon atoms $(1/m^2)$
Q_{laser}	laser energy (W/m^3)
Q_{Ni}	flux of nickel atoms $(1/m^2)$
R	gas constant $(J/(kgK))$
	radius of arc discharge chamber (m)
	Reflectivity
r	coordinate axis
	radius of nanoparticle (m)
r_a	radius of atom (m)
r_c	radius of critical cluster (m)
S	saturation ratio

s	electrostatic sheath thickness (m)
s_0	electrostatic sheath thickness calculated using Child-Langmuir relation (m)
T	temperature
T_0	surface temperature (K)
T_1	temperature at the outer edge of Knudsen Layer (K)
T_e	temperature of electron (K)
T_{intial}	initial temperature of target in laser ablation (K)
U	bias voltage (V)
U_a	anode sheath drop (V)
$\mathbf{u}$	velocity vector (u, v, and w are components along r, z, and θ directions in cylindrical coordinates)
$\mathbf{V}$	velocity vector used on Knudsen Layer (V_x, V_y, and V_z are the components along x, y, and z directions)
V_1	velocity at the edge of Knudsen Layer (m/s)
V_2	velocity at the outer edge of Hydrodynamic Layer (m/s)
V_a	atomic volume (m^3)
v_l	velocity along a line l (m/s)
v_{th}	thermal velocity (m/s)
z	coordinate axis

Greek Symbols

α	Absorption coefficient $(1/m)$
α_{e-i}	inverse Bremsstrahlung electron-ion absorption coefficient $(1/m)$
α_{e-n}	inverse Bremsstrahlung electron-neutral absorption coefficient $(1/m)$
α_{IB}	inverse Bremsstrahlung absorption coefficient $(1/m)$

β	coefficient corresponding to flux of return particle at Knudsen Layer outer edge
	ratio of deposition to evaporation of atoms
ΔG	Gibbs free energy of formation of spherical cluster
ΔG_c	Gibbs free energy of formation of critical cluster
δE_D	activation energy for surface diffusion (eV)
δ_{HL}	Hydrodynamic Layer thickness (m)
ε_0	permittivity of vacuum
ε_{rad}	re-radiation
ϕ_i	energy consumed in ionization (W/m^3)
ϕ_w	work function of anode material (eV)
Γ	rate of evaporation of mass flux $(kg/(m^2 s))$
γ	ratio of specific heats
η	coefficient to define the thickness of Hydrodynamic Layer
	effect of plasma flux on the growth of nanoparticle
φ	electric potential (V)
λ	wave length
λ_D	diffusion length (m)
λ_{De}	thickness of Debye sheath (m)
λ_{mf}	mean free path (m)
μ	dynamic viscosity (Ns/m^2)
μ_0	permeability of free space (H/m)
ν	frequency of laser beam $(1/s)$
	vibrational frequency of atoms $(1/s)$
$\nu_{e,a}$	electron-neutral collision frequency $(1/s)$
$\nu_{e,i}$	electron-Ion collision frequency $(1/s)$
ρ_l	density of a material l (kg/m^3)

σ	electrical conductivity (S/m)
	ionization cross section
	surface free energy
τ	shear stress (N/m^2)
τ_{inc}	incorporation time (s)
Ω	area of one carbon atom in SWNT

Abbreviations

DEW	Directed Energy Weapon
$DSMC$	Direct Simulation Monte Carlo
$FWHM$	Full Width Half Maximum
HL	Hydrodynamic Layer
KL	Knudsen Layer
LTE	Local Thermodynamic Equilibrium
MHD	Magneto Hydro-Dynamics
$MWNT$	Multi Wall Nanotube
nm	nanometer
ns	nanosecond
$SIMPLE$	Semi-Implicit Method for Pressure Linked Equations
$SIMPLER$	Semi-Implicit Method for Pressure Linked Equations Revised
$SWNT$	Single Wall Nanotube
TEM	Transmission Electron Microscope

Chapter I

Introduction

Ablation is defined as the departure of material, from the solid, in vapor phase due to phase transition of the former at high temperatures. When an external energy source is used to raise the temperature of the target, the temperature of the vapor is often, high enough to dissociate molecules to atoms and ionize the atoms. The ionized gas with a property to conduct electric current is known as plasma. As shown in Figure 1.1, plasma along with neutral vapor, influence the energy deposition to target, which in turn influence the evaporation rate and subsequent formation of plasma. Hence, it is a coupled problem. This phenomenon is observed in several cases such as reentry bodies, directed energy, and arc discharges.

Knowledge of various parameters such as, evaporation rate, temperature distri-

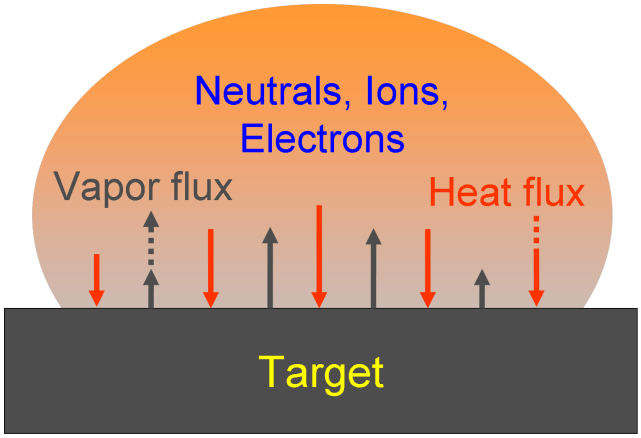

Figure 1.1: Schematic of ablation controlled plasma.

bution, species density, and velocity field are required for system design. Since it is very difficult to directly measure these parameters during experiments and testing, numerical simulation is essential. The numerical simulation should couple target ablation and plasma formation to obtain the evaporation rate and plasma parameters self-consistently.

In this dissertation, two problems in which ablation plays a crucial role are considered: laser target interaction and arc discharges. For these cases, the energy sources for evaporation are high energy laser beam and arc current respectively. Laser ablation is studied in the perspective of directed energy applications, while arc discharge ablation is modeled for the synthesis of nanoparticles.

1.1 Laser Ablation for Directed Energy Applications

The schematic of laser ablation is shown Fig. 1.2. Laser beam is directed on to a target to melt and evaporate the same.

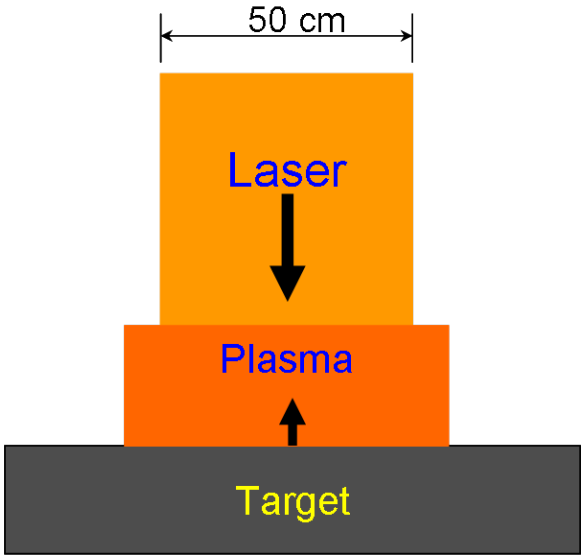

Figure 1.2: Schematic of laser ablation.

Directed energy weapon (DEW) systems use concentrated electromagnetic radiation in order to disable or destroy a stationary or moving target. The DEW and/or

target may be located on the ground, in the air, or in space. Development and testing of DEWs involve the evaluation of the effect of weapons on the target and the assessment of defensive capabilities of the target.[1] If the energy beam wavelength is in the range of few nanometers to a micrometer, then the weapons are categorized under laser-based DEW. The laser beam diameter can be as large as 50 cm, with power ranging from several kilowatts to gigawatts per square centimeter. The power characteristics of the beam, such as fluence and duration, depend on the type of target and objectives of the mission. The target and/or weapon can be stationary, low speed, or high speed and located on ground, in the air, or in space. The mission objectives may be to (1) temporarily disable or permanently damage the targets optronic sensors and radio communication devices or (2) destroy the target completely. If the weapon-target engagement duration is long enough, as in the case of stationary targets, low-energy lasers can be used to heat the target continuously. For instance, a laser pulse of 1 ms with 5 kJ of energy was used to destroy an optronic device located at a distance of 2 km and blind the same located 7 km away.[2] For targets such as missiles, which have a shorter duration of engagement, short pulses with high energy fluence are employed to fulfill the mission objectives.

When a laser beam is directed from the weapon onto a distant target, large amount of beam energy is lost due to several effects, such as (1) atmospheric attenuation (absorption, turbulence, scattering, and thermal blooming),[3] (2) plasma shielding near the target, and (3) surface reflectivity of target.[4] The atmospheric attenuation follows Beers law, and the attenuation coefficient depends on laser beam wavelength (λ).[5] Absorption of irradiance in plasma near the target surface, known as plasma shielding, is mainly due to inverse Bremsstrahlung electron-neural and electron-ion processes.[6;7] Because, inverse Bremsstrahlung coefficients α_{e-n} and α_{e-i} are functions of wavelength, the absorption of energy by plasma depends on wavelength. Besides this, the target surface reflectivity increases with wavelength,[8] which decreases the

amount of energy absorbed by a target. Laser ablation of a Cu target showed that shorter wavelength results in a better ablation rate.[9] It is also observed that plume length increases with wavelength.[10] Because all the processes in laser ablation are strongly coupled, a detailed numerical analysis is required to investigate the dependency of ablation rate on wavelength.

By obtaining the wavelength for which ablation rates are maximum, the kill performance of the DEW can be improved with less beam energy. On the other hand, if the objective is to defend a target, one can choose a suitable surface coating that minimizes the ablation rate. Measurements made for laser beam propagation in air at sea level over a distance of 1,800 m showed that several atmospheric windows (λ for which attenuation is low) are available in the wavelength range of 0.3–15 μm.[11;5] However, the ablation rates are expected to be high at low wavelengths due to low surface reflectivity. So, in this work 193–1064 nm wavelength range is considered to carry out a detailed numerical analysis for finding the dependency of ablation rate on wavelength. Because the material response, in terms of evaporation and surface properties, varies differently with wavelength and fluence, three different materials, Al, Cu, and Ti, are considered for the analysis with a wide fluence range of 10–100 J/cm^2.

One of the major tasks in the design of DEWs is to choose the beam parameters such as energy fluence to destroy a particular type of target. The duration of engagement is very short for direct observations; hence a continuous telemetry has to be established from the test bed to track the parameters such as temperature history. But the telemetry is often interrupted by the plasma shroud existing around the target. If the plasma frequency exceeds the radio wave frequency, then significant attenuation occurs. Though there is a possibility of isolating an antenna from plasma (by locating it away from ablation spot), this is not guaranteed for all encounters, in particular for the spinning and small flying targets such as missiles. Besides this, if

the goal is to defend the target's communication devices, then one has to consider the options to mitigate the attenuation of radio waves.

Several approaches have been suggested to mitigate this communication attenuation.[12;13;14;15] The most suitable approaches among those are electromagnetic and electrostatic. The electromagnetic approach employs an $E \times B$ layer in the plasma to accelerate plasma in a direction normal to the evaporating surface and away from it. The density of plasma decreases above the layer, and hence plasma frequency also decreases. By choosing suitable values for the electric and magnetic fields, the plasma frequency can be reduced below that of radio waves. The electrostatic approach involves the introduction of a negatively biased electrode to create an electron-depleted sheath within the plasma. The advantage of the latter approach is design simplicity, and it eliminates almost all the electrons within the sheath. On the other hand, this study can also be used to specify the laser fluence to create a plasma shroud, around the antenna of enemy target, with electron density sufficient enough to interrupt communication.

1.2 Arc discharge synthesis of nanoparticles

Arc discharge is one the three popular methods used for the synthesis of nanoparticles, while the other two methods being laser ablation and chemical vapor deposition. Figure 1.3 shows the schematic of arc discharge setup used for the synthesis of nanoparticles. Helium filled cylindrical chamber consists of cathode and hollow anode made up of graphite. The hollow anode is filled with Nickel, Carbon, and Yttrium powders. The electrodes are connected to an external DC power source and when the gap between the electrodes is sufficient enough, an arc is generated. The arc heats and eventually sublimates the anode material. Temperatures in the arc region are high enough to ionize the vapor, which in turn sustains the arc. The vapor particles of different species combine together to form nanoparticles. These nanoparticles appear

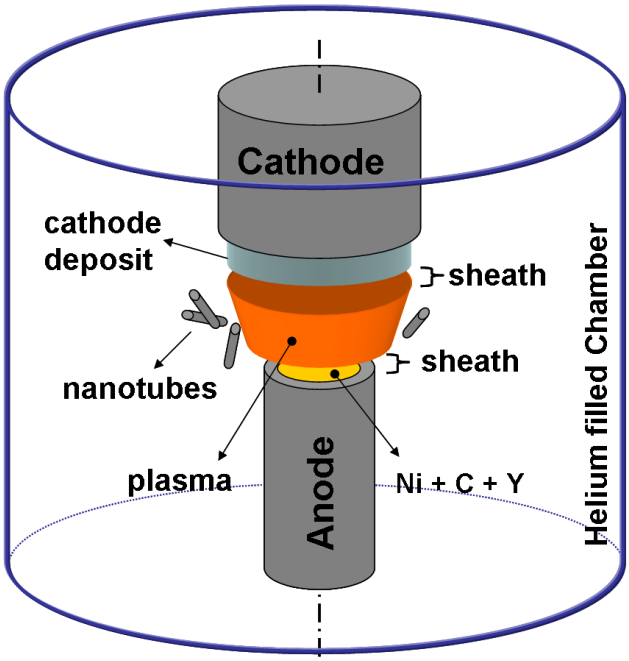

Figure 1.3: Arc discharger chamber for nanoparticle synthesis

as a web and precipitate on the electrode and chamber walls. Constant pressure is maintained throughout the process. In general, these clusters appear as spherical, tubular and planar shapes in varying sizes. The larger tubular clusters are known as nanotubes. Out of these carbon clusters, nanotubes are given with prime importance due to their superior thermo-mechanical[16] and electrical[17;18] properties and eventual industrial applications.[19;20;21] Besides nanotubes, graphene is also produced under the influence of external magnetic field in arc discharges.[22;23] Though arc discharge is the first method used for the synthesis of carbon nanoparticles[24], cheaper[25], and has the capability to produce nanotubes with fewer topological defects,[26;27] this method has lesser controllability. In order to improve the controllability, a comprehensive understanding of the growth mechanism of nanoparticles, in arc discharges, is required. Numerical models to estimate the size of nanoparticles should be developed and parametric studies have to be carried out to obtain the controllability.

General modeling aspects of ablation controlled plasma are given in Chapter-2, which consists of an overview of the models used for target heating, evaporation

rate, flow expansion, species transport, and ionization to simulate ablation controlled plasmas self-consistently. It can be well understood from Sections 1.1 and 1.2 that, the type and magnitude of heat source used for ablation in laser-target interaction and arc discharge are different. So, the general modeling equations are tailored to obtain two separate self-consistent models which are given in Chapter-3 for laser ablation and Chapter-4 for arc discharges. In addition to this, in Chapter-3, numerical simulations are carried out to obtain optimum beam wavelength for target evaporation and the feasibility of electrostatic sheath in high energy laser ablation is studied. In Chapter-4, surface flux balance and continuum surface diffusion models suitable to estimate the size of nanoparticles in dynamic plasmas, are added and parametric studies are carried out. Conclusions are given in Chapter-5 followed by Future work, Appendices and Bibliography.

Chapter II

Modeling Aspects

The complete mathematical model for ablation controlled plasmas should address target heating, evaporation rate, vapor expansion into the background, plasma formation, electromagnetic field, heat source evaluation, chemical reactions, and species transport.

2.1 Target heating

It is known that during the ablation process, target material exists in both solid and liquid phases. So, the model should account for phase change and the variations in thermophysical properties. It is not straightforward to define solid-liquid interface, so heat diffusion equation in enthalpy form (Eq. (2.1)) is considered.

$$\frac{\partial(\rho h)}{\partial t} = \nabla \cdot \left(k \nabla \left(\frac{h}{c_p} \right) \right) + \dot{q} \tag{2.1}$$

where h, t, k, and c_p are enthalpy, time, thermal conductivity, and specific heat respectively. The final term, $\dot{q}$, is volumetric heat source.

2.2 Ablation model

The schematic of ablation is shown in Fig. 2.1. In between target and vapor plume, there exists a very thin discontinuity layer called Knudsen Layer (KL). Vapor particles in this region undergo strong collisions and some will escape to the vapor plume while the remaining particles bounce back to the target surface. The velocity distribution of particles transform from half Maxwellian at the solid surface to shifted Maxwellian at the outer edge of KL. The region in the plume adjacent to KL consists of weakly ionized and thermally non-equilibrium plasma. The behavior of vapor particles in this region is more or less similar to neutrals and this region is known as Hydrodynamic Layer (HL).[28] Beyond this point in the plume, vapor is strongly ionized and attains electron-neutral thermal equilibrium. Three models are used widely to estimate the ablation rate: a) Langmuir model, b) Knudsen layer sonic speed model, and c) Knudsen layer self-consistent model.

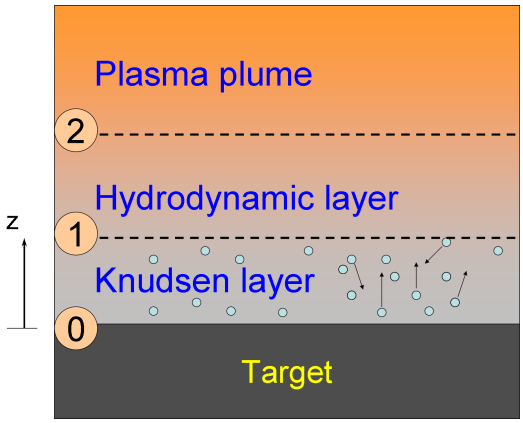

Figure 2.1: Kinetics at the evaporating surface.

2.2.1 Langmuir model

Mass flux rate is obtained by the product of mean velocity of evaporated particles in the normal direction to the surface and their half space density existing at the saturation pressure of the material.[29] It is given by Eqn. (2.2). Here, the back flux of

vapor from the Knudsen layer is not considered.

$$\Gamma = p_0 \left(2\pi R T_0 / M\right)^{-1/2} \tag{2.2}$$

where, Γ, p_0, R, T_0, and M are mass flux rate, vapor pressure, gas constant, surface temperature, and molecular weight respectively.

2.2.2 Knudsen layer sonic speed model

The velocity distribution of vapor particles at the evaporating surface can be given by half Maxwellian. For an arbitrary velocity V_1, the vapor parameters at the outer edge of KL can be obtained using Anisimov's assumption. It states that velocity distribution of returned particles is $\beta f_1(\mathbf{V})$. Where, β is proportionality coefficient and $f_1(\mathbf{V})$ is Maxwellian distribution function shifted by V_1. The distribution functions are given in Eqs. (2.3) and (2.4).[30;31] It has to be noted that the Maxwellian distribution functions are normalized and subscript x, and y correspond to the evaporation plane coordinates.

$$f_0(\mathbf{V}) = \begin{cases} n_0 \left(\frac{m}{2\pi k_B T_0}\right)^{3/2} exp\left(-\frac{mV^2}{2k_B T_0}\right) & for V_z > 0 \\ \beta f_1(\mathbf{V}) & for V_z < 0 \end{cases} \tag{2.3}$$

$$f_1(\mathbf{V}) = n_1 \left(\frac{m}{2\pi k_B T_1}\right)^{3/2} exp\left(-m\frac{V_x^2 + V_y^2 + (V_z - V_1)^2}{2k_B T_1}\right) \tag{2.4}$$

The DSMC simulation of Knudsen layer clearly shows the shift in velocity distribution as the vapor moves in normal direction to the target surface.[31]. This shift in velocity distribution is shown in Fig. 2.2. Distribution function is plotted at $x = 0$, 5λ, 25λ, and 100λ. In this figure, x is distance along the normal direction to the

evaporating surface, λ is mean free path. The velocity V_1 is about sonic speed.

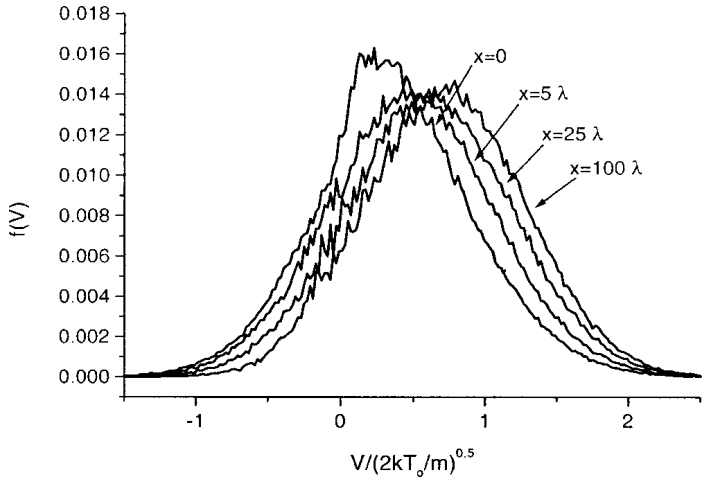

Figure 2.2: Velocity distribution function in Knudsen layer[31] obtained using DSMC simulation.

The governing equations in Knudsen layer for mass, momentum, and energy conservation can be obtained by integrating the Eqs. (2.3) and (2.4). across the Knudsen layer.

$$\frac{n_0}{2\left(\pi d_0\right)^{0.5}} = n_1 V_1 + \beta \frac{n_0}{2\left(\pi d_0\right)^{0.5}} \left\{ exp\left(-\alpha_{KL}^2\right) - \alpha_{KL}\pi^{0.5} erfc\left(\alpha_{KL}\right) \right\} \tag{2.5}$$

$$\frac{n_0}{4d_0} = \frac{n_1}{2d_1} \left\{ \left(1 + 2\alpha_{KL}^2\right) - \beta \left[\left(0.5 + \alpha_{KL}^2\right) erfc\left(\alpha_{KL}\right) - \alpha_{KL} exp\left(-\alpha_{KL}^2\right) / \pi^{0.5} \right] \right\} \tag{2.6}$$

$$\begin{aligned} \frac{n_0}{\left(\pi d_0\right)^{1}.5} = \frac{n_1}{\left(d_1\right)^{1}.5} \pi^{-1} \{ & \alpha_{KL}\left(\alpha_{KL}^2 + 2.5\right) - 0.5\beta \left[\left(2.5 + \alpha_{KL}^2\right) \alpha_{KL} erfc\left(\alpha_{KL}\right) \right. \\ & \left. - \left(2 + \alpha_{KL}^2\right) exp\left(-\alpha_{KL}^2\right) / \pi^{0.5} \right] \} \end{aligned} \tag{2.7}$$

where, $V^2 = {V_x}^2 + {V_y}^2 + {V_z}^2$, $d_0 = m/2k_BT_0$, $d_1 = m/2k_BT_1$, and $\alpha_{KL}^2 = V_1^2/\left(2k_BT_1/m\right)$.

But, the velocity of the vapor at the outer edge of Knudsen layer is not known a priori. This velocity is assumed to be sonic, especially for evaporation into vacuum. If the velocity, V_1 is sonic i.e. $V_1 = \sqrt{\gamma RT}$, the equations can be solved to obtain, n_1 and T_1 in terms of n_0 and T_0.[32] Which gives the values: $\beta = 6.29$, $n_1 = 0.31n_0$, $T_1 = 0.67T_0$

2.2.3 Knudsen layer self-consistent model

The velocity at the outer edge of Knudsen layer is obtained from the Hydrodynamic layer.[28] Subscript 2 is at the outer edge of HL.

$$n_1 V_1 = n_2 V_2 \tag{2.8}$$

$$n_1 k_B T_1 + m n_1 V_1^2 = n_2 k_B T_2 + m n_2 V_2^2 \tag{2.9}$$

$$\alpha_{KL}^2 = V_1^2 / \left(2k_B T_1/m\right) = \left(T_2 n_2 / 2T_1 - n_1/2\right) / \left(n_1 - n_1^2/n_2\right) \tag{2.10}$$

2.3 Fluid model for Plasma

Ideally, for continuum flows, a separate transport model should be used for individual species and Maxwell equations for electromagnetic field. This is known as magneto-hydrodynamic (MHD) description. However, for simplicity and without losing much of accuracy, plasma transport can be described using single fluid MHD equations.[33]

$$\frac{\partial \rho}{\partial t} + \nabla \cdot (\rho \mathbf{u}) = 0 \tag{2.11}$$

$$\frac{\partial(\rho\mathbf{u})}{\partial t} + \nabla\cdot(\rho\mathbf{u}\mathbf{u}) = -\nabla p + \nabla\cdot(\mu\nabla\mathbf{u}) + \rho\mathbf{g} + \mathbf{j}\times\mathbf{B} \tag{2.12}$$

where, $p = p_a + p_i + p_e$, the sum of partial pressures of neutrals, ions, and electrons respectively.

$$\mathbf{E} + \mathbf{u}\times\mathbf{B} = \frac{\mathbf{j}}{\sigma} \tag{2.13}$$

$$\frac{\partial q}{\partial t} + \nabla\cdot\mathbf{j} = 0 \tag{2.14}$$

$$\frac{\partial(\rho h)}{\partial t} + \nabla\cdot(\rho\mathbf{u}h) = \frac{Dp}{Dt} + \nabla\cdot\left(k\nabla\left(\frac{h}{c_p}\right)\right) + \dot{q} \tag{2.15}$$

2.4 Ionization

The ionization of atoms is mainly due to exchange of energy between atoms and fast moving electrons through direct collisions and radiation. The individual influence of collision and radiation processes varies depending on the density of plasma. Ionization and recombination in high density plasmas is dominated by collisional processes while in low density plasmas, radiative processes influence significantly. The ionization fractions can be obtained using rate equations for individual reactions as given in Eq. (2.16). The main difficulty in using rate equations is finding the ionization and recombination constants S_{ac} and S_{ca}, besides the computational intensity.

$$\frac{dn_e}{dt} = n_e n_a S_{ac} - {n_e}^2 n_i S_{ca} \tag{2.16}$$

Fortunately, the plasma in high energy laser ablation and arc discharges is dense enough and dominated with collisions, to treat it as LTE plasma. Hence, solution of individual rate equations can be avoided and Saha equation (Eq. (2.17))can be used

to find out the density of ions and neutrals. More details are given in Appendix B

$$\frac{n_e n_{i,l}}{n_{a,l}} = \left(\frac{2\pi m_e k_B T_e}{h^2}\right)^{3/2} exp\left(-\frac{E_l}{k_B T_e}\right) \tag{2.17}$$

2.5 Species transport

Solving mass, momentum and energy equation for each of the individual species is tedious. Instead, by assuming zero slip velocity (valid for high density gases), the mass fraction of species can be considered as scalar variable and it can be obtained using Eq.(2.18).

$$\frac{\partial\left(\rho c_l\right)}{\partial t} + \nabla \cdot \left(\rho \mathbf{u} c_l\right) = \nabla \cdot \left(D_l \nabla\left(\rho c_l\right)\right) \tag{2.18}$$

$$c_l = \frac{\rho_l}{\sum_{i=1}^{l} \rho_i}$$

2.6 Thermophysical properties

Thermophysical properties of material vary with temperature. The variation can be obtained from kinetic theory or experiments. In this work, the variations are considered from literature. Again, when single fluid approach is used, the properties of the mixture is obtained by averaging the individual species properties at a given temperature. The properties can be averaged using mole fractions or mass fractions, depending on the property under consideration as shown in Eq. (2.19).

$$k = \sum_i k_i x_i \quad , \quad \mu = \sum_i \mu_i x_i$$

$$c_p = \sum_i c_{p_i} c_i \quad , \quad M = \frac{1}{\sum_i c_i / M_i}$$

$$x_j = \frac{\rho_j / M_j}{\sum_{i=1}^{l} \rho_i / M_i} \quad , \quad i = 1, 2, 3, ..l; j = 1, 2, 3, ..l \tag{2.19}$$

Coming back to the two specific cases of study, further simplifications are applicable based on the type of energy source and resulting flow field. These simplifications are given in Chapter 3 for laser ablation and Chapter 4 for arc discharge ablation along with the solution technique and results.

Chapter III

Laser ablation

Laser ablation is studied in the perspective of directed energy applications, where beam size varies from few centimeters to tens of centimeters with energies extending up to 10 kW/cm^2. Because of this high energy deposition, the evaporated material expands to supersonic speeds into the free space. Due to large spot sizes and the associated supersonic flow, one dimensional Euler equations are considered to be sufficient for modeling the plume. Instead, more emphasis was given to evaporation model, by introducing Knudsen layer kinetics at the plume target interface, and plasma shielding.

For most of the applications, laser beam energy is directed in pulses. Typical pulse shape is shown in Fig. 3.1. The pulse specifications are full width half maximum ($FWHM$), total pulse duration, and energy fluence (F). The irradiance at the laser source (I_0) can then be estimated from F, using Eq.(3.1).

$$I_0(t) = \frac{F}{\sqrt{\pi} t_0} exp\left[-(t - t_m)^2 / 2t_0^2\right] \tag{3.1}$$

where, $t_0 = \frac{FWHM}{2\sqrt{2ln(2)}}$

One of the interesting and important aspects of laser ablation is plasma shielding. While on its way to target surface, some portion of laser irradiance is absorbed by the expanding plasma plume. This absorbed energy causes further increase in plasma

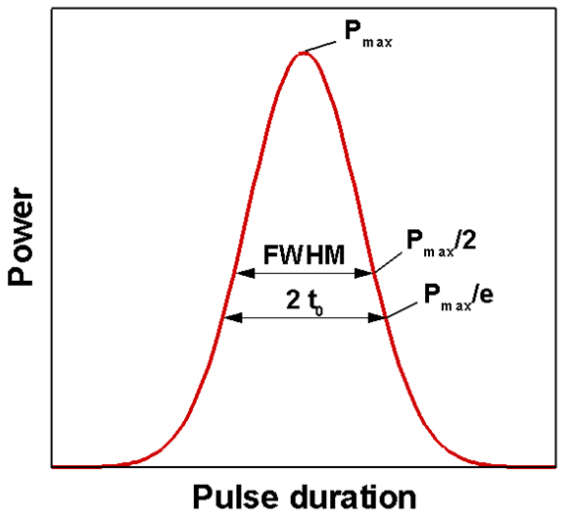

Figure 3.1: power distribution in a typical laser pulse.

temperature which results in stronger ionization. With a fluence of about 100 J/cm^2, charge states of 8^+ and ion temperatures of 370 eV have been observed for 1064 nm 9 ns laser ablation of tantalum targets under vacuum conditions.[34]

3.1 Mathematical model

The mathematical model for laser ablation is deduced from the general model given in Chapter 2.

3.1.1 Target

The heat conduction equation Eqn.(2.1) can be used with heat source term corresponding to the laser energy absorbed by target. Enthalpy in all cells is obtained and temperature is then calculated using Eqn. (3.2).[35]

$$\begin{aligned} T &= h/c_s, & h &\leq c_s T_m \\ T &= T_m, & c_s T_m < h &< c_s T_m + L_m \\ T &= T_m + (h - c_s T_m - L_m)/c_l, & h &\geq c_s T_m + L_m \end{aligned} \tag{3.2}$$

where, c and L are specific heat and latent heat; suffixes s, l and m correspond to solid, liquid and molten states respectively. Laser energy at any spatial location and time is given by Eqn.(3.3). α is absorption coefficient which is considered constant for target material and varies with time and space for plume. $I(z,t)$ is laser irradiation which also varies with time and space and is evaluated using Eqn. (3.4). A is absorptivity of material.

$$Q_{laser}(z,t) = \alpha I(z,t) \tag{3.3}$$

$$I(z,t) = AI_0(t)\, exp\left(-\int_0^z \alpha dz\right) \tag{3.4}$$

3.1.2 Ablation

The Knudsen-layer sonic model and self-consistent model given in Chapter 2 (Eqs.(2.5)–(2.7) and (2.8)–(2.10)) can be used to calculate the evaporation rate. Vapor pressure at the target surface for Al metal given by Eqn.(3.5)[36] is considered for the present study. p_0 and T_0 are vapor pressure and temperature at the target surface. The number density at the surface n_0 can be obtained from the relation $p_0 = n_0 k_B T_0$.

$$log_{10}(p_0) = 11.60 - 15880/T_0 \tag{3.5}$$

3.1.3 Plume

Conservation of mass, momentum, energy and equation of state for plasma bulk are given by Eqs. (3.6)–(3.9) respectively. The terms on right hand side of Eqn. (3.8) account for laser irradiation absorbed by plasma, energy consumed in ionization and energy re-radiated from plasma. First term is treated as source while other two are sinks.[37]

$$\frac{\partial \rho}{\partial t} + \frac{\partial(\rho v)}{\partial z} = 0 \tag{3.6}$$

$$\frac{\partial(\rho v)}{\partial t} + \frac{\partial(p + \rho v^2)}{\partial z} = 0 \tag{3.7}$$

$$\frac{\partial\left[\rho\left(e + \frac{v^2}{2}\right)\right]}{\partial t} + \frac{\partial\left[\rho v\left(e + \frac{p}{\rho} + \frac{v^2}{2}\right)\right]}{\partial z} = \alpha_{IB}(z,t)\, I(z,t) - \phi_I(z,t) - \varepsilon_{rad}(z,t) \tag{3.8}$$

$$p = (1 + C_e)\frac{\rho k_B T}{m} \tag{3.9}$$

Since plasma bulk is in thermal equilibrium, Saha equation (Eqn.(3.10)) is used to find the concentration of species. C is ionization fraction, suffixes e and Z stand for electron and degree of ionization. E is ionization energy and h is Plancks constant. Highest state of ionization considered in this study is 3 and the reason for this assumption will be justified at the end of section 3.2.1.

$$\frac{C_e C_Z}{C_{Z-l}} = \frac{1}{n}\left(\frac{2\pi m_e k_B T_e}{h^2}\right)^{3/2} exp\left(-\frac{E_Z}{k_b T}\right) \tag{3.10}$$

$C_1 + C_2 + C_3 = 1$

$C_1 + 2C_2 + 3C_3 = C_e$

Absorption coefficient, α_{IB} in Eqn. (3.8), is given by summation of electron-neutral and electron-ion inverse Bremsstrahlung absorption coefficients i.e. $\alpha_{IB} = \alpha_{e-n} + \alpha_{e-i}$

$$\alpha_{e-n} = \left[1 - exp\left(-\frac{hc}{\lambda k_B T}\right)\right] Q n_e n_0 \tag{3.11}$$

$$\alpha_{e-i} = \left[1 - exp\left(-\frac{hc}{\lambda k_B T}\right)\right] \frac{4e^6 \lambda^3 n_e}{3hc^4 m_e}\left(\frac{2\pi}{3 m_e k_B T}\right)^{0.5} \sum_Z Z^2 n_{i,Z} \tag{3.12}$$

where, λ and c are wavelength of laser and velocity of light and Q is photon absorption

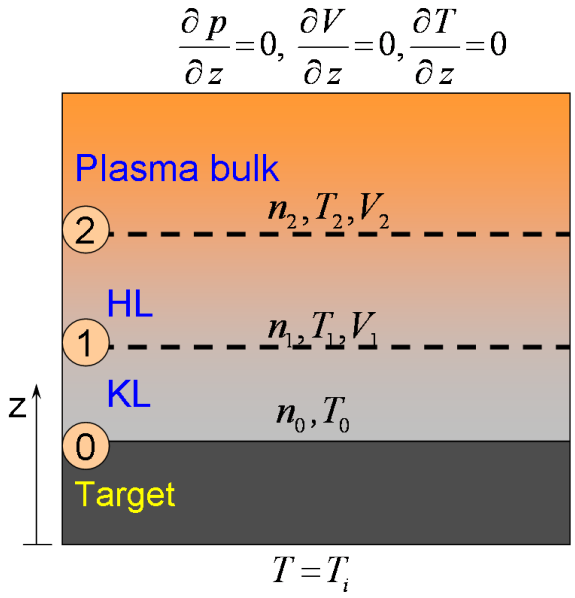

Figure 3.2: Laser ablation boundary conditions.

cross section. Third mechanism of absorption, photo-ionization is not considered in the present model. It is observed that, contribution of this third mechanism to the overall absorption coefficient is relatively less and decreases with the increase of laser fluence.[9] Energy consumed in ionization,$\phi_I(z,t)$ is given by Eqn. (3.13) in which $n_{i,Z}$ is ion density.

$$\phi_I(z,t) = n_{i,1}E_1 + n_{i,2}(E_1+E_2) + n_{i,3}(E_1+E_2+E_3) \tag{3.13}$$

where, E_1, E_2, and E_3 are first, second and third ionization energies. Final term of Eqn. (3.8), Energy re-radiated from plasma, ε_{rad} is given by Bremsstrahlung irradiance Eqn. (3.14).

$$\varepsilon_{rad} = \left(-\frac{2\pi k_B T}{3m_e}\right)\frac{32\pi e^6}{3hc^3 m_e} n_e \sum_Z Z^2 n_{i,Z} \tag{3.14}$$

3.2 Numerical solution procedure

The above mentioned equations are divided into three domains: target, KL and plasma bulk. At any point of time, all the three domains need information from each other and the equations representing these domains are highly non-linear. The situation demands both local as well as global convergence. So each of the three sets of equations are solved iteratively, initially to achieve local and then global convergence. Forward Euler scheme is used for target (Eqs. (2.1), (3.2)) and material properties are evaluated using the temperature distribution of previous local iteration. Equations (2.5)–(2.9) and (2.10) can be reduced to quadratic form in terms of unknowns. The roots of these quadratic equations are obtained with initial guess and then updated iteratively to obtain n_1, V_1, and T_1. Properties at target surface n_0 and T_0 are obtained using Eqn. (3.5) while the information prevailing at HL outer edge, n_2, V_2, and T_2 corresponding to the current global iteration is considered. Now, set of Eqs. (3.6)-(3.8) representing HL and plasma bulk are solved with the boundary values n_1, V_1, and T_1. In order to account for the variation in δ_{HL}, a moving interface is considered between HL and plasma bulk. The governing equations are solved using Godunov scheme. Inter-cell fluxes are estimated using $HLLC$ Riemann solver with hybrid-pressure based wave speeds.[38] The details of the scheme and validation of the fluid solver are given in Appendix B. Finally, ionization fractions are evaluated using Eqn. (2.17), which is solved by Newton-Raphson iterative method. Source and sink terms in the energy equation ((3.8)) are then obtained using species concentrations.

3.2.1 Numerical simulation of HL

Knowledge of the thickness of the hydrodynamic layer, δ_{HL}, is required to find properties at HL outer edge which influence the flow properties in KL and also to know the region of thermal equilibrium in the plume. A coefficient η, is introduced to define thickness of HL based on ionization layer scale,[39] $\delta_{HL} = \eta/\left(n_0\sigma\right)$; where n_0

is neutral vapor density and σ is ionization cross section. Since temperature is not known a priory, 6 eV is considered to estimate σ which is assumed to be constant for all simulations. The actual variation in σ with temperature is obtained by choosing a suitable value for η. For the ablation of a target material with given fluence, η is assumed to be constant. Which means, an average value of ionization cross section is used to estimate δ_{HL} for a given ablation regime. However, η is varied for different ablation regimes to account for the variation in σ with average temperature in HL (if fluence and/or target material are changed) and change in physical properties of vapor (if target material is changed).

The coefficient η is varied from 0.5 to 0.08 to study flow dynamics of the region adjacent to KL. The following conditions are considered: 248 nm wavelength, 8 ns $FWHM$ Gaussian profile laser beam with fluence of 10 J/cm^2 and pulse duration of 30 ns. Cell size at the edge of KL is taken smaller than the least possible ionization length in order to capture HL. Variable grid is used for both target and plasma domains. The first cell size in solid domain is 10 nm while for fluid domain it is 1 nm. The target domain is thick enough to satisfy infinite slab condition ($T = T_{initial}$ at the cold end). Fluid domain considered, is long enough to capture shock front throughout the pulse duration. Initially temperature of the target is 300 K and fluid domain is filled with metal vapor at near vacuum condition ($T = 300K$ and $p = 0.004Pa$).

Though it is considered that HL consists of weakly ionized plasma, it becomes very strongly ionized just outside HL. Also, it is not straightforward to specify the degree of ionization at the edge of HL as the transition length is of the order of microns. So, at any point of time, the minimum fraction of neutrals at the outer edge of HL is considered to be 0.1. That means, η is chosen such that, fraction of neutrals, $C_a\left(\delta_{HL}\right) > \approx 0.1$. This value of C_a is arrived at by observing the validity of numerical results with experiments which will be discussed in the next subsection. Figure 3.3(a)

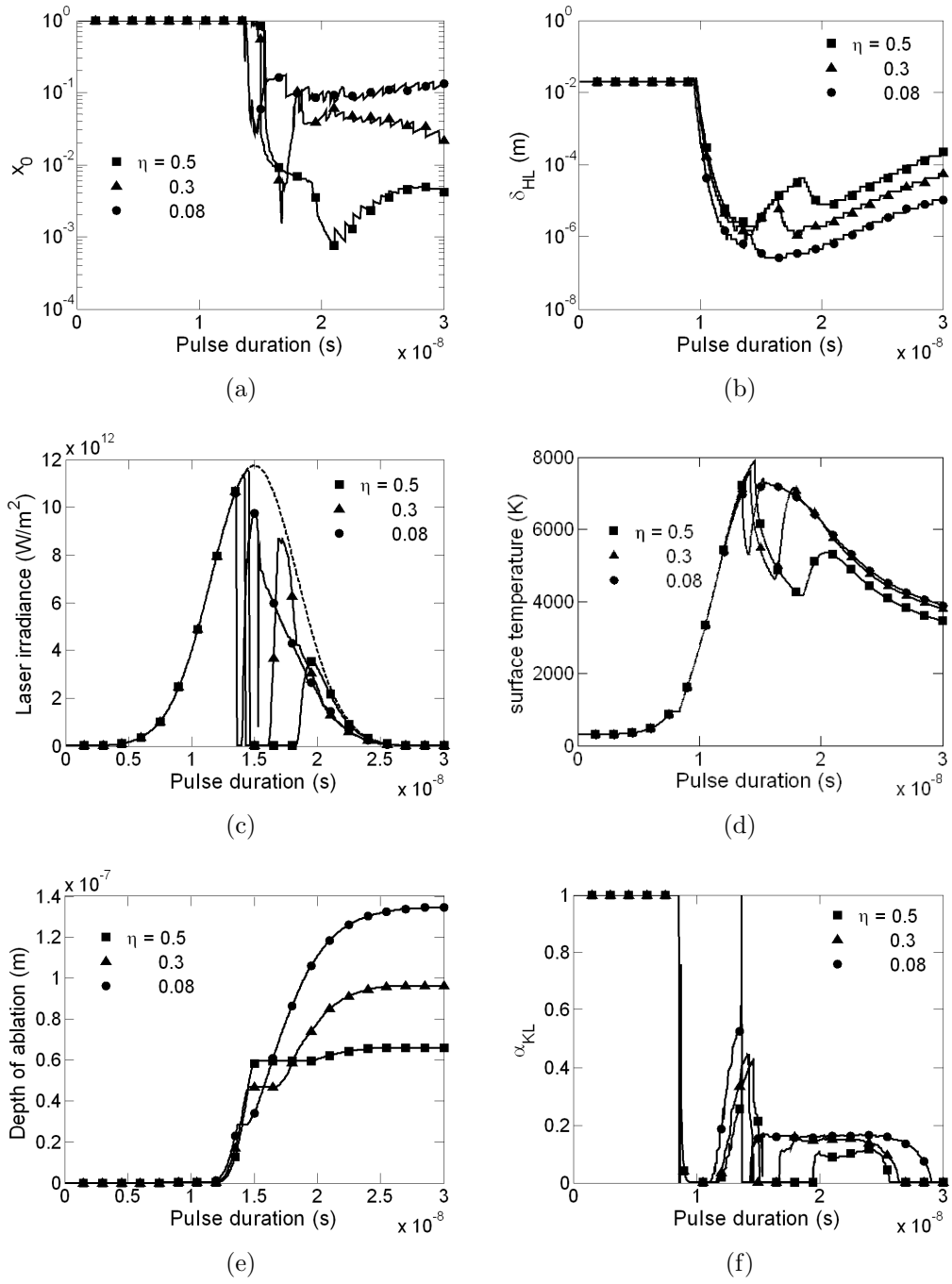

Figure 3.3: Influence of η on ablation process for laser fluence of 10 J/cm^2: (a)neutrals concentration, (b) hydrodynamic layer thickness, δ_{HL}, (c)laser irradiance at the target surface, (d)temperature history of target surface, (e)depth of ablation, and (f) Knudsen layer coefficient, α_{KL}

shows the dependency of C_a on η. Since C_a decreases with z, minimum value of C_a which exists at the outer edge of HL is considered for the plot. Figure shows that C_a increases with the decrease of η. It can also be seen from this figure that $C_a << 0.1$ in the second half of the pulse for $\eta = 0.5$ while $C_a \approx 0.1$ for $\eta = 0.08$. Since δ_{HL} is directly proportional to η, it decreases with η (Fig. 3.3(b)). Laser irradiance at the target surface for three values of η is shown in Fig. 3.3(c). In all these cases irradiance reaching the surface is less than the input due to plasma shielding. An identical trend of dip and rise[9] are observed for all the three cases. For smaller η, i.e. smaller δ_{HL}, the vapor undergoes ionization from a point closer to the outer edge of KL, as high temperature propagates quickly and the resulting plasma absorbs laser the irradiance. So dip is observed at earlier point of time. Then, vapor density drops suddenly due to expansion, which results in the reduction of plasma shielding and leads to the recovery of irradiance. For larger η, ionization starts at a later point of time i.e. at the moment high temperature propagates to the outer edge of HL. Until this point of time whole energy of laser beam reaches the target as there will not be absorption. Once the temperature at the HL edge rises high enough to cause ionization, plasma absorbs laser energy and plasma temperature increase quickly which results in very strong ionization that leads to complete absorption of laser energy. In this case, recovery of irradiance is comparatively very small. Because, by this time the density of neutrals increases in the plume and electron-neutral absorption contributes to the absorption of laser energy by the plasma.

Influence of η on target surface temperature history is shown in Fig. 3.3(d). The flat region in all profiles indicates the melting point of the material. For smaller η, peak temperature is lower as peak laser irradiance at the surface is less than those of higher η. The trends, early dip and rise in the case of lower η and continuous dip of cases corresponding to higher η, are in accordance with laser irradiance profiles. Ablation depth (Fig. 3.3(e)) increases with the decrease of η due to decrease in total

laser energy at the target surface. The flat region seen in the profiles infers that rate of evaporation is zero at this time band. This is because of the dip in heat flux and due to negative values of α_{KL} (Fig. 3.3(f)) which actually indicates back flux of vapor particles. After this time band, heat flux recovers and α_{KL} becomes positive leading to evaporation.

Moreover Fig. 3.3, shows the interdependency of ablation parameters and the influence of η on ablation rate. Variation of η from 0.5 to 0.08 results in over 100 % change in the depth of ablation. Based on weak plasma assumption, and from Fig. 3.3(a), η= 0.08 seems to be a suitable value for calculations. Depth of ablation obtained using this value of η and fluence 10 J/cm^2 (Fig. 3.3(f)) shows good agreement with experiments which will be discussed in section 3.2.2 in detail.

The plume properties for η = 0.08, at 15, 20 and 30 ns are shown in Fig. 3.4. Figure 3.4(a) shows that initially, the flow temperature is high at the surface due to absorption of laser energy by the ionized plume. After some time, the temperature in the plume at the shock front exceeds the ionization temperature and some portion of the energy is absorbed by the resultant plasma. The corresponding velocity profiles are shown in Fig. 3.4(b). Velocity of the plume increases with time due to absorption of laser energy and expansion. Pressure and density distribution in the plume is shown in Figs. 3.4(c) and 3.4(d). Peak pressure and density are observed at mid-pulse and decreases gradually with time. In reality the shock wave will not form adjacent to vacuum, but here in this model perfect vacuum is not simulated. So, there exists high pressure ratio (though pressure is low $\approx$ 1 Pa) at the plume front to form a shock wave. However this shock will not affect the solution as the density in this region is very low and absorption of energy from the laser is negligible. The temperature and velocity distributions (Fig. 3.4(a) and 3.4(b)) are in qualitative agreement with the analytical solution obtained for plume expanding to 1 kPa background gas in the case of laser ablation of graphite.[40]

Distribution of species in the plume at 15 ns is shown in Fig. 3.5(a). It is seen from the figure that the degree of ionization increases towards the shock front where the highest temperature is noticed. Beyond the shock front, flow is neutral as the temperature is very small. It is also seen here that, $C_a < 0.2$ in most of the plume other than at the shock front, where there is a chance of getting higher ionization states ($Z > 3$), but it is of not much importance as the density is very low in this region. The ionization fractions across HL (Fig. 3.5(b)) at 15 ns shows transition from weakly ionized plasma to strongly ionized plasma. Figure 3.6 shows temperature distribution in the target at the three time points. From 15 ns onwards, the temperature at the

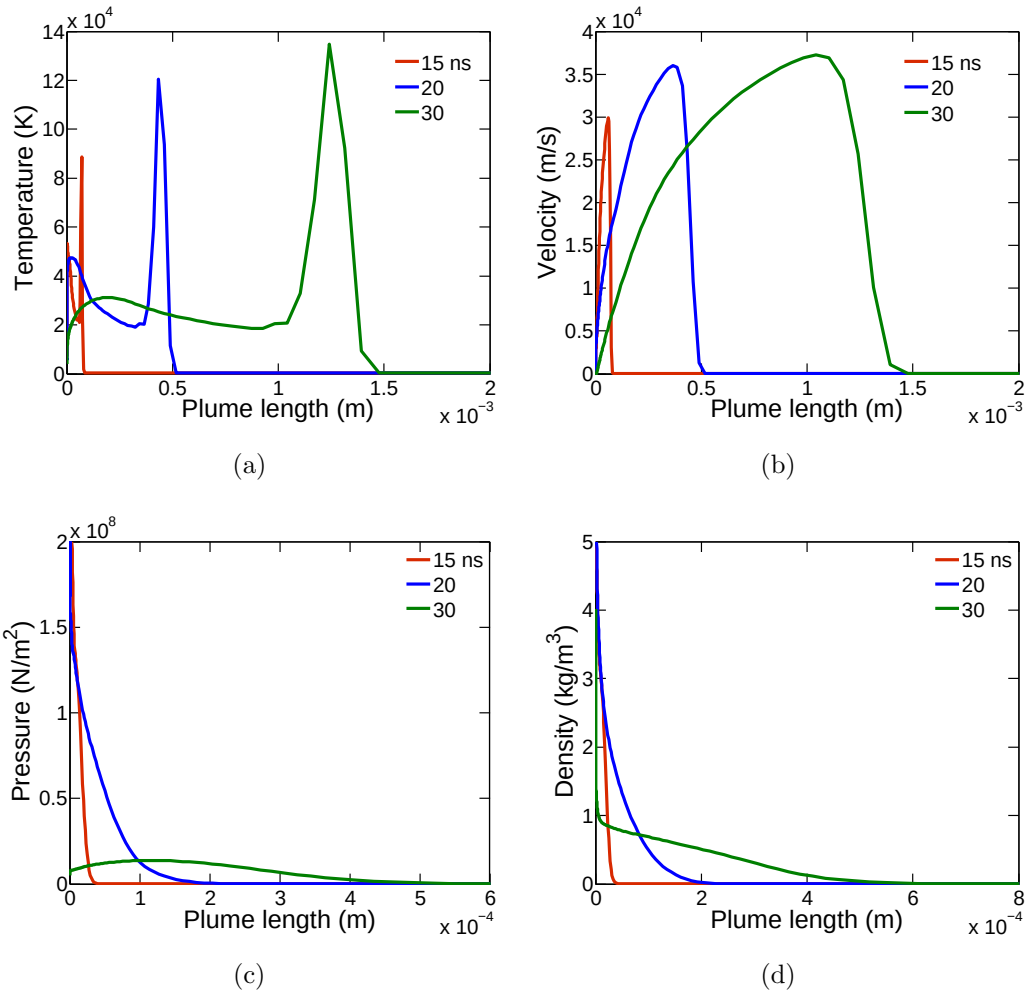

Figure 3.4: Flow distribution in the plasma plume of Al alloy for laser fluence of 10 J/cm^2: (a)temperature, (b)velocity, (c)pressure, and (d)density

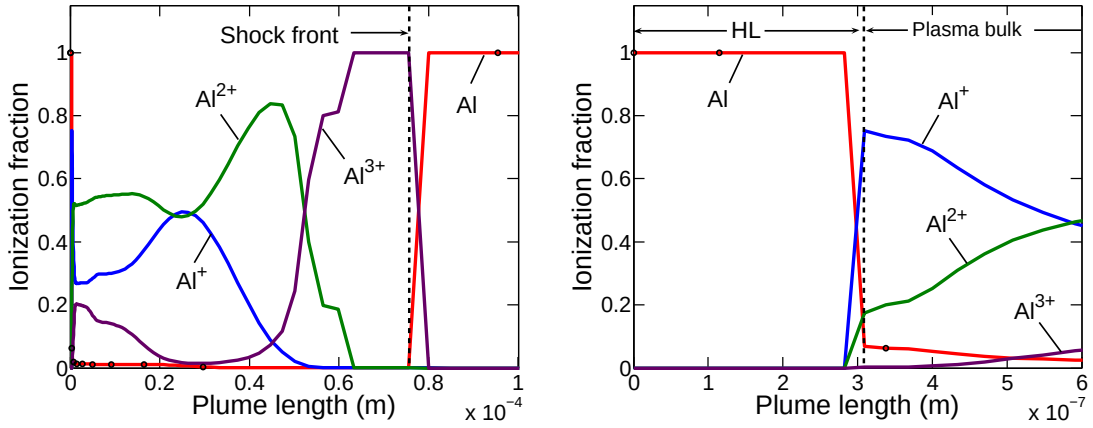

(a) (b)

Figure 3.5: Species concentration in plasma plume of Al alloy for laser fluence of 10 J/cm^2 at t = 15 ns: (a) plasma bulk and (b) hydrodynamic layer.

ablation surface decreases while it increases in the interior regions. This is because of the reduction in laser irradiance at the surface and due to conduction of heat from surface to interior regions. The flat region in the profiles distinguishes molten metal from solid and also it shows depth of melt.

3.2.2 Validation

The self consistent model developed here is first compared with expansion to sonic speed model and then validated with experimental results. Laser fluence of 10 J/cm^2 with pulse duration of 30 ns is considered for comparison with sonic speed model. Laser irradiation at the target surface is shown in Fig. 3.7(a). Early dip in heat flux for sonic speed model infers higher evaporation rate and hence larger absorption of laser energy. Corresponding surface temperature histories are shown in Fig. 3.7(b). Though the self consistent model predicts higher surface temperature, it has a larger dip duration during which rate of ablation is much lower than that of the sonic speed model. This conclusion is also evident from the depth of ablation shown in Fig. 3.7(c). So, cumulative depth of evaporation for self consistent model at the end of pulse is less than that of sonic speed model.

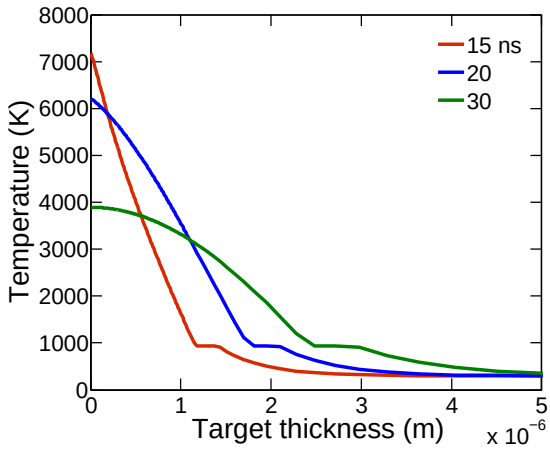

Figure 3.6: Temperature distribution in the target for laser fluence 10 J/cm^2

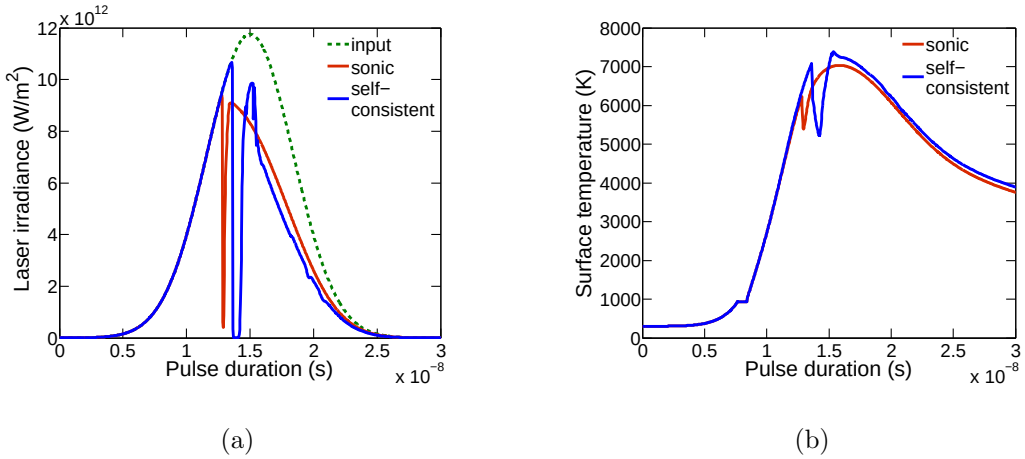

(a) (b)

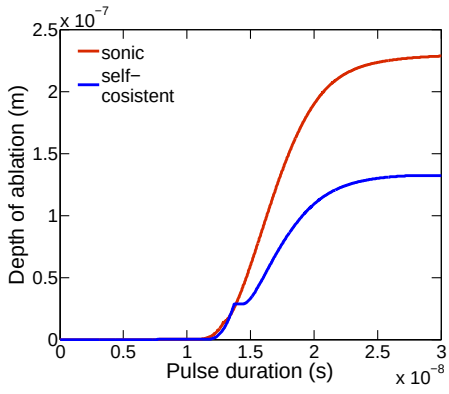

(c)

Figure 3.7: Comparison of sonic and self-consistent models.

The depth of ablation obtained using sonic and self-consistent models with nanosecond pulse at different laser fluences is compared with experiments. Most of the experimental data found in literature correspond to femto and picosecond pulses.[41;42;43] The results available in nanosecond regime are either confined to plasma parameters[44;6;45] or with depth of ablation given for limited range of laser fluences.[46] Though depth of ablation of Al is given for wide range of power densities by Korner et al.,[47] those are not considered here due to difficulties involved in extraction and interpretation. Depth of ablation obtained by Dou et al.[48] for Al alloy in the fluence range 0.02 to 10 J/cm^2 is considered for validation purpose. The laser system used for the experiment, carried out by Dou et al., has Lambda Physik model $LPD500 - fs$ dye laser and a Lambda Physik $EMG150$ of a dual-cavity excimer laser. The system has a provision to produce two types of lasers: 308 nm beam with pulse width of 15 ns and 248 nm with pulse width of 500 fs. The target is irradiated with 10 pulses with a repetition rate of 10 Hz and average depth per pulse is given in the fluence range 0.02 to 10 J/cm^2.

Figure 3.8(a) reflects the difference in depth of ablation of Al alloy obtained by the sonic speed model, self consistent model, and experiments. Sonic and self consistent model results are almost the same up to 6 J/cm^2 after which the sonic model diverges from the self consistent model. The sonic model results match well with experiments[41] at 5 J/cm^2, but it diverges after that and self consistent model shows good agreement with experiments. For fluences below 5 J/cm^2, self consistent model will not give good results as it predicts higher vales of δ_{HL} leading to very weakly ionized plasma in large portion of plume. This behavior is due to low n_0 in this fluence range and constant σ. However, by implementing direct variation of σ as function of temperature, the current model may be used for ablation with lower laser fluences. Besides, sonic model shows satisfactory agreement with experiments at lower laser fluences, so it can be used in low fluence regime.

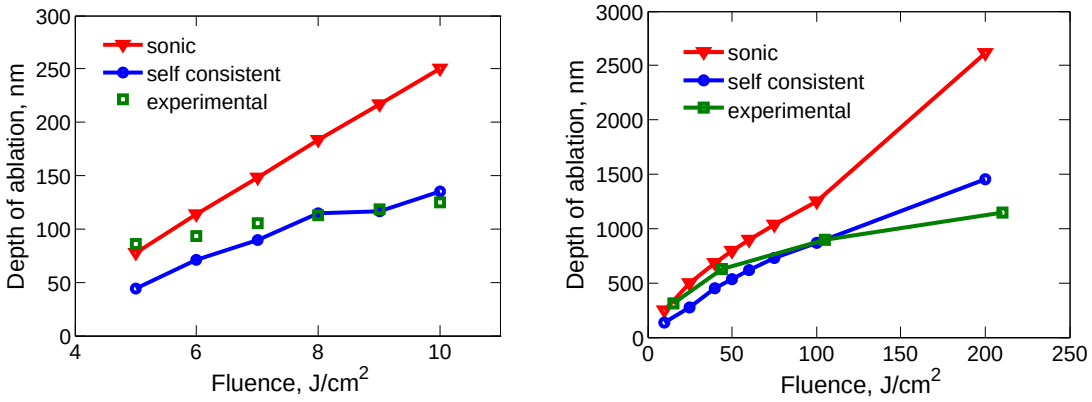

(a) (b)

Figure 3.8: Comparison of sonic and self consistent models and validation with experiments: (a) Aluminum alloy (308 nm 15 ns, experimental data are taken from Dou et al.[48]) and (b) Copper (532 nm 6 ns, experimental data are taken from Semerok et al.[49]).

The model is also validated with experiments carried out by Semerok et al.[49] for ablation of pure copper. The experiment is performed at atmospheric pressure using $Nd-YAG$ laser with 6 ns pulse width and 532 nm wavelength. Ablation rate obtained with sonic and self consistent models is compared with experimental results in the fluence range of 10 to 200 J/cm^2. Figure 3.8(b) shows that sonic model results are closer to experiment for laser fluences below 50 J/cm^2 and beyond this self consistent model results are more realistic. Also it shows that sonic model over predicts the ablation rate at higher fluences, which is consistent with the ablation of Al alloy in Fig. 3.8(a). Since ablation of both metals show similar characteristics and the numerical results are close to experiments, our assumption of C_a at the outer edge of HL may be justified. In fact, value of C_a is obtained after several numerical experiments to get close agreement with experimental results of Al alloy at one laser fluence and then, the same value (0.1) is considered for all other fluence ranges for both Al alloy as well as Cu. However, η has to be obtained for each ablation regime based on the assumption made in section 3.2.1.

3.3 Sample calculations

Laser ablation of Al alloy is obtained using self consistent model with laser fluence varying from 5 to 100 J/cm^2. Fig. 3.9(a) shows variation of η and time averaged δ_{HL} with fluence. It can be seen that δ_{HL} decreases with the increase of laser fluence. Since, δ_{HL} is inversely proportional to n_0, which increases with T_0, this trend is observed. Figure 3.9(a) also shows that, η increases with the increase of laser fluence up to 10 J/cm^2 and then decreases with further increase of fluence. In reality, the ionization cross section, σ initially increases sharply and then decreases gradually with the increase of temperature.[50;51] Here in this study, η is introduced to account for the average variation in ionization cross section in HL and hence similar trend is displayed by η. Similarly, for Cu ablation shown in Fig. 3.8(b), η increases from 0.025 at 10 J/cm^2 to 0.041 at 100 J/cm^2 and then decreases continuously to 0.02 at 200 J/cm^2. However, the values of η for Al and Cu differ as the ionization layer scales are different for both materials.

Time averaged Mach number and temperature at the outer edge of KL are shown in Fig. 3.9(b). It shows that M_1 increases sharply from 0.11 at 10 J/cm^2 to 0.14 at 25 J/cm^2 and then gradually from there afterwards. Below 10 J/cm^2, a constant increasing trend is seen with the decrease of fluence, which may reach Mach 1 (sonic speed) on further decrease of fluence. The average Mach number obtained is much below sonic speed which is also observed previously in different conditions.[28;52] As expected, T_1 in Fig. 3.9(b), increases continuously with the increase of laser fluence i.e. increase of energy input to the vapor.

Time averaged M_2 and T_2 are shown in Fig. 3.9(c). The properties increase from KL edge to HL due to decrease in pressure and addition of laser energy to vapor. It is interesting to note here that, M_2 variation is exactly opposite way of M_1. This behavior is because of decrease in pressure difference across HL due to absorption of high laser energies at higher fluences near HL outer edge. Finally, the depth of

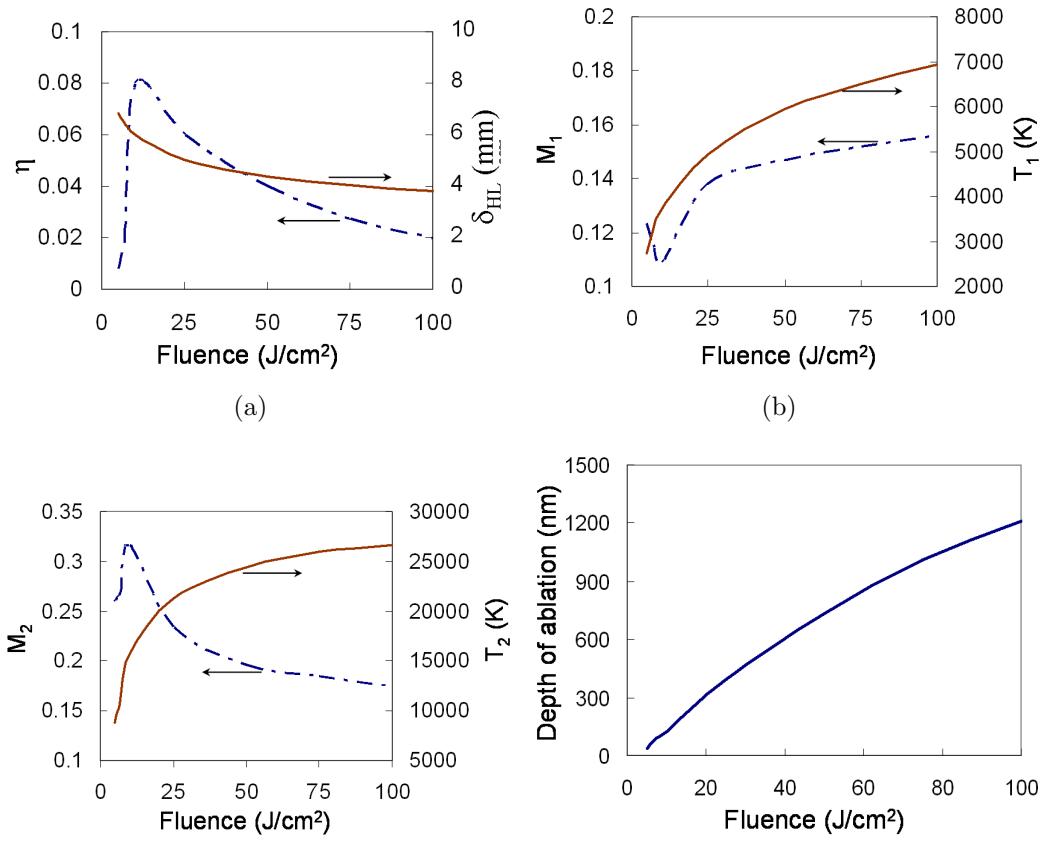

Figure 3.9: Sample calculations for Aluminum alloy for laser fluence varying from 5 to 100 J/cm^2: (a)η and time averaged δ_{HL}, (b) time averaged flow parameters at KL outer edge, (c)time averaged flow parameters at HL outer edge, and (d) depth of ablation.

evaporation is shown in Fig. 3.9(d). Since, rate of evaporation is directly proportional to V_1, slope of the curve decreases with the increase of laser fluence.

3.4 Effect of beam frequency

The absorption coefficient, α and absorptivity, A in Eqs. (3.3) and (3.4) are calculated as shown in Eqs. (3.15) and (3.16).

$$\alpha = \frac{4\pi k}{\lambda} \tag{3.15}$$

$$A = (1 - R) = \frac{(n-1)^2 + k^2}{(n+1)^2 + k^2} \tag{3.16}$$

where, R is reflectivity, n and k are real and imaginary parts of the effective index of the refraction of a material.

Ablation analysis is carried out with λ varying from 193–1064 nm and laser fluence 10–100 J/cm^2. Three materials Al, Cu and Ti are considered for the analysis. The real and imaginary parts of index of refraction of the three materials for the considered range of wavelength are taken from Ref.[8] It is observed that the optical properties of solid and molten Al are almost similar,[53] so same values shown in Ref.[8] are considered for the respective molten states. Gaussian profile laser pulse of 30 ns duration with $FWHM$ at 8 ns is considered. Figure 3.10 shows the ablation characteristics and surface properties of Al, Cu, and Ti. Sub plots in the top row show depth of ablation contours, percentage of energy absorbed by plasma, and surface properties as function of wavelength respectively for Al metal. Sub plots in middle and bottom rows show similar contours and surface properties for Cu and Ti metals.

As expected, depth of ablation of Al increases with the increase of laser fluence. But it increases gradually with wavelength until 850 nm and then decreases sharply. Maximum depth of ablation is found at 850 nm for all fluences, and it seems to be contradicting the plot shown for plasma shielding for Al, because depth of ablation is maximum at the beam parameters for which percentage of energy absorbed by plasma is highest. But it is true, as energy absorbed by plasma due to inverse Bremsstrahlung process (Eqs. (3.11) and (3.12)) is directly proportional to the number densities of plasma and it increases with the rate of evaporation. Therefore both maxima appear at more or less same fluence and wavelength Surface properties plot of Al show that, R remains more or less same up to $\lambda = 450$ nm, decreases sharply till $\lambda = 850$ nm, and then increases sharply. Since R is lowest at $\lambda = 850$ nm, heat flux at the Al surface is highest at this wavelength and hence depth of evaporation is maximum.

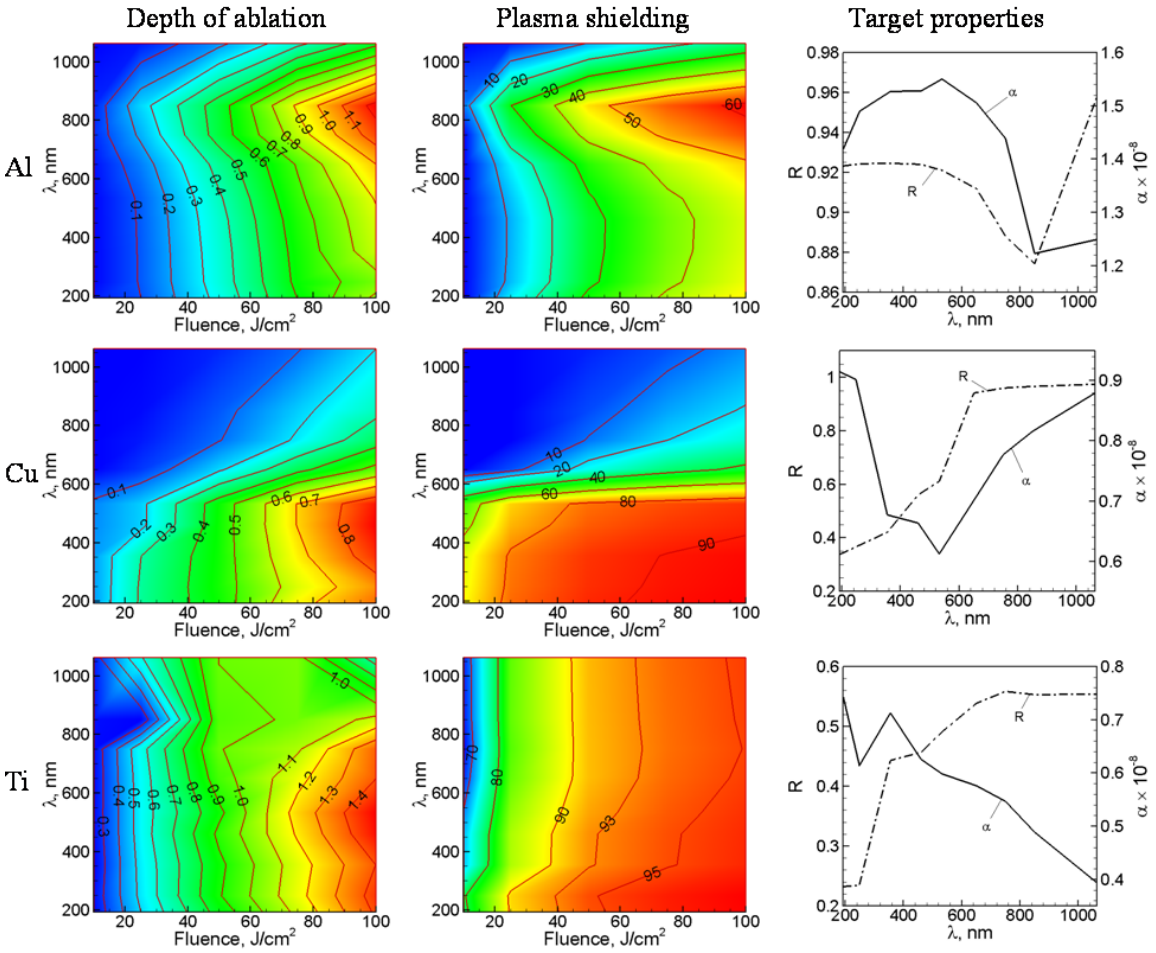

Figure 3.10: Effect of laser beam wavelength and energy fluence on ablation of pure metals. Ablation characteristics of three metals Al, Cu and Ti are given in top, middle and bottom rows respectively. The depth of ablation contours in μm are given in the first column, percentage of energy absorbed by plasma is given in second column, and surface properties are given in the third column. Surface properties are taken from Ref.[8]

Though R is constant in the range 190 to 532 nm, there is a gradual change in depth of evaporation due to change in plasma shielding and λ. It is difficult to find the exact influence of inverse Bremsstrahlung absorption as it is a function of temperature and plasma density, which depends on the instantaneous rates of evaporation. Rate of evaporation in turn depends on the plasma parameters at the edge of HL. So the effect of α_{e-n} and α_{i-n} is found indirectly by keeping $\alpha = 1.41\times10^8$ and $R = 0.921$ (values corresponding to $\lambda = 193$ nm) constant, while varying λ. For a fluence of

50 J/cm^2 the depth of ablation and percentage of energy absorbed are found to be 370 nm and 31.13 % for $\lambda = 193$ nm, and 402 nm and 29.94 % for $\lambda = 532$ nm. This shows that depth of ablation increases with the increase of λ. The actual depth of ablation for $\lambda = 532$ nm is 386 nm which shows the effect of α, i.e. depth of ablation decreases when α is increased from 1.41×10^8 to 1.55×10^8. It is interesting to note here that, depth of ablation decreases with the increase of α, this is because the amount of energy absorbed with smaller α becomes greater than that absorbed with larger α after a certain depth. For instance, the amount of energy absorbed by Al with $\alpha = 1.41$ exceed the energy absorbed with $\alpha = 1.55$ at a depth of 0.5 nm. However, the influence of α_{e-n}, α_{i-n}, and α on ablation depth is found to be very small when compared to the influence of R.

The trend of ablation contours of Cu shown in middle row differ from those of Al. The depth of ablation is maximum at $\lambda \approx 360$ nm for fluences < 50 J/cm^2, while it is maximum at $\lambda \approx 460$ nm for fluence > 50 J/cm^2. This trend can be explained using plasma shielding contours of Cu. For fluences < 50 J/cm^2 and $\lambda <$ 360 nm, plasma shielding is more or less constant so, the ablation contours in this region display similar trend. For fluences > 50 J/cm^2, the plasma shielding is highest for lowest wavelength. At low λ, since the reflectivity is very low, ablation rates are high during the first half of laser pulse. The high density plasma formed will increase plasma shielding and hence ablation rate decreases. For instance, the ablation rate of Cu for $\lambda = 193$ nm and fluence of 100 J/cm^2 is greater than that for $\lambda = 460$ nm during the first 12 ns and it becomes less, there afterwards. This shift in time location increases with the decrease of fluence and if it occurs in the second half of the pulse there will not be any noticeable change in the ablation characteristics. Coming to higher wavelength ($\lambda > 532$ nm), the depth of ablation decreases continuously as the reflectivity increases drastically.

Ablation contours of Ti target are shown in bottom row of Fig. 3.10. For fluences

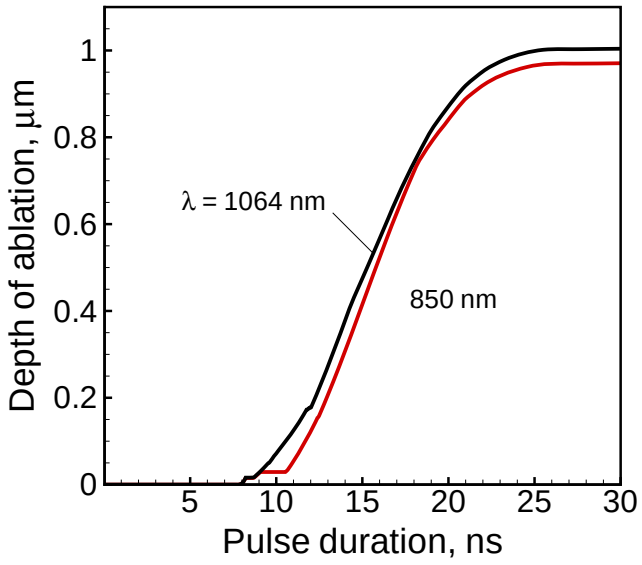

Figure 3.11: Cumulative depth of evaporation of Ti target with a laser fluence of 50 J/cm^2

below 60 J/cm^2, depth of ablation is slightly higher at $\lambda \approx 750\ nm$, whereas for higher fluences above 60 J/cm^2 maximum depth of ablation is observed for $\lambda \approx 532\ nm$. For all fluences, the depth of ablation decreases suddenly at $\lambda \approx 850\ nm$, and then it increases with the increase of λ. At 850 nm, the sudden decrease in depth of ablation is due to back flux. If the pressure at the evaporating surface is less than that of the surrounding plasma plume then evaporation will not occur. Figure 3.11 shows the comparison of cumulative depth of evaporation for $\lambda = 850\ nm$ and 1064 nm with fluence of 50 J/cm^2. It shows that, back flux starts for both wavelengths at same time around 8 ns, but it extends to greater duration for 850 nm compared to that of 1064 nm. This is because of the difference in the energy absorbed by the surface. Reflectivity, R is same for both wavelengths, but α is small for 1064 nm, which causes greater internal heat absorption that, leads to higher surface temperature and evaporation pressure. Previously, it was observed in the case of Al ablation that, the influence of α is less significant, but here in this case of Ti, it is influential

to considerable extent. This is because, heat absorbed by the surface is directly proportional to R (Eqs. (3.3) and (3.16)) and Ti has low reflectivity (0.75) compared to that of Al (0.92). It is interesting to observe from sub plot for plasma shielding of Ti, that more than 90% of the laser energy is absorbed by plasma for fluences greater than 40 J/cm^2 for all wavelengths.

The optimum wavelengths specified above are all based on single pulse ablation. If there are multiple pulses, the plasma density in the plume increases and the rate of increase depends on the time lag between successive pulses. If the time lag is large, then the plasma created by previous pulse will expand out giving way to the plasma generated by new pulse. On the other hand, if time lag is shorter than the expansion time, the plasma created by new pulse will add to that created by the previous pulse and the overall density increases. Figure 4 shows that, wavelength converges to a single optimum value at higher plasma densities. So, the optimum wavelength calculated for single pulse may be extended to multiple pulses with loss of some accuracy.

3.5 Mitigation of communication attenuation

The properties of plasma generated by laser ablation vary with time, and hence it is essential to consider transient sheath equations to obtain instantaneous sheath thickness in the plasma. Transient sheath thickness is calculated using Eq. (3.17). It is obtained by equating the Child law[54] ion current density with that at the plasmasheath interface due to drift velocity V and the uncovering of ions.[55] The electron density in Eq. (3.17) varies with time and space. By assuming electron density to be dependent only on time and its value equal to the peak density in the plume at any instance of time, Eq. (3.17) may be transformed into an ordinary differential equation. This can be solved analytically to obtain a simple expression for a transient sheath that is given by Eq. (3.18). The variable s_0 is given by Eq. (3.19), and

V_B is velocity due to the Bohm criterion given by Eq. (3.20). Equation (3.18) is solved numerically using Newton-Raphson method in conjunction with the ablation model. At a particular time instant, peak density of electrons and its location are found in the plume domain. Using these parameters as inputs, for a given value of U, sheath thickness is obtained at all time instances. Sheath characteristics for Al and Ti plasma in N_2 background maintained at 1 atm pressure are discussed first and then the effect of background pressure on sheath requirements in Al plasma are discussed.

$$\frac{ds}{dt} = \frac{4}{9}\varepsilon_0 \left(\frac{2Z_i e}{m_i}\right)^{1/2} \frac{U^{3/2}}{s^2} \times \frac{1}{Z_i e n\,(z)} \tag{3.17}$$

$$s = s_0 \frac{exp\left[2\left(s + Vt\right)/S_0\right] - 1}{exp[2\left(s + Vt\right)]/s_0 + 1} \tag{3.18}$$

$$s_0 = \left(\frac{4}{9}\varepsilon_0\right)^{1/2} \left(\frac{2Z_i e}{m_i}\right)^{1/4} \frac{U^{3/4}}{\left(eZ_i n V_B\right)^{1/2}} \tag{3.19}$$

$$V_B = \left(\frac{k_B T}{m_i}\right)^{1/2} \tag{3.20}$$

The transient sheath characteristics of Al plasma generated with a laser fluence of 4 J/cm^2 using bias voltage of 9 kV are shown in Fig. 3.13. The sub plots show instantaneous peak density of electrons, location of peak density, ratio s/s_0 and s. Figure 3.13(a) shows the simulation carried out during laser pulse of 30 ns. Plasma starts to develop from 10 ns onwards. The density of electrons increases as pulse progresses and it decreases towards the end of the pulse as energy of pulse decreases. The location of peak electron density varies from 10^{-8} m to $5{\times}10^{-4}$ m. The ratio s/s_0 varies from 10^{-3} to 1 and a sudden jump can be seen at the location when electron density builds up. It shows that within this time scale and at lower values of n_e,

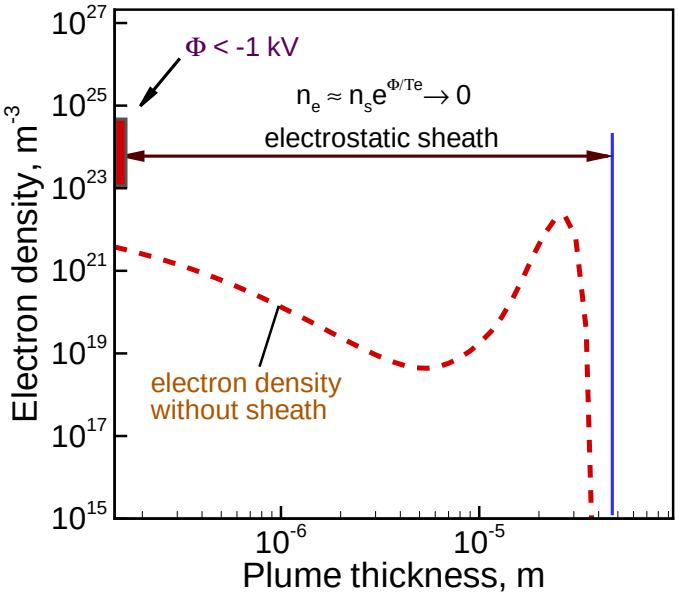

Figure 3.12: Electrostatic sheath conceptual schematic

transient sheath calculations are required while at higher n_e, Child-Langmuir sheath calculations are sufficient. During first 10 ns, s is very large as n_e is small, and as time progresses, n_e increases and s decreases. Figure 3.13(a) shows clearly that, s is greater than the location of peak density within the pulse duration of 30 ns. After the laser pulse is stopped, the plasma formed at the surface continues to expand to the background pressure, while peak density of electrons decreases continuously due to recombination of electrons and ions. The sheath thickness increases as the peak density of electrons decreases and Fig. 3.13(b) shows that it is always larger than the location of peak density of electrons. In summary, Fig. 6 shows that, electromagnetic waves can be transmitted through Al plasma generated with 4 J/cm^2 fluence and 1 atm background pressure.

The sheath characteristics with laser fluence of 4.5 J/cm^2 and $U = 10$ kV is shown in Fig. 3.14. At this laser fluence, n_e is very high (λ 1026 m^{-3}) and hence the sheath thickness is small and it is smaller than the peak density location. Though, the sheath thickness can be increased by increasing U, due to the limitations involved in onboard

voltage sources, maximum allowable value for U is 10 kV.

Similar analysis is carried out for ablation of Ti to find the fluence limit up to which electrostatic sheath can be applied. The sheath characteristics are shown in

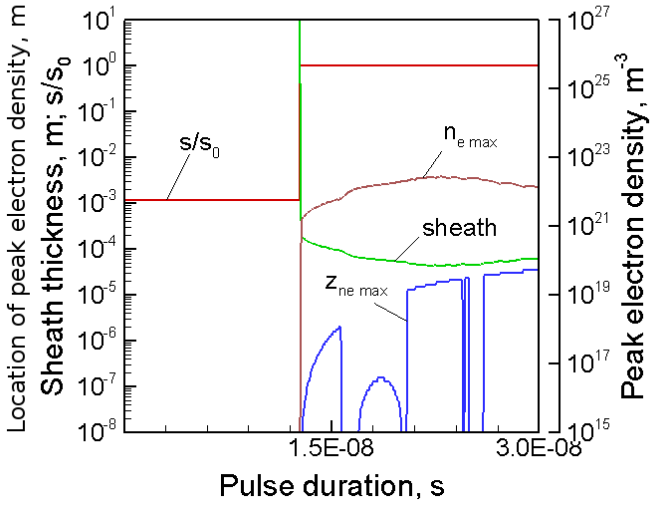

(a)

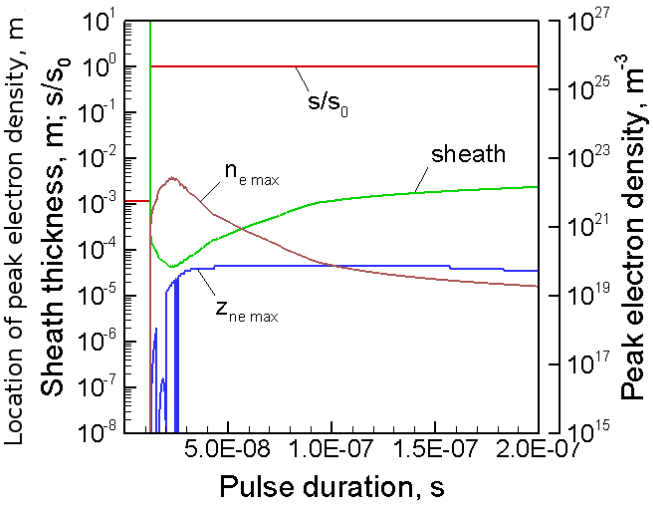

(b)

Figure 3.13: Transient electrostatic sheath using 9 kV bias voltage in thermally ionized plasma generated by ablation of Al with laser fluence of 4 J/cm^2 in N_2 background maintained at 1 atm: (a) during pulse and (b) beyond pulse.

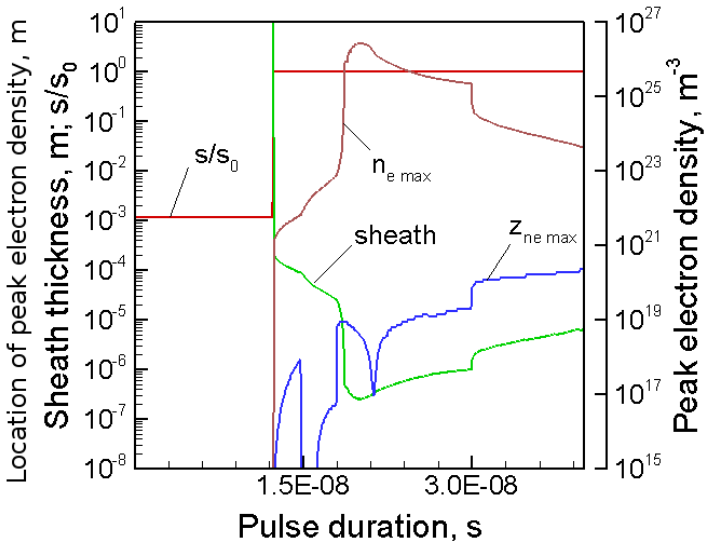

Figure 3.14: Transient electrostatic sheath using 10 kV bias voltage in thermally ionized plasma generated by ablation of Al with laser fluence of 4.5 J/cm^2 in N_2 background maintained at 1 atm

Fig. 3.15. It can be seen from Fig. 3.15(a) that sheath thickness is greater than maximum n_e location for a fluence of 1.3 J/cm^2 and $U = 1$ kV. Figures Fig. 3.15(b) and Fig. 3.15(c) show that sheath thickness for a slightly higher fluence of 2 J/cm^2 and with $U = 1$ and 10 kV, is smaller than peak n_e location. Hence electrostatic approach can be used for Ti plasma during laser ablation with fluences up to 1.3 J/cm^2 only.

The peak electron density history of Al plasma generated using laser fluence of 4 J/cm^2 in N_2 background with pressure varying from 10^5 Pa to 10^2 Pa is shown in Fig. (3.16). The electron density increases with the decrease of pressure up to 10^4 Pa then decreases with the further decrease of pressure up to 10^2 Pa. When the background pressure is decreased, the shock strength increases which results in higher temperatures while the vapor density decreases due to increased plume length. Though, there exists high density of N_2 at the shock front, the ionization rates are

negligibly small due to its high ionization potential. So, there exists a certain value of background pressure for which electron density is maximum. For the present regime, this pressure is found to be around 10^4 Pa.

The sheath thickness and location of the peak density of electrons are shown in Fig. 3.17 for four different background pressures with a bias voltage of 9 kV. For the case of 7.5×10^4 Pa background pressure Fig. 3.17(a), the sheath thickness is greater than the location of peak density of electrons at all time instances. The

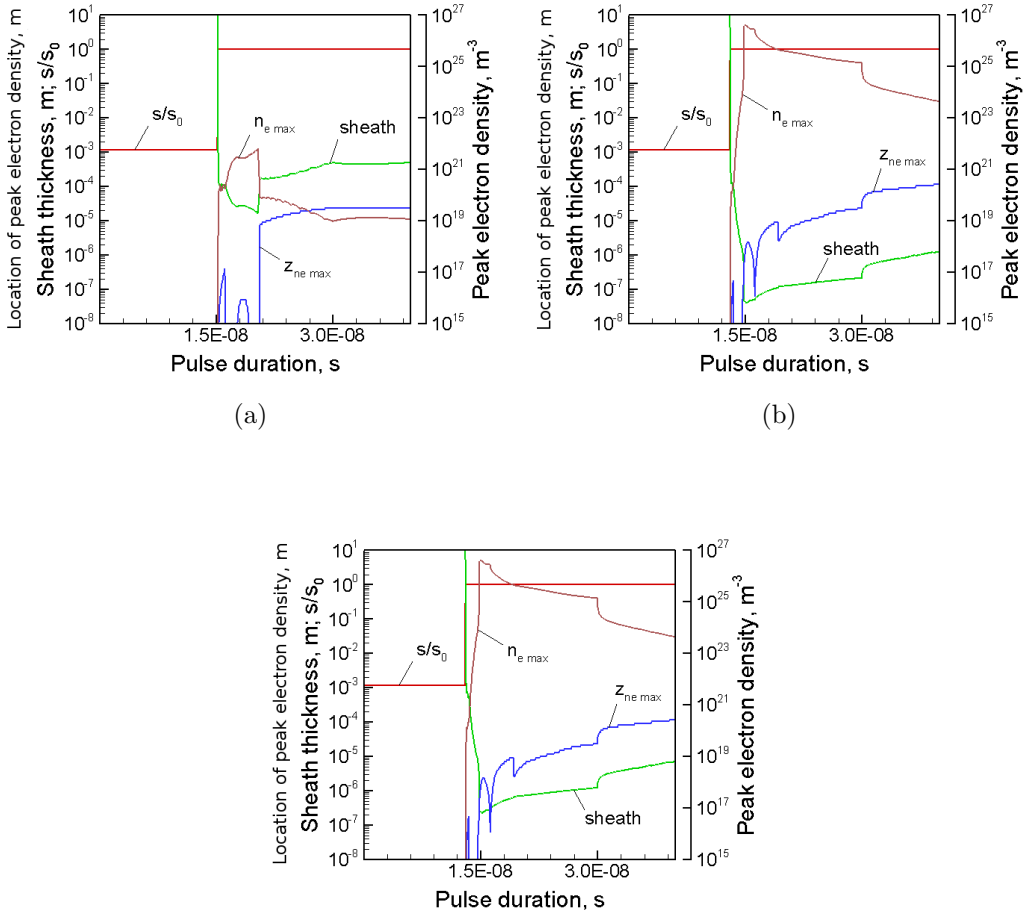

(a) (b)

(c)

Figure 3.15: Transient electrostatic sheath in thermally ionized plasma generated through laser ablation of Ti in N2 background maintained at 1 $atm.$: (a)laser fluence 1.3 J/cm^2 and bias voltage 1 kV (b) laser fluence 2 J/cm^2 and bias voltage 1 kV, and (c) laser fluence 2 J/cm^2 and bias voltage 10 kV.

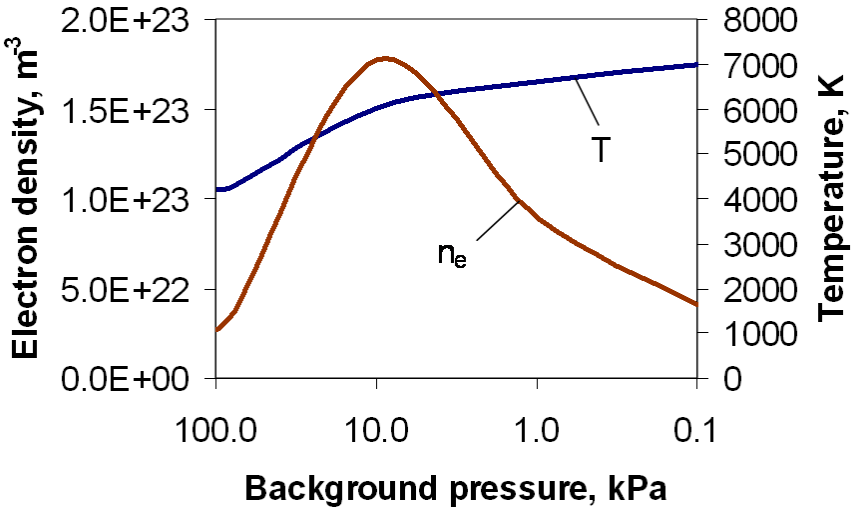

Figure 3.16: Effect of background pressure on plasma electron density and temperature

sheath thickness is smaller than peak electron density location for the remaining three background pressures 10^4, 10^3, and 10^2 Pa shown in Figs. 3.17(b)-3.17(d) respectively. Since electron density is highest for background pressure of 10^4 Pa, sheath thickness is smallest. Though electron densities and sheath thickness for the cases of $7.5\times$ 10^4 Pa and 10^2 Pa background pressure are of the same order, the location of peak electron density is farther for the latter case due to longer plume. So, the sheath thickness is smaller than the location of peak electron density in the case of 10^2 Pa background pressure. From this analysis it can be derived that, bias voltage requirement increases with the increase of altitude, as pressure decreases.

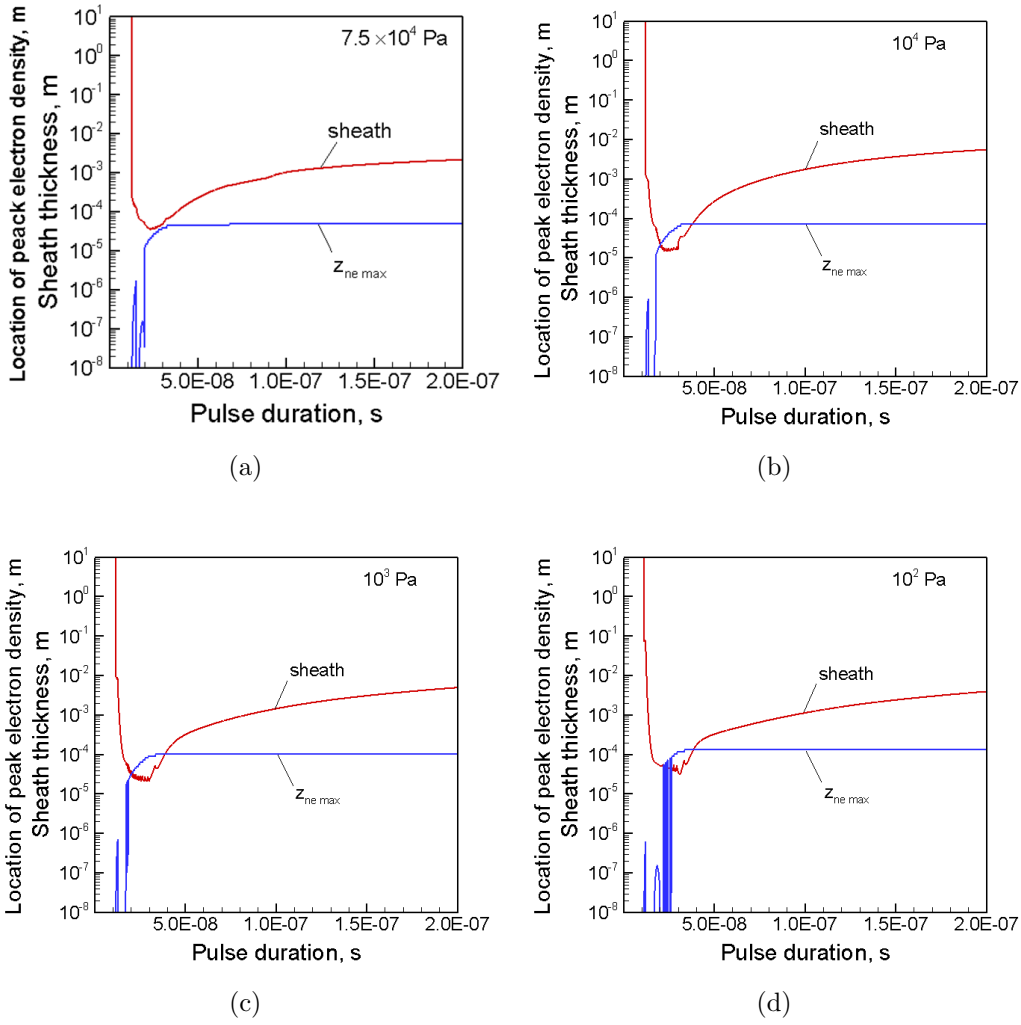

Figure 3.17: Effect of background pressure on location of peak density of electrons and electrostatic sheath during laser ablation of Al alloy with fluence of 4 J/cm^2. Bias voltage is 9 kV and background gas is N_2. Calculations are performed with four different background pressures: (a)$7.5\times10^4 Pa$, (b)$10^4 Pa$, (c)$10^3 Pa$, and (d)$10^2 Pa$.

Chapter IV

Arc discharge ablation

The energy source for arc discharge ablation is the electric current between the electrodes. In macroscopic view point, due to the resistivity of the conducting medium (plasma in this case), heat is generated due to Ohmic or Joule heating within the arc region. The Joule heating increases the plasma temperature and density, which in turn decrease the resistivity. In addition to this, the evaporated particles from the anode, change the chemical composition of the fluid which also influence the plasma temperature and density, due to the change in the overall material properties of the medium especially, the ionization potential.

A brief review of previous work on carbon arc discharge simulations is presented here followed by the mathematical model used in this work. One dimensional model developed by Farhat et al.[56] solved for temperature, species concentration, and velocity in one spatial direction between the electrodes . A more accurate two dimensional model developed by Bilodeau et al.[57] assumes uniform erosion rate of anode obtained from experiments. Navier Stokes equations along with electromagnetic sources and energy equation were solved in cylindrical coordinates using the SIMPLE algorithm. Linear electric field with radial variation of current was considered to simulate the arc between electrodes of equal diameter. It should be pointed out that the linear electric field assumption might be inadequate, if the electrodes are of different sizes, and

hence, current continuity in potential form must be solved.[58] However, in both the cases, azimuthal component of magnetic field intensity alone is significant to consider. Similar formulation with two dimensional electric field was considered by Murphy et al.[59], but it was for the simulation of arc welding process with plate anode.

The general model presented in chapter 2 is simplified by considering the above mentioned factors. In this work, two-dimensional electric field was considered to simulate the arc. Current continuity in electric potential form is solved to obtain the potential distribution. Current is then calculated from the potential, and from axial current, magnetic field is obtained using Amperes law. Conservative form of Navier-Stokes equations with electromagnetic source and energy equation are solved using SIMPLER algorithm.[60] For a given current, the self-consistently obtained data such as flux distribution of individual species, temperature distribution, and electric potential serve as inputs for the nanoparticle growth model.

4.1 Mathematical model

The computational domain and boundary conditions are shown in Fig. 4.1

4.1.1 Arc

Current continuity in electric potential form (Eq. (4.1)) is solved to obtain the potential field and then current $\mathbf{j}$ is obtained. Where, σ is electrical conductivity and φ is electric potential. Electrical conductivity of weakly ionized plasma in DC field is obtained using Chapmann-Enskog equation shown in Eq. (4.2) ,[61;62;63;64] . Where, e, n_e, and m_e are charge, number density, and mass of electron respectively. $\nu_{e,a}$ and $\nu_{e,i}$ are collision frequency of electron-neutrals and electron-ions respectively as given by Eqs. (4.3) and (4.4). k_B, T, n_a, and n_i are Boltzmann constant, temperature, neutrals density, and ion density respectively. Q_m is momentum transfer cross section for electrons and neutrals collision varying with temperature.[65;66] Coulomb logarithm,

$ln(\Lambda)$ in Eq. (4.4) is given in Eq. (4.5) for $T_i = T_e$ and $n_i = n_e$. More details about the numerical implementation are given in Appendix A.3

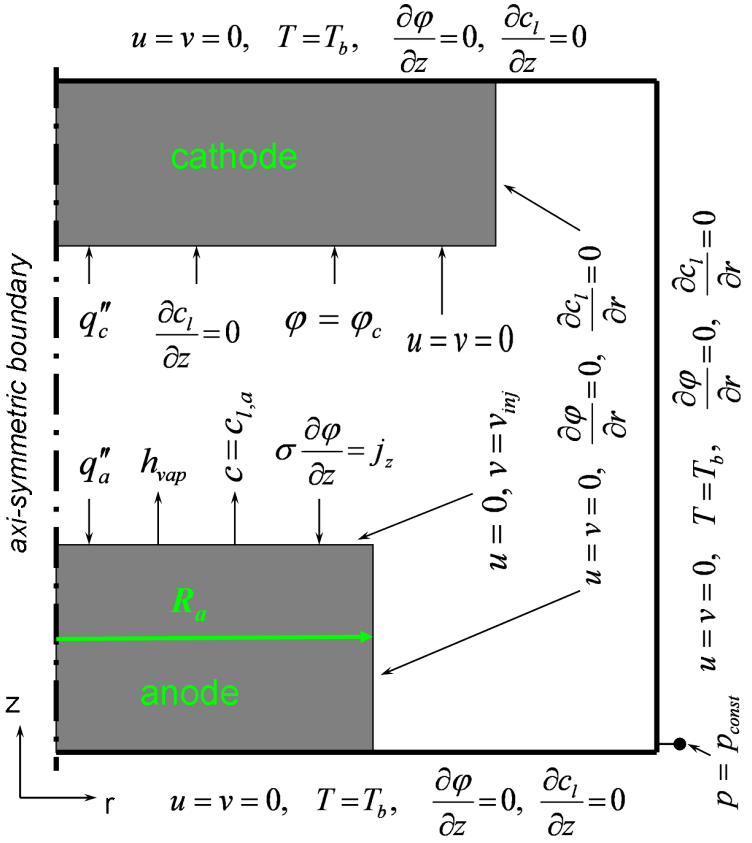

Figure 4.1: Computational domain of arc discharge chamber showing boundary conditions. The average velocity of species mixture is considered at the anode tip and no-slip condition is considered on all other walls for momentum equations. Conduction heat flux from the neutral species to the electrodes is intrinsic to the energy equation and the additional heat flux arising due to arc current is given as external boundary condition on the tip of the electrodes. For species transport, mass fraction of the individual species existing at the anode tip and zero normal gradient on the remaining on interfaces are considered. Constant electric potential at the cathode tip and uniform current flux on the anode tip are considered for electric potential.

$$\nabla \cdot (-\sigma \nabla \varphi) = 0 \tag{4.1}$$

$$\sigma = \frac{e^2}{m_e} \frac{n_e}{(\nu_{e,a} + \nu_{e,i})} \tag{4.2}$$

$$\nu_{e,a} = \frac{4}{3}\left(\frac{8k_BT}{\pi m_e}\right)^{1/2} n_a Q_m \tag{4.3}$$

$$\nu_{e,i} = \frac{4\sqrt{2\pi}}{3} n_i \left(\frac{e^2}{k_BT}\right)^2 \left(\frac{k_BT}{m_e}\right)^{1/2} ln\left(\Lambda\right) \tag{4.4}$$

$$ln\left(\Lambda\right) = ln\left(\frac{4k_BT}{\gamma^2 e^2 k_e}\right) - 2ln\left(\sqrt{2}\right) \tag{4.5}$$

where, $k_e^2 = (4\pi n_e e^2)/(k_BT)$ and $ln(\gamma) = 0.577$ (Euler's constant)[65]

Referring to Fig. 4.1, for Eq. (4.1), $\varphi = \varphi_c$ is constant arbitrary value on the cathode tip and uniform current flux is given at the anode tip. All the remaining surfaces are insulated. The azimuthal component of self induced magnetic field is obtained using Amperes law (Eq. (4.6)). B_θ is azimuthal component of magnetic field, μ_0 is permeability of free space, r is spatial coordinate in radial direction, j_z is axial component of current flux, and R is radius of chamber.[67;68]

$$B_\theta = \frac{\mu_0}{r}\int_0^R j_z r dr \tag{4.6}$$

4.1.2 Sublimation

Initially, arc concentrates near the axial region and the catalyst-filled core intensively evaporates. Due to this intensive evaporation, the gap between electrodes increases near the catalyst core, and hence, the arc shifts towards the enclosed carbon shell. This transition in arc position is expected to alternate between the catalyst core and enclosed carbon shell throughout the experiment. Simulation of this transition is complicated so, it is assumed that anode is made of single uniform compound material and arc is distributed uniformly throughout the anode tip.

Sublimation is calculated using Langmuir model (Eq. (2.2)). Saturation pressure of the three materials is taken from Ref.[36] and then multiplied with the mole fractions

to obtain the overall saturation pressure, p_{sat}[69;70] . Equation (2.2) is applied at all radial locations along the anode tip and plasma interface to account for the variation in surface temperature and the subsequent sublimation rate. It has to be noted here that, Langmuir model predicts higher ablation rate compared to self-consistent model (Eqs.(2.5)–(2.7) and (2.8)–(2.10)), as the former does not considers the influence of background pressure on the ablation rate.[71]

4.1.3 Flow

Conservative form is used to account for the variations in density. The expanded equations in cylindrical coordinates are shown below.

$$\frac{\partial \rho}{\partial t} + \frac{1}{r}\frac{\partial}{\partial r}\left(r\rho u\right) + \frac{\partial}{\partial z}\left(\rho v\right) = 0 \tag{4.7}$$

$$\frac{\partial}{\partial t}\left(\rho u\right) + \frac{1}{r}\frac{\partial}{\partial r}\left(r\rho uu\right) + \frac{\partial}{\partial z}\left(\rho vu\right) = -\frac{\partial p}{\partial r} + \frac{1}{r}\frac{\partial}{\partial r}\left(r\tau_{rr}\right) - \frac{\tau_{\theta\theta}}{r} + \frac{\partial}{\partial z}\left(\tau_{zr}\right) \tag{4.8}$$

$$\frac{\partial}{\partial t}\left(\rho v\right) + \frac{1}{r}\frac{\partial}{\partial r}\left(r\rho uv\right) + \frac{\partial}{\partial z}\left(\rho vv\right) = -\frac{\partial p}{\partial z} + \frac{1}{r}\frac{\partial}{\partial r}\left(r\tau_{rz}\right) + \frac{\partial}{\partial z}\left(\tau_{zz}\right) \tag{4.9}$$

$$\tau_{rr} = 2\mu\frac{\partial u}{\partial r} - \frac{2}{3}\mu\left[\frac{1}{r}\frac{\partial}{\partial r}\left(ru\right) + \frac{\partial v}{\partial z}\right] \quad , \quad \tau_{\theta\theta} = 2\mu\frac{u}{r} - \frac{2}{3}\mu\left[\frac{1}{r}\frac{\partial}{\partial r}\left(ru\right) + \frac{\partial v}{\partial z}\right]$$

$$\tau_{zz} = 2\mu\frac{\partial v}{\partial z} - \frac{2}{3}\mu\left[\frac{1}{r}\frac{\partial}{\partial r}\left(ru\right) + \frac{\partial v}{\partial z}\right] \quad , \quad \tau_{rz} = \mu\left[\frac{\partial v}{\partial r} + \frac{\partial u}{\partial z}\right]$$

$$\begin{aligned}\frac{\partial}{\partial t}\left(\rho\bar{c_p}T\right)+\frac{1}{r}\frac{\partial}{\partial r}\left(r\rho u\bar{c_p}T\right)+\frac{\partial}{\partial z}\left(\rho v\bar{c_p}T\right) &= -\frac{Dp}{Dt} \\ &+ \frac{1}{r}\frac{\partial}{\partial r}\left(rk\frac{\partial T}{\partial r}\right)+\frac{\partial}{\partial z}\left(k\frac{\partial T}{\partial z}\right) \\ &+ \frac{j^2}{\sigma}+\frac{5}{2}\frac{k_B}{e}\left[j_r\frac{\partial T}{\partial r}+j_z\frac{\partial T}{\partial z}\right] \quad (4.10)\end{aligned}$$

Mass averaged velocity of the sublimated vapor at the interface is given as the boundary condition for axial velocity at the anode tip. The mass averaged velocity is obtained by dividing the evaporation mass rate with sum of vapor density and local density of fluid existing at the interface. Radial velocity and normal gradient of axial velocity are zero along the axis. Vent condition is specified at the bottom right corner or the chamber to maintain constant pressure inside the chamber.

Temperature on chamber walls is maintained constant at 350 K and normal gradient along the axis is considered to be zero. Heat flux boundary condition at the anode tip and plasma interface is given by Eq. (4.11). I is arc current and R_a is radius of anode. T_e is temperature of on coming electrons in eV, U_a is anode sheath voltage drop, ϕ_w is work function of anode material, and ΔH_{evap} is the latent heat of evaporation.

$$q_a'' = \frac{I}{\pi R_a^2}\left(2T_e + U_a + \phi_w\right) - \Delta H_{evap} \quad (4.11)$$

It has to be pointed out here that, the anodic arc was observed to be diffuse. Which means the flux of electrons in the plasma at the anode sheath edge is greater than the arc current flux.[72] In this scenario, the potential drop U_a must be negative in order to prevent the additional flux of electrons coming on to the anode.[73] Only high energy electrons enter the sheath. Anode sheath drop, U_a is obtained using Eq. (4.12). The electron flux j_{th} is the product of thermal velocity and electron density

at the anode sheath edge.

$$U_a = -T_e ln\left(\frac{j_{th}}{j_z}\right) \tag{4.12}$$

The enthalpy of the vapor leaving the anode tip, h_{vap}, given in Eq. (4.13) is added to the first cell of the fluid near the anode. Where, $c_{p,m}$ is the specific heat of the vapor mixture.

$$h_{evap} = \int_0^{T_a} c_{p,m} dT \tag{4.13}$$

Cathode sheath is not considered here, so, the heat flux at cathode tip-plasma interface is due to attachment of ions and thermionic electron emission from cathode tip. This is given in Eq. (4.14). U_{iz} and ϕ_{wc} are cathode material ionization potential and work function.

$$q_c'' = j_z \left(U_{iz} + \phi_{wc}\right) - j_{emission}\phi_{wc} \tag{4.14}$$

Equation (4.10) is solved throughout the domain, which includes conduction heat transfer between neutral gas and solid electrodes. It has to be noted here that, in Eqs. (4.11)–(4.14), all the variables are functions of radial coordinate and hence, these equations are used at all radial locations along the electrode-plasma interface to account for the two-dimensionality.

4.1.4 Species transport

Mass diffusion equation, Eq. (2.18) is employed to find the distribution of individual species inside the chamber. Mass fractions of individual species obtained from Eq. (2.2) as described in Section 4.1.2 are given as boundary condition at the anode tip and fluid interface. Zero normal gradient is considered on all the remaining boundaries. Binary diffusion coefficients with hard sphere model (Eq. (4.15)) are

used to account for the influence of temperature on the diffusion.[74;75] D_{AB} is diffusion coefficient of species A diffusing into species B. M_A and M_B are molecular weights of species A and B. σ_{AB} is rigid sphere collision diameter.

$$D_{AB} = \frac{2.63 \times 10^{-7}}{p\sigma_{AB}^2} \left(\frac{T^3 \left(M_A + M_B \right)}{2 M_A M_B} \right)^{1/2} \tag{4.15}$$

4.2 Solution procedure

For a given arc current and electrode gap, initially the electric potential is solved to obtain the potential field distribution. Then current is calculated and from current, magnetic field is obtained. Sublimation rate is calculated and individual mass fractions at the anode tip and fluid interface are obtained. Species diffusion is solved separately for C, Ni, and Y to obtain the respective mass fractions inside the fluid domain. Ionization fractions are calculated for the individual species using Eq. 4.1.4. Momentum and energy equations are solved using finite volume discretization and SIMPLER algorithm to obtain velocity distribution. Power law scheme is used to obtain the fluxes on the cell faces. Energy equation is then solved to obtain the temperature distribution. Using equation of state overall density distribution is obtained. This order is repeated till convergence is achieved at any time step. This procedure is repeated at all time steps to obtain the transient results. Thermophysical properties of individual species are considered from Refs.[76] Further details are given in Appendix D

4.2.1 Grid convergence

In this setup, Anode and cathode are of 6.35 and 12.5 mm in diameter, separated by 4 mm gap. Height and diameter of the chamber are 240 and 156 mm. Variable grid is considered throughout the domain. Finer grid is used near the electrodes where gradients are steep. The grid convergence is carried out for grid size varying in z

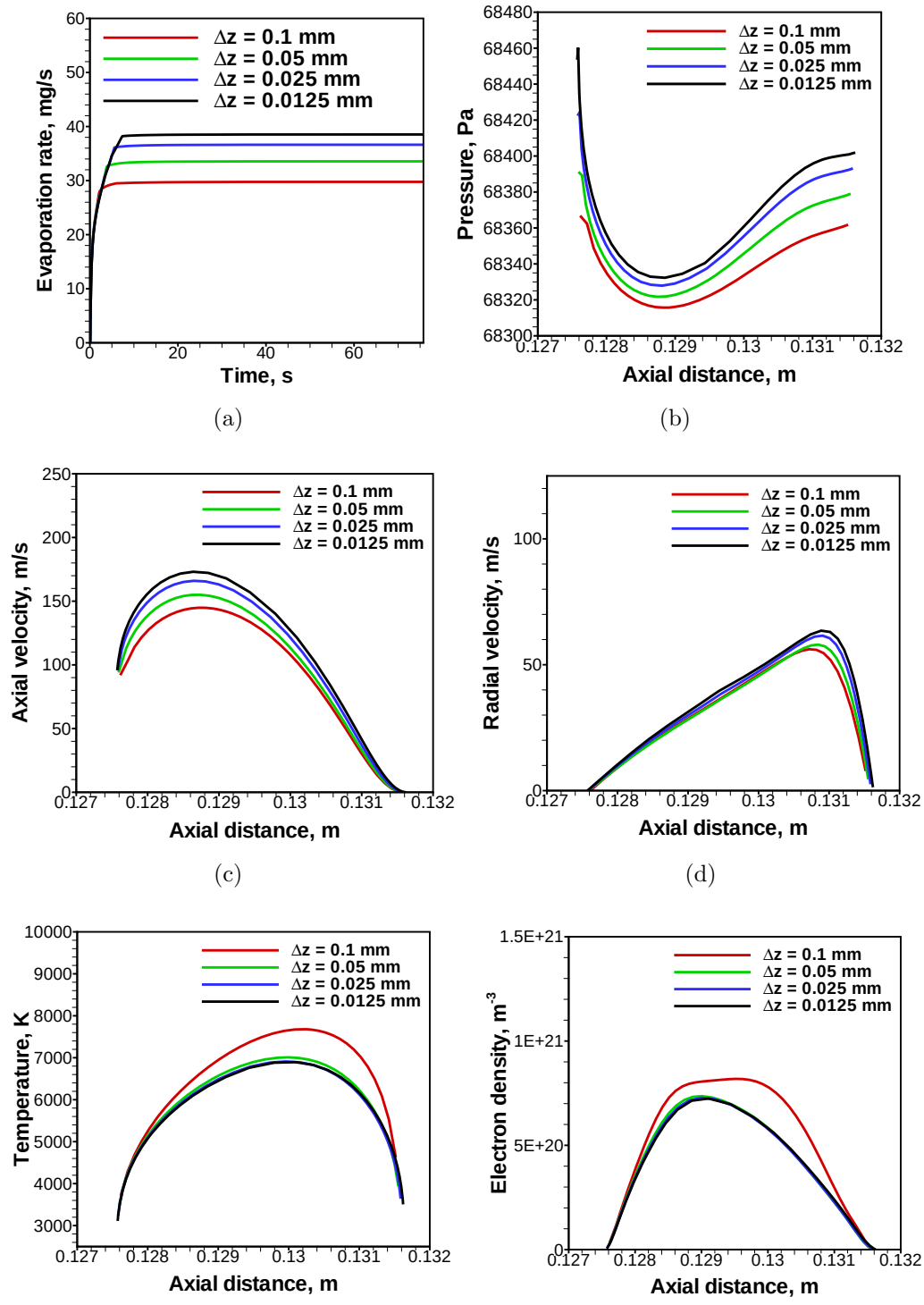

Figure 4.2: Grid convergence study for arc discharge chamber for $I = 60A$ and background helium pressure = $68\%Pa$. The variables are compared between the electrodes and $r = R_a/2$: (a) evaporation rate, (b) pressure, (c) Axial velocity, (d) Radial velocity, (e) Temperature, and (f) electron density

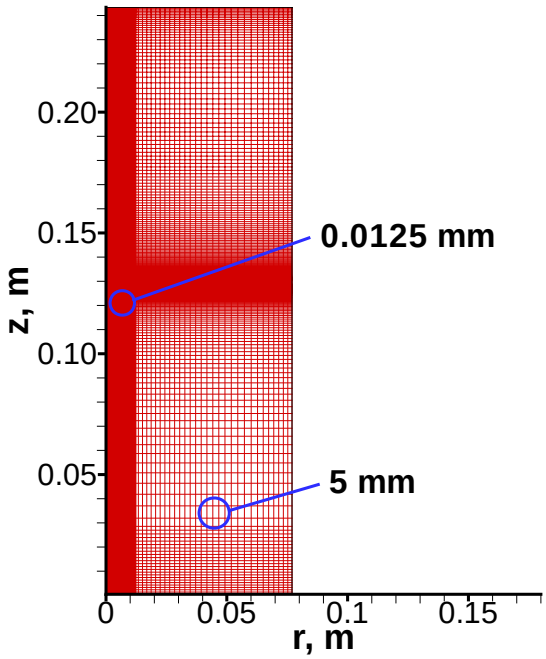

Figure 4.3: Grid for arc discharge chamber

direction near the inter electrode gap. The grid size is varied from 0.1 mm to 0.0125 mm. The plots for different variables in the inter-electrode gap are shown in Fig. 4.2. The converged grid is shown in Fig. 4.3.

4.3 Validation

Mass fractions of C, Ni, and Y in the anode are 0.66, 0.25, and 0.09 respectively. The background Helium pressure is 68 kPa. Sublimation rate is obtained for current varying from 10 to 100 A and compared with those from experiments[77] and one dimensional model[78]. The comparison plot is shown in Fig. 4.4(a). The present two dimensional model predicts slightly higher sublimation rate compared to the experiments while maintaining the similar trend of variation. Though one dimensional model showed better agreement for $I < 60A$, it could not capture the trend. The higher sublimation rate is due to the average saturation pressure model and Langmuir model as discussed in section 4.1.2.

Current voltage characteristics of 2D simulation are given in Fig. 4.4(b). Arc voltage is obtained by adding anode drop, U_a and inter-electrode plasma voltage, U_{pl}. Since the current flux variation at the cathode tip is non-linear, it is not straight forward to estimate the plasma voltage. Three methods are used to estimate the the plasma voltage from 2D simulation: 1) along the axis, potential at the cathode tip is subtracted from that existing at the anode tip (green curve) 2) using average conductivity calculated along the axis and arc current (blue curve) 3) using the average conductivity between the electrodes and arc current (blue curve with dot). Methods

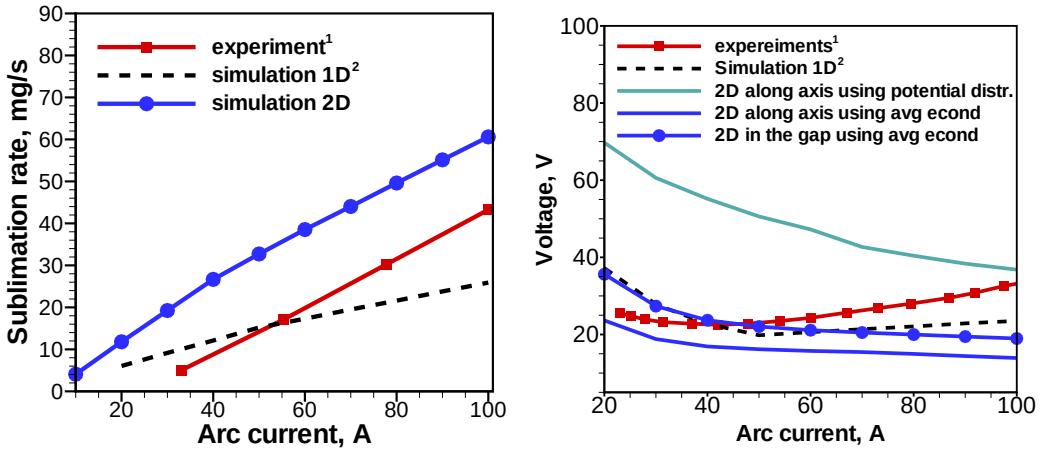

(a) (b)

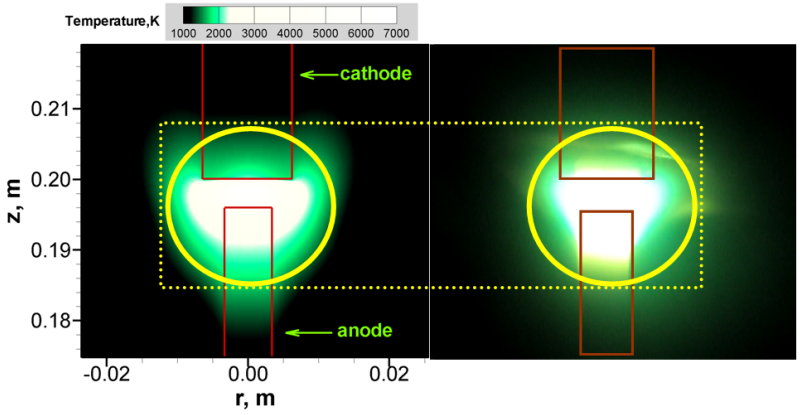

(c)

Figure 4.4: Validation of arc discharge results for current varying from 10 to 100 A: (a)Ablation rate, (b) current voltage characteristics, and (c) direct comparison of temperature contours with photo of experiment

1 and 2 show good agreement with experiment results at the high and low currents respectively. Whereas method 3 result is close to experiments in the medium range currents and 1D model calculations. It was observed from the experiments that the arc diameter increases with the increase of current. This variation in the arc diameter can not be seen in the 2D simulation due to average current flux boundary condition on the anode. However this variation is incorporated in the 1D simulations hence show better agreement with experiments.[79]

Figure 4.4(c) shows the direct comparison of temperature contours from the simulation (left hand side) with the photo of experiments. Total current is 60 A and the electrodes are separated by 4 mm. This 1:1 comparison is made for qualitative purpose alone. The similarity in the size and shape of the temperature contour plot and image can be noticed here.

4.4 Typical distribution of arc discharge parameters

The current flux and self induced magnetic field are shown in Fig. 4.5(a). The current flux is uniform near the anode tip and self adjusts to a lower value towards the cathode tip. The maximum value of self induced magnetic field is 0.0034 T. Pressure and density are shown in 4.5(b). Pressure of the gas inside chamber is 68280 Pa throughout the chamber except in the arc region. Pressure along the axis near the anode tip is 68480 Pa and decreases to 68350 Pa in the mid arc region and then increases to 68390 Pa at toward cathode tip due to flow stagnation. The density is low in he arc region due to high temperatures. Streamlines are shown in Fig. 4.5(c). The material evaporates from the anode with a velocity of 95 m/s and accelerates to 176 m/s in the mid arc region due to heat addition. The vapor then deflects away from the axis by cathode and velocity decreases gradually due to expansion. Vapor velocity is 20 m/s at distance of 20 mm from the axis. In addition, the deflected vapor separates into two recirculation regions after hitting the chamber wall. Some

of the gas leaves the chamber through the vent to maintain constant pressure.

Figures 4.6(a) and 4.6(b) show the density distribution of neutral species C, Ni, Y and their ions in the arc discharge chamber. The highest values of density existing at the anode tip are 4.2×10^{22}, 3.2×10^{21}, and 7.8×10^{20} m^{-3} for C, Ni, and Y, respectively. As expected, the density of carbon in the plasma exceeds that of the catalyst. The transport of species below the arc is mainly due to diffusion, whereas the diffusion and convection ensure the transport above the arc. The diffusion coefficient increases with the temperature; since the temperature in the fluid below the anode tip is high due to conduction from the anode lateral surface, the downward diffusion of species is observed in this area. The transport in radial direction is mainly due to convection. The highest densities of ions are 1.9×10^{20}, 5.5×10^{20}, and 2.6×10^{20} m^{-3} respectively for C^+, Ni^+, and Y^+. It is interesting to note that number density of C^+ is lowest though it has highest neutrals density. This is due to its high ionization potential. Out of these three species, Y has the lowest ionization potential and hence more Y^+ are seen just outside the arc, where temperatures are not sufficient to ionize C and Ni. Helium background gas has even higher ionization potential so its ionization is negligible throughout the chamber. Figure 4.6(c) illustrates the calculated distributions of temperature and electron density in the discharge with the highest numbers,7020 K and 7.5×10^{20} m^{-3} respectively, observed in the inter-electrode gap. The disk like radial distribution of temperature is due to convection.

The flow parameter distribution for I = 100 A of arc current is shown in Fig. 4.7. Anode evaporation rate increases due to higher energy deposition. As a result, the species density and temperature increase inside the chamber. Figure 4.7(a) shows the increased spreading of neutrals in all directions. The peak density of neutrals is 6.56×10^{22}, 5.02×10^{21}, and 1.21×10^{21} respectively for C, Ni, and Y respectively. The peak densitis of C^+, Ni^+, and $Y+$ (Fig. 4.7(b)) are 7.31×10^{20}, 9.89×10^{20}, and 4.25×10^{20} respectively. An increment of ($\approx 2mm$) in the size of plasma region can

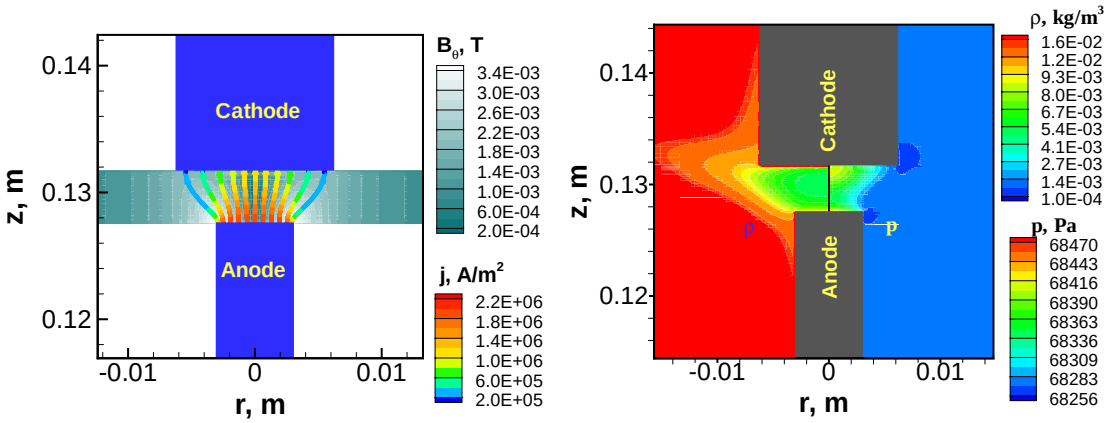

(a) (b)

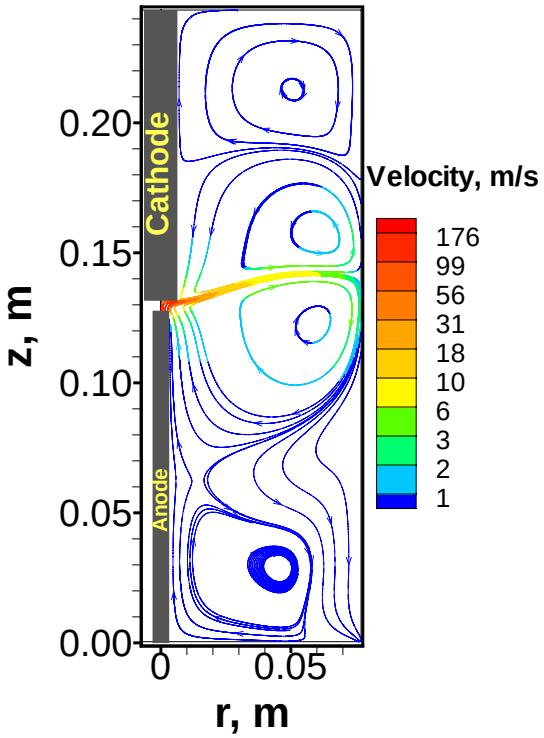

(c)

Figure 4.5: Typical distribution of parameters for I=60 A: (a)current flux lines with magnitude and self induced magnetic field contours, (b) pressure contours on the right hand side and density contours on the left hand side, and (c)streamlines with magnitude

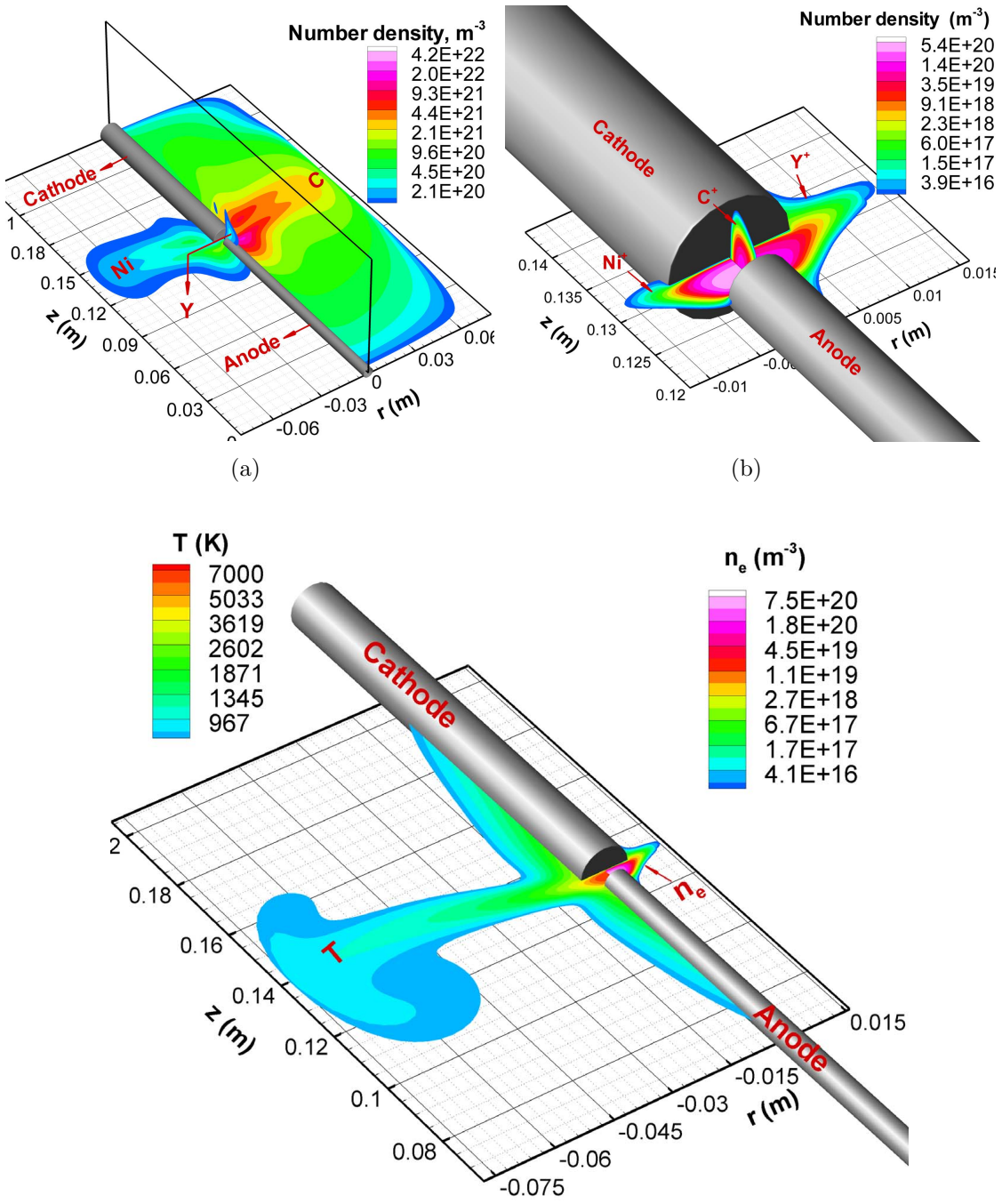

Figure 4.6: Species and temperature distribution in arc discharge for I=60 A: (a)Neutrals carbon, Nickel and Yttrium on the right, left and vertical planes, (b) Ions, and (c) Temperature and electron density distribution

be observed. The peak temperature in the arc region (Fig. 4.7(c))is 8033 K which is 1000 K greater than that observed for I = 60 A case. Slight reduction in the thickness

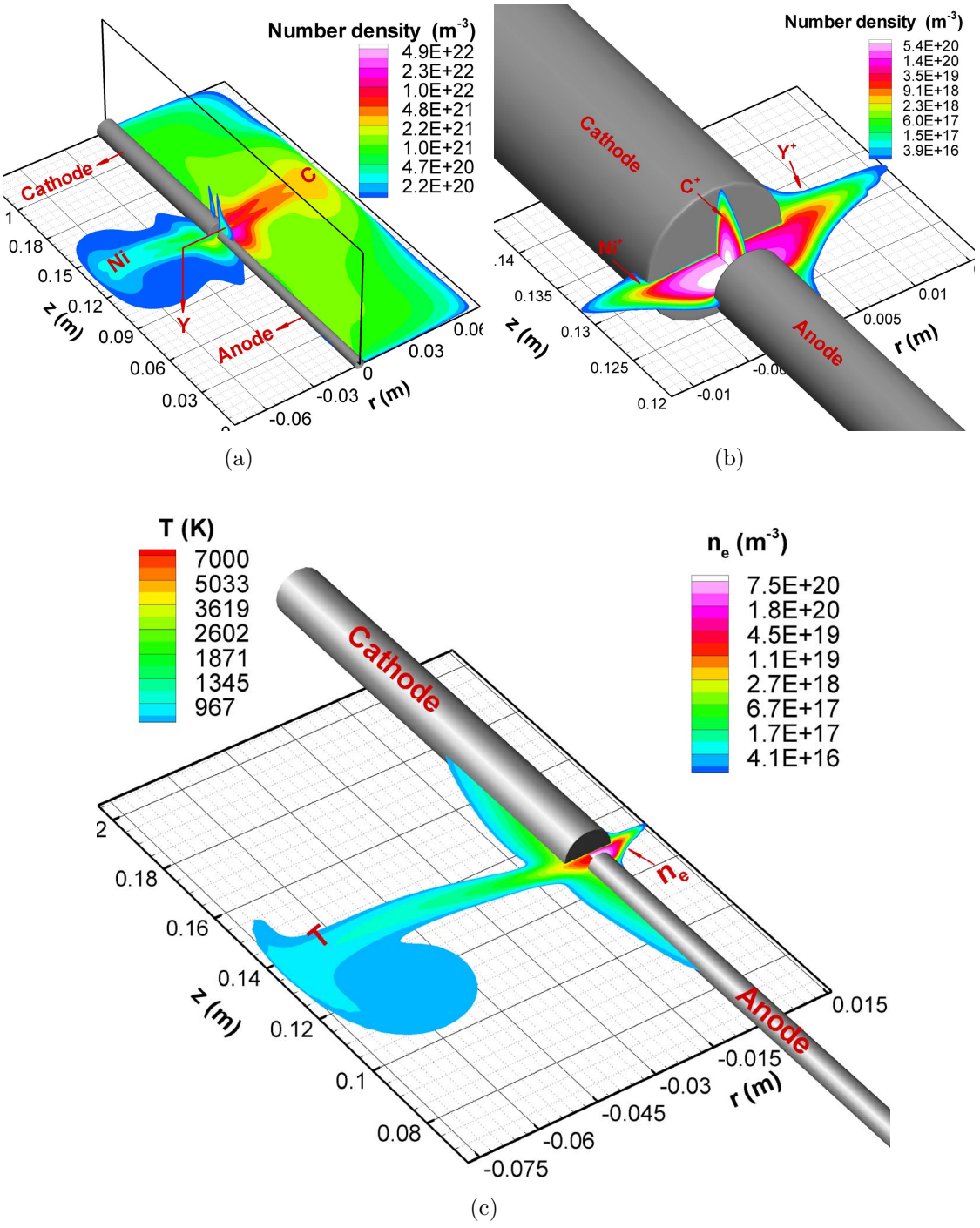

Figure 4.7: Species and temperature distribution in arc discharge for I=100 A: (a)Neutrals carbon, Nickel and Yttrium on the right, left and vertical planes, (b) Ions, and (c) Temperature and electron density distribution

of the disk-like structure is noticeable, which is due to the increased flow speed. The peak density of electrons, for this case, is 1.6×10^{21}.

4.5 Nanoparticle growth region

In this section, an attempt is made to identify and outline the probable location of nanotube growth, directly from the simulation results. Majority of $MWNT$s are found in the soft core of the cathode deposit while $SWNT$s are found in the collaret, lateral surface of the cathode, upper wall of the chamber and in the web suspended between cathode and chamber walls.[80;81] It was also observed that, the cathode deposit has negligible amounts of Ni, while it is high inside the soot deposited on the electrode lateral surfaces and in the web.[82] The temperature distribution in Fig. 4.6(c) also shows that temperature inside the arc region is high for Ni clusters to form. It can also be deduced that arc temperature is high enough to evaporate the CNT even if formed. Since cathode deposit is not simulated in this work, the other locations of the nanotube growth are explored. The remaining possibilities are growth on the electrode walls, chamber walls and in the vapor just outside the arc. Three major theories were suggested for the growth of nanotubes: open ended model[83] , two step growth model[84] , and root-growth model.[85] Either one or all of the three mechanisms may contribute for the growth. Nevertheless, the root growth model is considered here, due to the presence of large Ni clusters outside the arc region. It was shown analytically that growth rate of nanotubes is terminated due to the solidification of Ni clusters.[86] By considering the solidification point $\approx 1730K$ and condensation point $\approx 3180K$, the region of nanotube growth can be outlined using the isothermal lines, directly from the simulation.

The probable growth region in vapor is shown in Fig. 4.8 for $I = 20$, 60, and 100 A. The outlined region also shows the possibility of nanotube growth on the walls of the electrodes. It can be deduced now that, the clusters grown in this region will

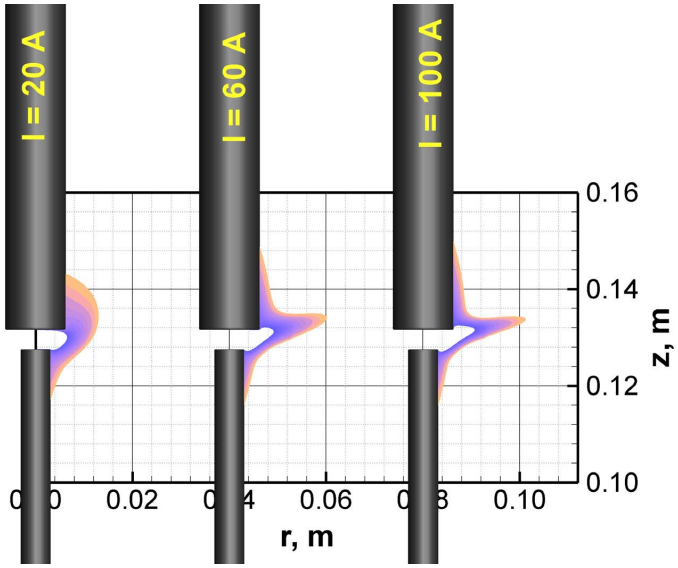

Figure 4.8: Growth region of nanoparticles for arc current I =20, 60, and 100 A

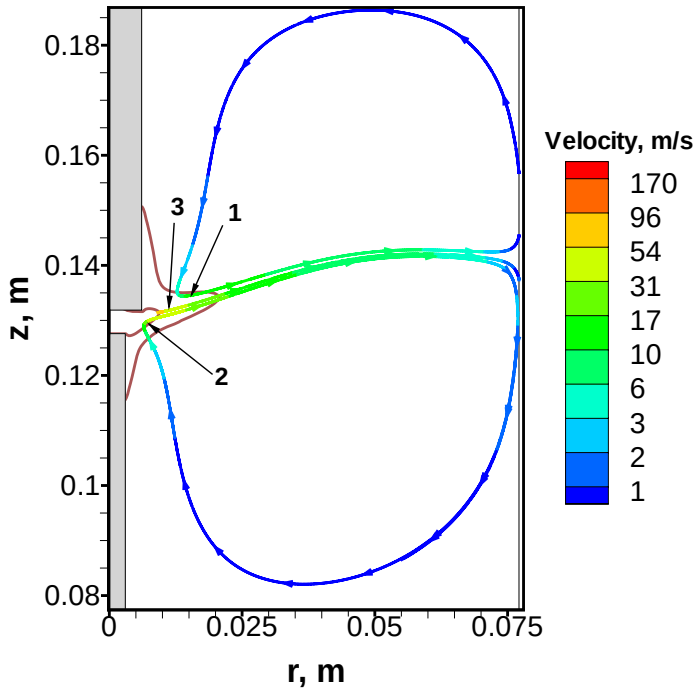

Figure 4.9: Nanoparticle path in discharge chamber. Growth models are used along the streamlines within the growth region.

be transported away due to convection and buoyancy, and deposited on the chamber walls. Cluster length and growth rate can now be estimated from the C and Ni densities in the outlined region, by employing flux balance models[87]. Arc discharge

parameters can be optimized, to increase the cluster length, by carrying parametric studies.

The path of nanoparticle in the chamber has to be traced in order to extract the vapor density and temperature local to the particle, which contribute to its growth. Since the particle size varies from nanometer to micrometer, they can be conveniently assumed to follow the streamlines of the flow. Figure. 4.9 shows the streamline for I=60 A case. Streamlines 1, 2 and 3 represent the typical flow pattern in the growth region. Nanoparticle growth models can be used along these streamlines, in the probable growth region, to estimate the particle size.

4.6 Nanoparticle growth model

The first approximation growth models used here are based on thermodynamics and surface diffusion. Two models are used: one for the spherical Ni cluster growth and the second for the growth of $SWNT$. Based on the experiments, the possibility of formation of compound and composite materials is neglected. Vapor flux contributing to the growth consists of neutrals and ions of metal and carbon. The nanoparticles are negatively charged due to high mobility of electrons, creating a sheath of thickness close to Debye length, and hence ions are attracted towards the nanoparticle as shown in Fig. 4.10. Nanoparticle of diameter d_{np} is surrounded by Debye sphere of radius $d_{np}/2 + \lambda_{De}$ consisting of non-neutral plasma. Ions enter the sheath with Bohm speed, v_B at the Debye sphere edge and create a focused flux that contributes to the growth of nanoparticle.[88;89;90] Neutrals, on the other hand, attach to nanoparticle with thermal velocity v_{th}. However, the focusing of ion flux vanishes if the collisions with the neutrals of background gas are dominant inside the sheath, which occurs for smaller mean free paths, i.e. $\lambda_{De} > \lambda_{mf}$.

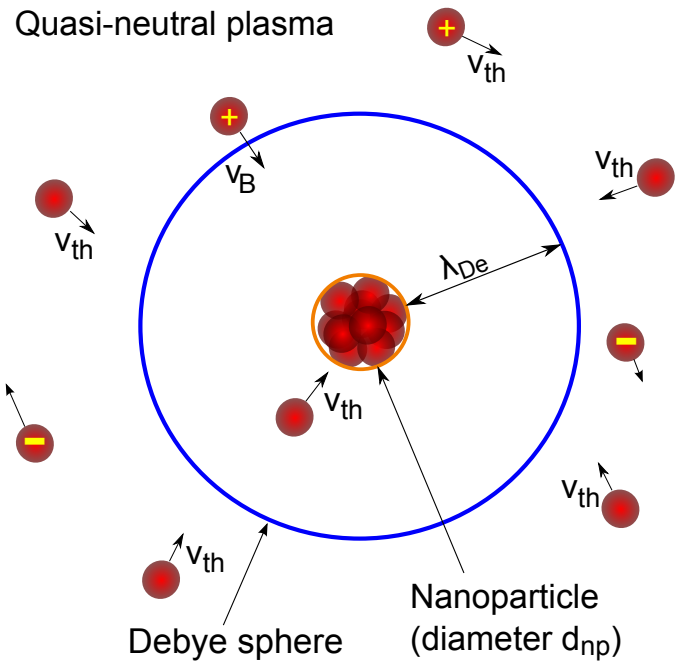

Figure 4.10: Nanoparticle growth in plasma. The cluster is negatively charged. The positive ions are focused on to the cluster from Debye sheath edge with Bohm velocity. Neutral approach the cluster with thermal velocity. Note: Not to the scale

4.6.1 Catalyst cluster

The growth of catalyst clusters can be obtained by first finding the critical cluster size using Gibbs free energy of formation of a spherical cluster of radius r given by Eq. (4.16).

$$\Delta G = 4\pi r^3 \sigma - 4\pi r^3 \frac{k_B T}{V_a} ln\,(S) \tag{4.16}$$

where, σ is surface energy (surface tension of isotropic materials), V_a is the atomic volume, and S is the saturation ratio given by the ratio of oncoming vapor pressure p_v and equilibrium pressure of the spherical cluster p_{sat}. Equation (4.16) has maxima at $r_c = 2\sigma V_a/[k_B T ln(S)]$ with a maximum energy of $\Delta G_c = (4/3)\pi r_c^2 \sigma$. The clusters with $r \geq r_c$ are stable and grows larger with further addition of vapor atoms. Further the probable number of critical clusters may be given using Boltzmann like

distribution function: $n_{r_c} = n_a exp[-\Delta G_c/(k_B T)]$.[91;92]

The growth model for the cluster moving along l is given by Eq. (4.17).[93]

$$\frac{dN}{dl} = 4\pi (r_c + r_a)^2 \frac{Q_{Ni}\beta}{v_l} \tag{4.17}$$

$$and\ r_c + r_a \approx r_c = \left(\frac{3}{4\pi}\right)^{1/3} N^{1/3} (2r_a)$$

where, N is the number of atoms in the cluster, r_a is the radius of atom,r_c is the radius of nanoparticle, and v_l is the velocity of the cluster. The coefficient β is the ratio of the vapor atoms contributing to the cluster to those arriving on to the cluster's surface. β can be calculated as $(R_{arrival} - R_{evap})/R_{arrival}$. Since arrival rate $R_{arrival}$ and evaporation rate R_{evap} are proportional to pressure of the vapor atoms and equilibrium pressure of the cluster, by assuming bulk vapor and cluster exist at the same temperature, $R_{evap}/R_{arrival} = S$. The equilibrium pressure p_{sat} of the spherical cluster surface can be calculated from its value corresponding to a flat surface using Kelvin's equation: $p_{sat} = p^* exp[2\sigma V_a/(rRT)]$.[94;95] The flux Q_{Ni} in Eq. (4.17), is obtained by adding neutral and ion fluxes as given in Eq. (4.18).

$$\begin{aligned} Q_{Ni} &= n\frac{1}{4}v_{th} + n_{Ni^+} v_B \left(\frac{r_c + \lambda_{De}}{r_c}\right)^2 \\ &= n\frac{1}{4}v_{th} \underbrace{\left[1 + \frac{n_{Ni^+}}{n}\frac{4v_B}{v_{th}}\left(1 + \frac{\lambda_{De}}{r_c}\right)^2\right]}_{\eta} \end{aligned} \tag{4.18}$$

Finally, Q_{Ni} from Eq. (4.18) is substituted in Eq. (4.17) to obtain the model for

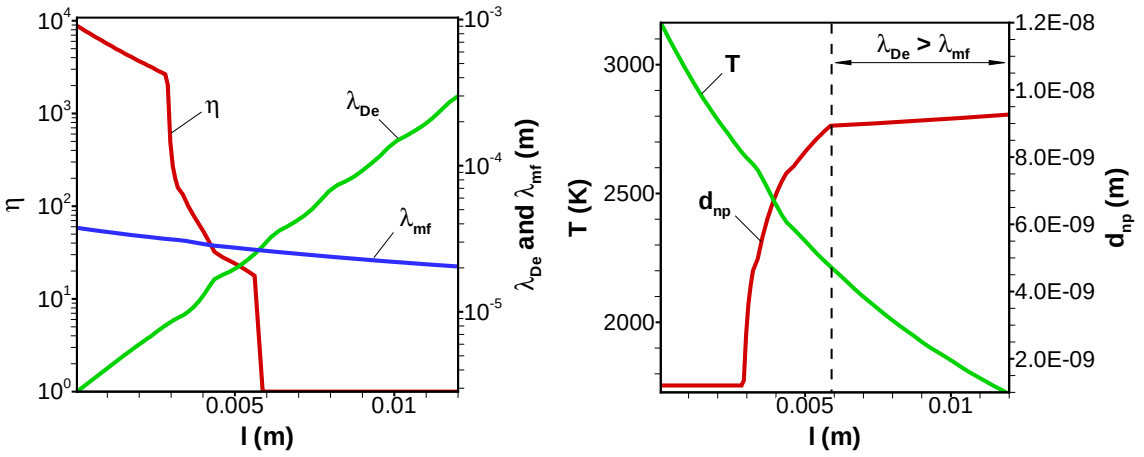

(a) (b)

Figure 4.11: Catalyst cluster growth calculations for I=60 A: (a)Effect of plasma on catalyst nanoparticle growth and (b) Diameter of the catalyst (Ni) nanoparticle

catalyst cluster growth as given in Eq: (4.19)

$$\frac{dN}{dl} = \pi \left(\frac{3}{4\pi}\right)^{2/3} (2r_a)^2 N^{2/3} \left(\frac{8k_B T}{\pi m_a}\right)^{1/2} \frac{n\beta}{v_l}\eta \tag{4.19}$$

Growth calculations performed for $I = 60A$ and 4 mm inter-electrode gap with a background pressure of 68 kPa are shown in Fig. 4.11. Figure 4.11(a) shows the effect of plasma on the growth of Ni cluster. The abscissa represents the distance along the streamline-3 (Fig. 4.9) starting from the isotherm corresponding to $3180K$ and ending at the isotherm corresponding to $1730K$. The coefficient η shown on the left ordinate, reflects the ratio of ion flux to neutral flux $(\eta - 1)$ contributing to the growth.

The ion density decreases as the particle moves away from the arc and hence η also decreases. Debye sheath thickness, λ_{De} shown on right ordinate, increases with the reduction in plasma density. The mean free path λ_{mf} decreases due to reduction in the temperature. At $l = 6mm$, the ion flux to the Ni cluster ceases completely as $\lambda_{De} > \lambda_{mf}$. The resultant growth is shown in 4.11(b). Though the flux is high in the region up to $l = 3mm$, cluster growth is negligibly small due high rate of evaporation,

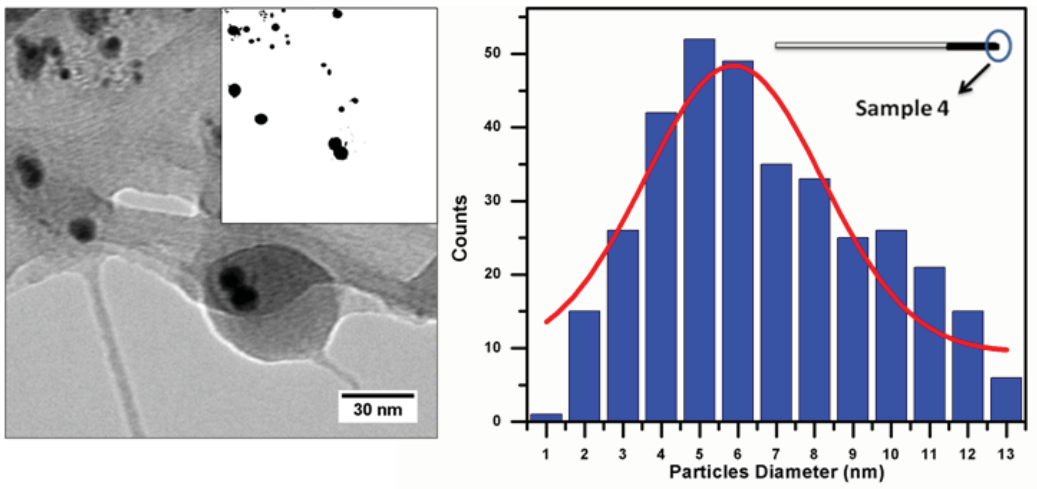

Figure 4.12: TEM images of Ni particles from experiments carried out by Jian et al.[96] High-magnification TEM image (200 Kx) is shown on LHS and diameter distribution of Ni particles is given on RHS.

R_{evap}. From $l = 3mm$ to $6mm$, steep increase in the particle diameter d_{np} is observed due to dominance of ion flux and beyond this point, the growth is very small due to cessation of ion flux. The final size of the Ni cluster is around $9.25nm$. It has to be noted here that, $SWNT$ starts growing on the Ni cluster simultaneously, which will reduce the Ni vapor flux to the cluster. The maximum reduction in the area may be 50%. It remains relatively unknown, exactly when the nanotube starts growing on the Ni cluster. Hence, on an average only 75% of the cluster area is considered to receive Ni vapor flux.

The TEM images and diameter distribution from the experiments given in Fig. 4.12 show that the catalyst cluster diameter varies from 2 to 12 nm in a sample taken at a distance of 20 mm from the arc axis.[96] The dark spots in Fig. 4.12(LHS) are the Ni particles surrounded by carbon nanoparticle-web. The size distribution of Ni particles is shown in RHS of Fig. 4.12. The highest number of particle are of 6 nm diameter and average size of the particles is 7.5 nm. The size of the Ni cluster obtained from the simulation at this location ($r = 20$ mm) is 9.2 nm.

4.6.2 SWNT

The effective flux of carbon atoms j_c contributing to the growth of nanotube is estimated using quasi-steady form of continuum surface diffusion model given by Eq. (4.20).[97;86]

$$D_s \frac{d^2 j_c}{dx^2} + Q_c - \frac{j_c}{\tau_a} = 0 \tag{4.20}$$

where D_s is surface diffusion coefficient, x is length coordinate along nanotube, Q_c is rate of carbon flux from the bulk vapor arriving on the nanotube surface, and τ_a is the time required to absorb carbon atoms. D_s and Q_c are estimated using Eqs.(4.21) and (4.22)respectively.

$$D_s = a^2{}_0 \nu exp\left(\frac{-\delta E_D}{k_B T}\right) \tag{4.21}$$

$$Q_c = n_C \frac{1}{4} v_{th} \underbrace{\left[1 + \frac{n_{C^+}}{n_C} \frac{4 v_B}{v_{th}} \left(1 + \frac{\lambda_{De}}{r_c}\right)\right]}_{\eta} \tag{4.22}$$

$$\tau_a = \frac{1}{\nu} exp\left(\frac{E_a}{k_B T}\right) \tag{4.23}$$

where a_0 is the inter atomic distance (jump distance) for carbon $0.14nm$, ν is the vibrational frequency of the atoms $= 3 \times 10^{13}$(value based on thermal vibrations), δE_D is the activation energy for surface diffusion carbon (0.3–1.8 eV), and E_a is adsorption energy (1.8–3.5 eV).[86]

Equation (4.20) is solved using boundary conditions $\frac{dj_c}{dx}|_{x=0} = 0$ and $-D_s \frac{dj_c}{dx}|_{x=L} = kj_c$ to obtain the flux distribution given in Eq. (4.24).

$$j_c(x) = Q_c \tau_a \left\{ \frac{\lambda_D cosh(x/\lambda_D)}{sinh(L/\lambda_D) + \frac{k\lambda_D}{D_s} cosh(L/\lambda_D)} + 1 \right\} \tag{4.24}$$

where $\lambda_D = \sqrt{D_S \tau_a}$ is diffusion length and $k = a_0/\tau_{inc}$ is the kinetic constant of incorporation. τ_{inc} is the incorporation time given by Eq. (4.25).

$$\tau_{inc} \approx \frac{1}{\nu} exp\left(\frac{\delta E_{inc}}{k_B T}\right) \tag{4.25}$$

The increase in the length of the nanotube moving along a line l inside the chamber can be estimated using Eq. (4.26).

$$\frac{dL}{dl} v_l = -\Omega D_s \frac{dj_c}{dx}|_{x=L} \tag{4.26}$$

The final equation for the growth of the nanotube is obtained by substituting for n_c from Eq. (4.24) in Eq. (4.26). The resulting expression is given in Eq. (4.27), which is solved using Runge-Kutta 4^{th} order method.[98]

$$\frac{dL}{dl} = \frac{1}{v_l} \frac{\Omega k Q_c \tau_a sinh\left(L/\lambda_D\right)}{sinh\left(L/\lambda_D\right) + \frac{k\lambda_D}{D_s} cosh\left(L/\lambda_D\right)} \tag{4.27}$$

Calculations performed for $I = 60A$ case are shown in Fig. 4.13. An average value is considered for adsorption energy ($E_a = 2.7eV$) as Eq. (4.27) does not account for radius and chirality of nanotube. The activation energy corresponding to the lower limit ($\delta E_d \approx 0.3eV$) is considered and $\delta E_{inc} \approx \delta E_d$. Figure 4.13(a) shows that, $\eta \approx 1$, for nanotube growth, throughout the growth region even though $\lambda_{De} < \lambda_{mf}$up to $l = 6mm$. This means the ion flux no longer contributes to the growth of nanotube, which is evident from Fig. 4.13(b). The ratio of ion density to neutrals density of carbon is negligibly small ($< 10^{-11}$) even the Debye sheath increases the collecting area. The reason for low ion flux is high ionization potential of carbon. Figure 4.13(c) shows the length of SWNT as it travels along the streamline in the temperature range $3180K$ to $1730K$. The nanotube grows up to $3.6\mu m$ long mostly due to neutrals flux.

The nanotube growth model, used here, can not specify the diameter, however the Ni cluster growth model can be used to specify the range of diameter. In fact it

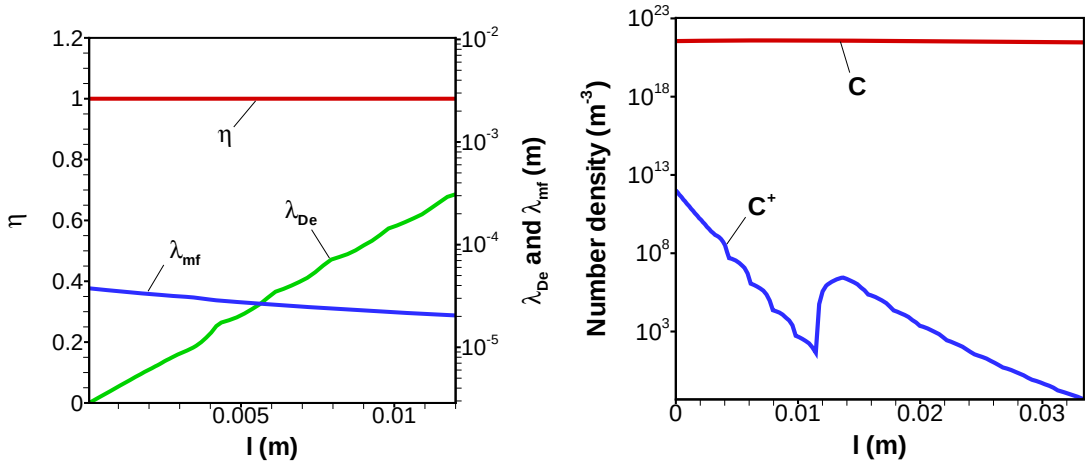

(a)

(b)

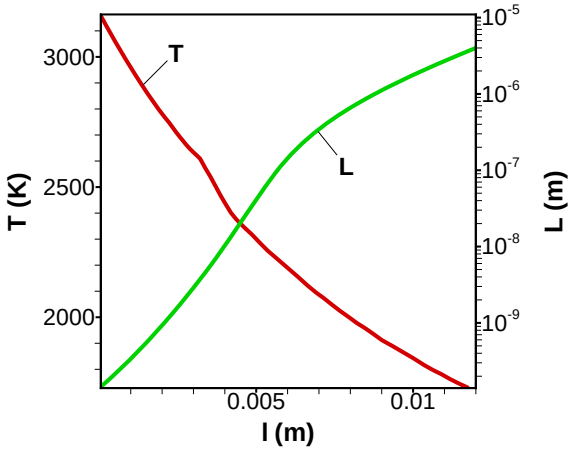

(c)

Figure 4.13: $SWNT$ growth calculations for I=60 A: (a) Effect of plasma on $SWNT$ growth, (b) Density of carbon neutrals and ions, and (c) length of SWNT

was shown that nanotubes grow as bundles as well on a single catalyst particle.[25;85] The HRTEM image of the bundle is shown in Fig. 4.14 The diameter of the $Ni-Y$ catalyst particle is 10 nm. Now, it can be deduced from Fig. 4.11(b),that the diameter of the single nanotube or a bundle of nanotubes varies from 2 to 9 nm. It has to noted that, Eq. (4.27) is suitable for single nanotube. In case of bundle growth, it is obvious that, overall length will be shorter as the same amount of surface flux has to be shared between all of the nanotubes in the bundle.

The SWNT length distribution from the experiments conducted for arc current

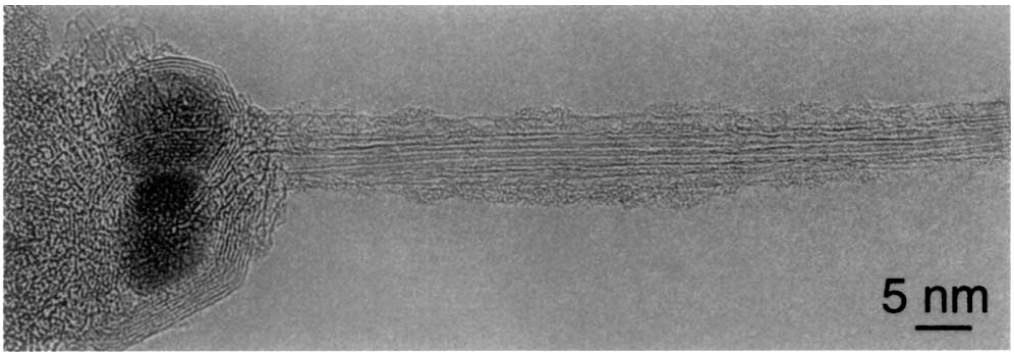

Figure 4.14: HRTEM image of SWNT bundle in arc discharges.[85] The diameter of the Ni-Y catalyst particle is 10 nm.

in the range of 70 to 80 A is shown in Fig. 4.15.[90] The SEM images in the left hand side inset shows the length measurement of single nanotube. The TEM image on the right hand side shows the bundle of nanotubes. The length distribution for nanotube growth without external magnetic field shows that, 50 % of the nanotubes are under 0.6 μm length while 90 % are less than 1.3 μm. The SEM image shows the nanotube length up to 3.04 μm. The growth calculations performed for 70 A and 80 A are shown in Fig. 4.16. The SWNT length is 2.2 μm and 2.02 μm respectively for the arc currents 70 A and 80 A. The length predicted by the growth model falls in the upper 10 % of the observations from experiments.

4.7 Parametric studies

The growth of nanoparticles can be improved by 1) increasing the size of growth region, 2) increasing the density of contributing species ($Ni, Ni^+, C, and C^+$), and 3) decreasing the velocity of nanoparticle ($\approx$ fluid velocity). For a given configuration, contributing species density and velocity are interdependent as velocity is directly proportional to the evaporation rate. Though ion flux has a significant effect on the growth rate, density of C^+ may not increase without increasing the temperature above 4500 K, at which nanoparticle can not grow.

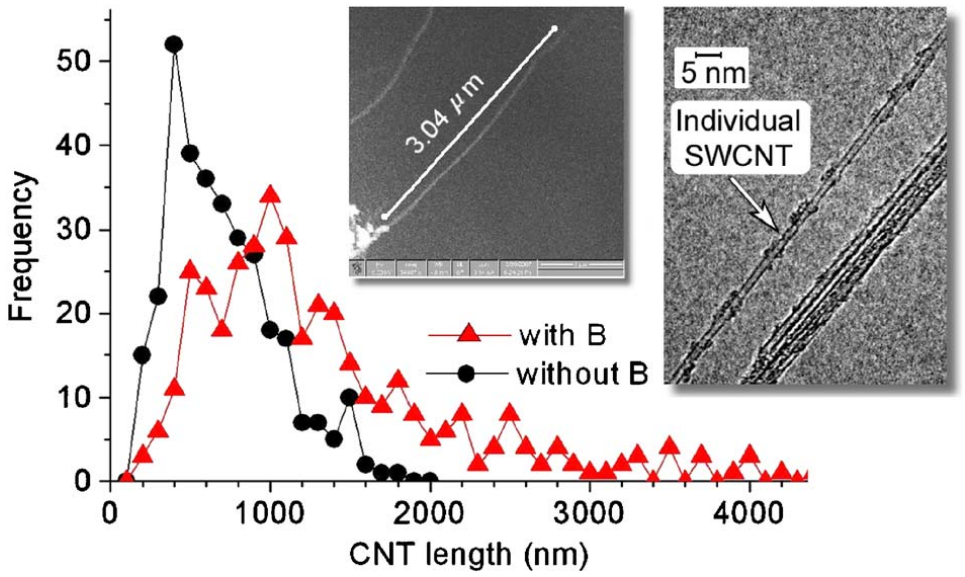

Figure 4.15: Carbon nanotube length distribution from experiments. LHS inset shows the SEM image for length measurement and RHS inset shows the TEM image of single nanotube and bundle of nanotubes.[90]

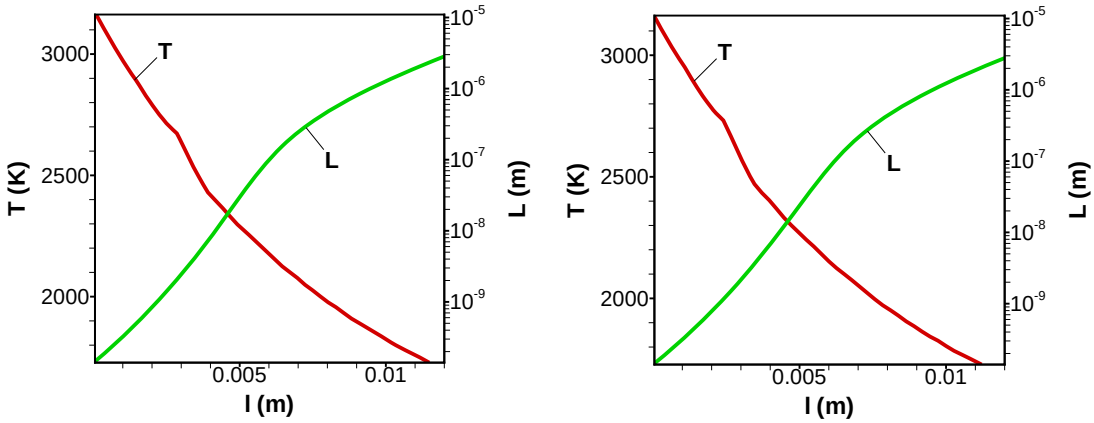

(a) (b)

Figure 4.16: $SWNT$ growth calculations: (a) $I = 70\ A$ (b) $I = 80\ A$

No.	I (A)	gap (mm)	p (kPa)	l (mm)	d_{np} (nm)	L (μm)
0	60	4	68	12	9.25	3.6
1	20	4	68	15	20	51
2	100	4	68	11	7.5	2
3	60	4	33	12.5	8	2.35
4	60	4	132	11	10.3	5.1
5	60	2	68	9.5	6.9	0.04
6	60	6	68	14	11.7	7

Table 4.1: Parametric study of Arc discharge

Keeping this in view, parametric studies are carried out by varying the arc current, background pressure, and inter-electrode gap. The results are listed in table 4.1. Columns 2,3, and 4 represents arc current, inter-electrode gap, and background pressure respectively. The length of path traversed by nanoparticle in the growth region (l) is shown in column 5. The size of Ni cluster (d_{np}) and length of $SWNT$ (L) are given in columns 6 and 7 respectively. The Parametric study No. 0, which is shown in Sections 4.6.1 and 4.6.2, is considered as reference for comparison. Parametric studies 1 and 2 are with arc current 20 A and 100 A. Studies 3 and 4 are with background pressure 30 kPa and 132 kPa respectively. Studies 5 and 6 correspond to electrode gap 2 and 6 mm.

The nanoparticle sizes, d_{np} and L decreases with the increase of arc current. This is mainly due to the increment in the flow velocity along the streamline as shown in Fig. 4.17(a). The velocity increases by 40 m/s compared to case-0. Though the density of species Ni, Ni^+, C, and C^+ is high due to the increased evaporation, the particles quickly move out the growth region. On the other hand reduction in arc current has the exactly opposite effect on the growth of nanoparticles. Though, a considerable increase in the particle sizes is observed, case-1 is avoided here as the error percentage in anode evaporation rate is high(Fig. 4.4(a)). Reduced background pressure (case-3) and inter-electrode gap (case-5) accelerates the flow as shown in Fig. 4.17(a) and decreases the species density as well. Hence the particle sizes also

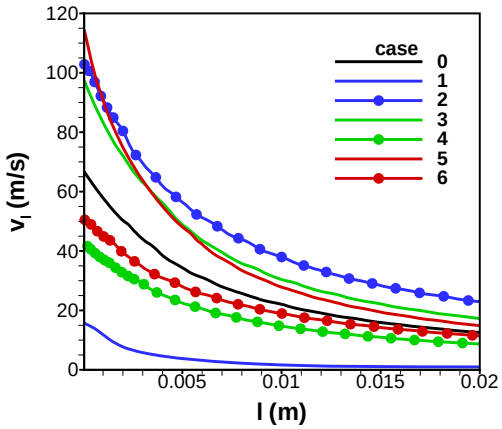

(a)

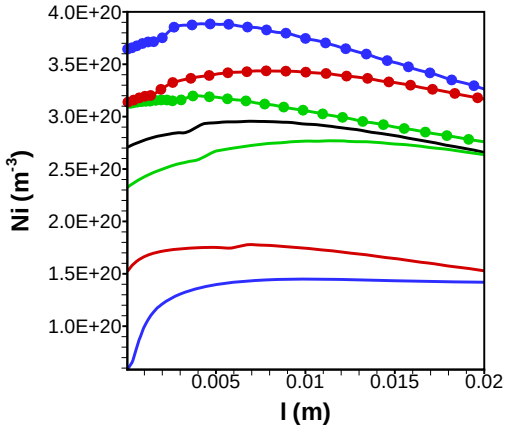

(b)

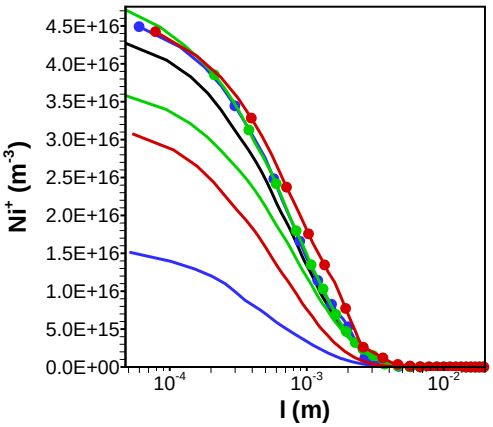

(c)

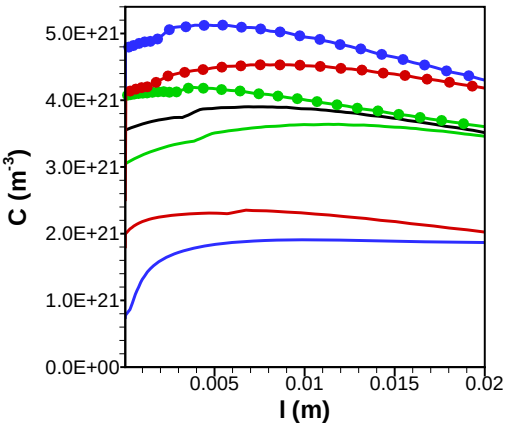

(d)

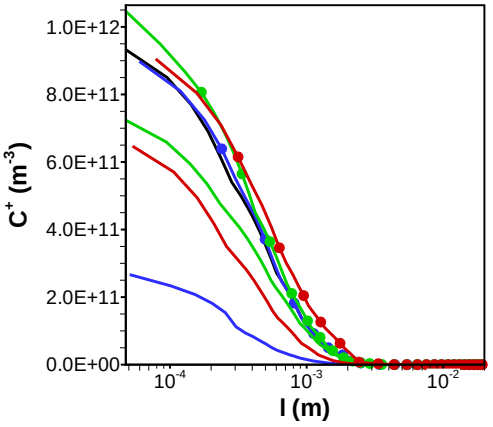

(e)

Figure 4.17: Species density along the streamline for parametric studies: (a) velocity and densities of (b) Ni, (c) Ni^+, (d) C, and (e) C^+

decrease. Increase in background pressure and electrode gap decelerate the flow and also results in the increase of species density along the streamline. The diameter of Ni cluster increases by 1.1 and 2.5 nm, and the length of SWNT increase by 1.5 and 3.4 μm respectively for the cases 4 and 6 in comparison to case-0.

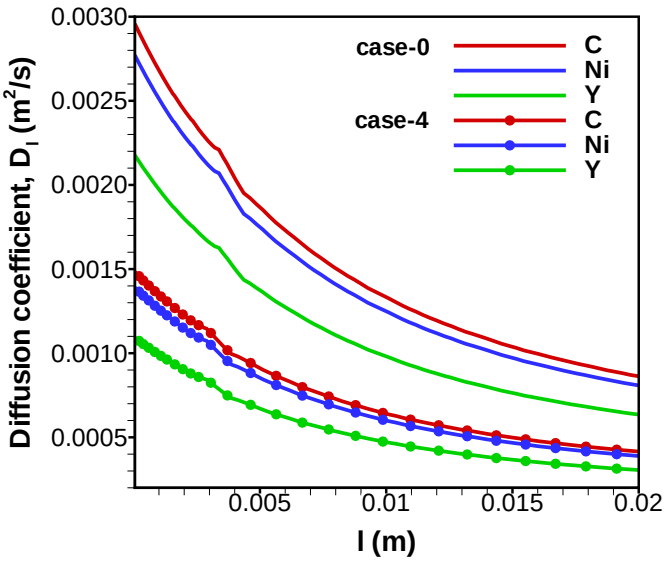

Figure 4.18: Effect of pressure on the diffusion coefficient of neutral species.

The increment of pressure and inter-electrode gap has limitations in terms of transformation to MWNT growth mode and arc stability. High pressure causes the arrival rate of vapor atoms to exceed the incorporation rate, which may result in the formation of MWNTS. The diffusion coefficient (Eq. (4.15)) is inversely proportional to pressure. Which confines the Ni and C atoms to a smaller region near the arc and increases the arrival rate. The comparison of diffusion coefficients of neutral species for case-0 and case-4 is shown in Fig. 4.18. As expected a clear reduction in the diffusion coefficient is observed. Besides this observation, the close match in the diffusion coefficients of C and Ni explains the selection of Ni as catalyst. In summary, the above parametric studies 1–6 show that the nanotube length increases by 40 to 90 %within the allowed variations in pressure and inter-electrode gap. Also, these parametric variations have less influence on the size of growth region or in other

words, the distance l traveled by the nanoparticle within the growth region. Hence an external means to increase the size of growth region has to be devised.

4.8 Hot chamber arc discharge

The growth region may be conveniently increased by maintaining the chamber walls at a higher temperature or by feeding preheated Helium gas. Keeping the same electrode configuration, the chamber may be replaced by a furnace possibly with $MoSiO_2$ heating elements to attain the required temperature. The reference case-0 is considered here with chamber wall temperature maintained at 1730 K (corresponding to the outer isotherm of the growth region). Figure 4.19 shows the growth region and streamlines in the hot chamber. Now, whole chamber serves as growth region.

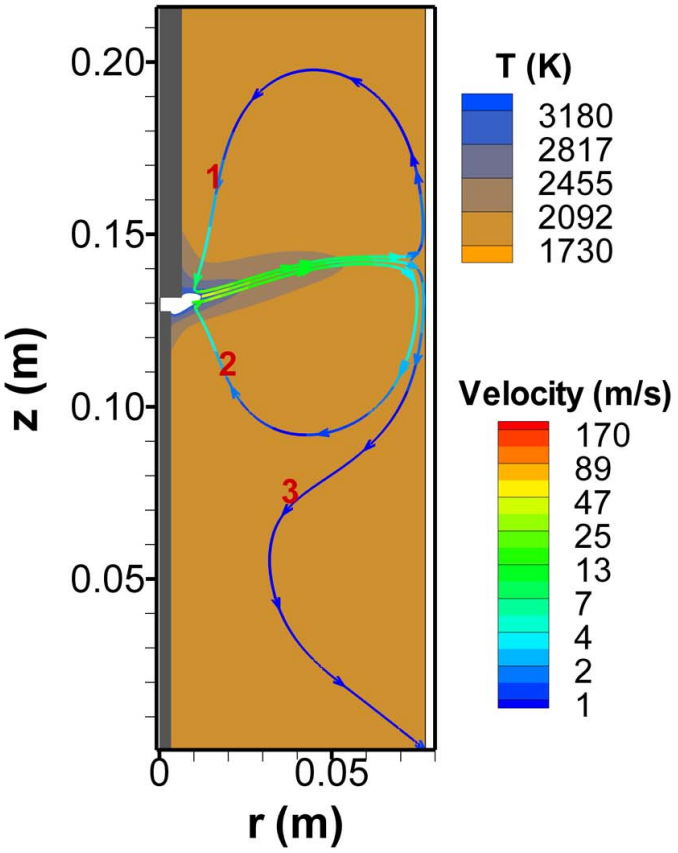

Figure 4.19: Growth region and streamlines in hot chamber arc discharge. The chamber walls are maintained at 1730 K

The nanoparticle growth calculations are shown in Fig. 4.20. The calculations are performed along the middle and bottom streamlines. The Ni cluster diameter, $SWNT$ length, and temperature are shown. Figure 4.20(a) shows that Ni diameter is 30 nm and $SWNT$ length is 0.25 mm for the growth along the middle streamline. The growth along bottom streamline for one circulation (4.20(b))is 35 nm Ni and 0.23 mm. The sizes of nanoparticles increase if the particles continue to circulate along the bottom streamline. Figures 4.20(c) and 4.20(d) show the growth for 2 and 5 loops along the bottom streamline. The Ni diameter and SWNT length are 50, 100 nm and 0.5, 1 mm respectively. The size of the Ni cluster may decrease if the proportion of Ni is decreased in the anode.

Figure 4.21 shows the streamlines in the hot chamber with modified anode composition. The Ni mas fraction is decreased from 0.25 to 0.03 and C mass fraction is increased from 0.66 to 0.87. Compared to the previous case (Fig. 4.19), the velocity of the vapor decreases from 170 m/s to 140 m/s. This is mainly due to the reduction in evaporation mass as a result of the increase in evaporation temperature of the anode with new material composition. The size of nanoparticle calculated along streamlines 3 and 2 are shown in Figs. 4.22(a) and 4.22(b) respectively. Comparing Figs. 4.20(a) and 4.22(a), the Ni particle size decreases from 30 nm to 20 nm while the length of $SWNT$ increases from 0.25 mm to 1.2 mm. Similar comparison between Figs. 4.20(b) and 4.22(b) shows that, Ni particle diameter decreases from 35 nm to 19 nm and the SWNT length increases from 0.23 mm to 0.4 mm.

In summary, hot chamber arc discharge method increases the size of the nanoparticles mainly due to the increase in the distance traveled by nanoparticles in the growth region. However, the growth models used in this study do not consider several other influential factors and physical phenomena. To name a few: temperature difference between nanoparticles and vapor atoms, variation in the activation energy, drag force on the particles, formation of web structure, and the possibility of transition to multi-

walled growth mode. Nevertheless, this method ensures the maximum possible growth of nanoparticles, under the influence of above mentioned factors, which are common to conventional arc discharges as well. However, numerical analysis using models for finding the distribution of nanoparticles is required to estimate of production rate.

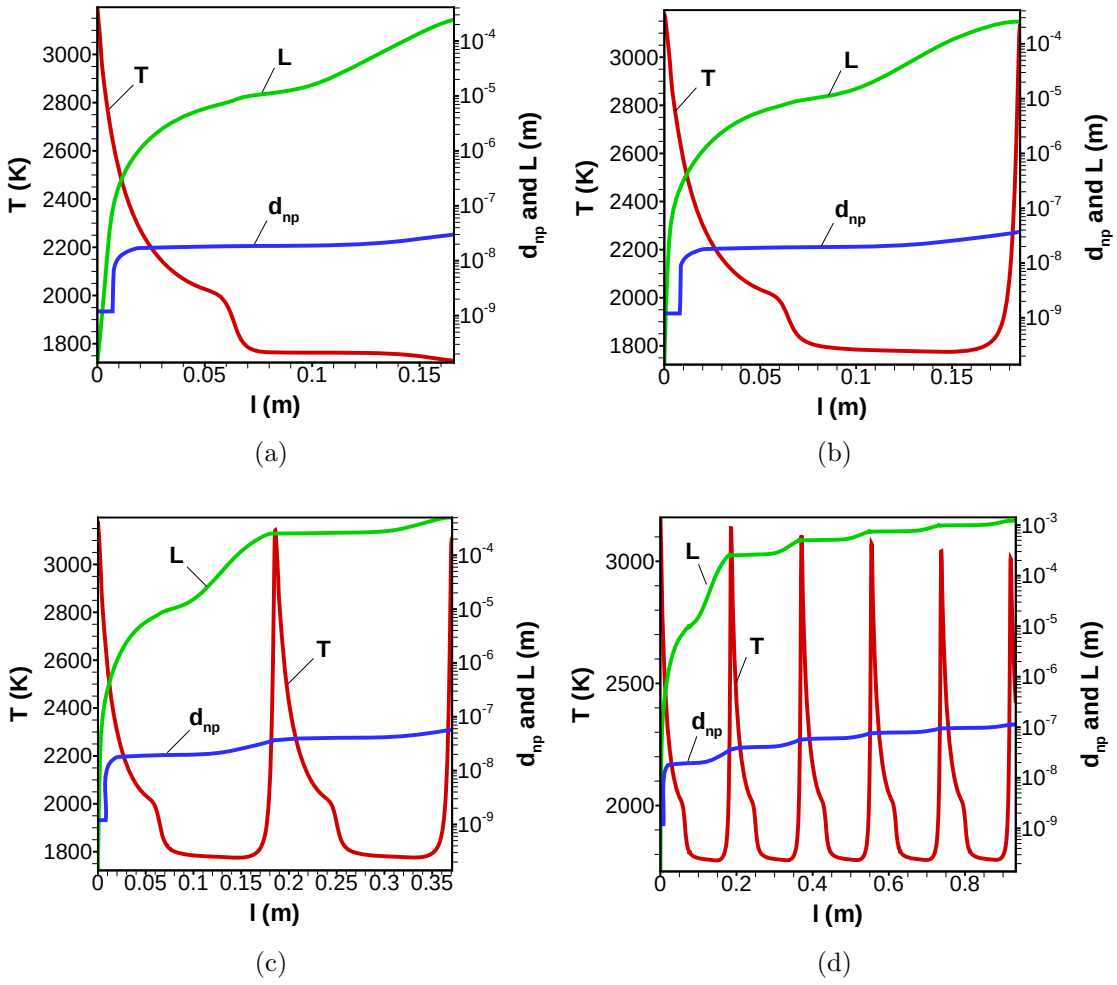

Figure 4.20: Nanoparticle growth in hot chamber arc discharge for an arc current of 60 A, 4 mm inter-electrode gap, and 68 kPa background pressure. The chamber walls are maintained at 1730 K: (a) along the middle streamline, (b) along the bottom streamline with 1 full circulation, (c) with 2 full circulations,and (d) with 5 full circulations.

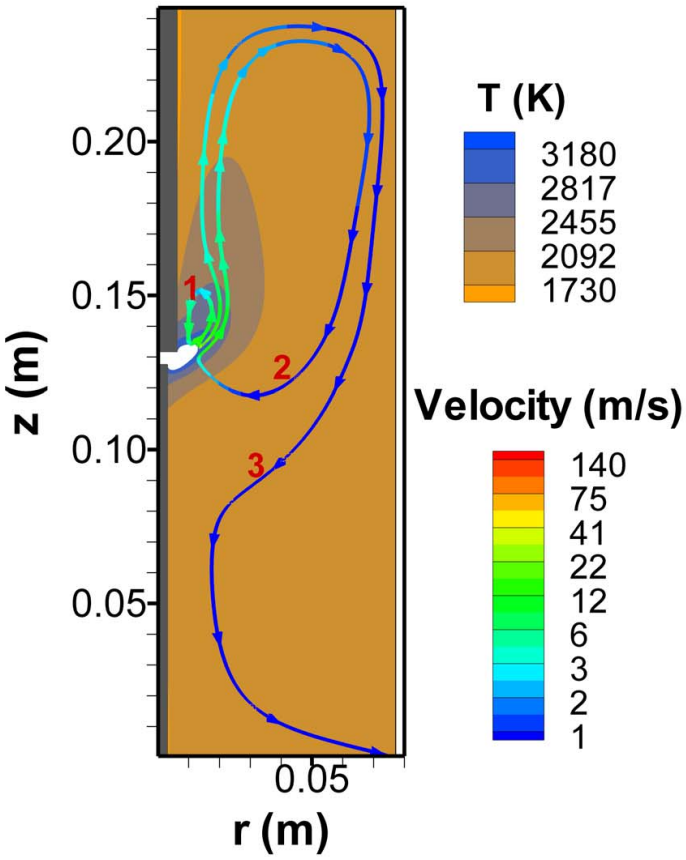

Figure 4.21: Growth region and streamlines in hot chamber arc discharge. Ni mass fraction is 0.03.

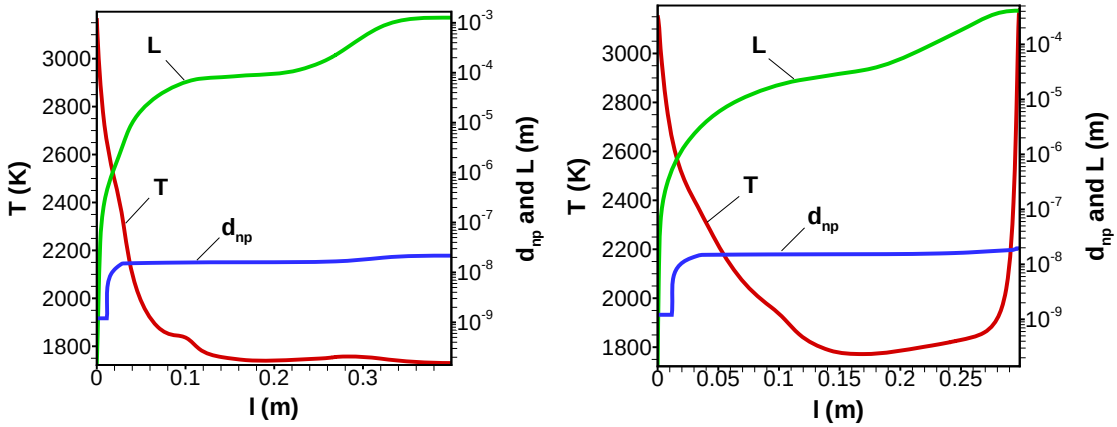

(a) (b)

Figure 4.22: Nanoparticle growth in hot chamber arc discharge for an arc current of 60 A, 4 mm inter-electrode gap, and 68 kPa background pressure. Ni mass fraction in the anode is decreased from 0.25 to 0.03 and carbon mass fraction is increased from 0.66 to 0.87: (a) along the streamline-3, (b) along the streamline-2 with one loop of circulation

Chapter V

Conclusions

1. Self-consistent model based on multi-layer analysis is proposed and numerical simulation procedure to find the thickness of the hydrodynamic layer (δ_{HL}) is presented. It is shown that δ_{HL} influences the results to a considerable extent. It is also demonstrated that the average speed of vapor at the outer edge of KL is much below the sonic speed. The proposed model is validated by direct comparison with experimental data and better agreement is observed compared to sonic speed model at higher fluences. By introducing actual variation of ionization cross section as a function of temperature, the model may be used for ablation with lower fluences.

2. Numerical analysis is carried out to obtain optimum wavelength for Laser based DEW to maximize the depth of ablation of three different materials Al, Cu, and Ti. The analysis shows that depth of ablation is high for the wavelength for which surface reflectivity lies in medium range values. The optimum wavelength changes from material to material. The optimum wavelength for Al is 850 nm. Two optimum wavelengths are noticed for Cu and Ti in low (10 50 J/cm^2) and high (50 100 J/cm^2) fluence ranges due the variation in material absorption coefficient. The optimum wavelengths for Cu are 360 nm and 460 nm in low and high fluence ranges. Similar values for Ti are 760 nm and 532 nm respectively.

The maximum depth of ablation of the three materials is found to be 1.1, 0.8, and 1.4 μ m respectively. Though Ti has superior heat sink properties compared to Al and Cu, it undergoes highest depth of evaporation.

3. Electrostatic sheath approach is found to be useful for the mitigation of communication attenuation during testing of DEW with relatively low laser fluences. Sheath characteristics change significantly with the change of fluence and target material. Transient sheath analysis carried out for Al and Ti targets shows that, electrostatic sheath can be used for ablation of Al targets with fluences up to 4 J/cm^2 and for Ti targets it is 1.3 J/cm^2 with a maximum bias voltage of 10 kV in 1 atm background pressure. It is found that the bias voltage requirement increases with the decrease of background pressure.

4. Arc discharge process is modeled for the synthesis of nanoparticles. The ablation rate of anode and current voltage characteristics are compared with experiments for $I = 60$ A current and 4 mm electrode gap with background pressure of 68 kPa. The evaporation rate obtained using the simulation, is consistent with the trend shown by the experiments but predicts higher evaporation rate. The evaporation rate is expected to decrease if Knudsen layer self consistent model is used. The current voltage characteristics of simulation fall in the range of experiment results.

5. The nanoparticle growth models are developed for particles moving in plasma. For $I = 60$ A current, with 4 mm inter-electrode gap in a He background of pressure of 68 kPa, the Ni cluster size obtained from the growth model is 9.2 nm while the TEM images of the experiment, from literature, for this case show that the average diameter is 7.5 nm with a maximum size of 12 nm. The $SWNT$ length for $I = 70$–80 A is found to be 2.2–2.05 μm. The measurement from the experiments for this current range showed that 10 % of the nanotubes

are longer than 1.3 μm with a maximum observed length of 3.04 μm. The numerical analysis showed that plasma has significant influence on the growth of Ni particles but not on the $SWNT$ growth.

6. Parametric studies are carried out for arc discharge chamber by varying the current, background pressure, and inter-electrode gap. Results showed 40 to 95 % increment in the nanotube length by increasing the background pressure and the inter-electrode gap.

7. Hot chamber arc discharge method is proposed to increase the nanoparticle growth region based on root growth mechanism. Growth analysis showed that, there is a possibility of synthesizing nanotubes up to two to three orders of magnitude longer than those synthesized in conventional arc-discharges with the same electrode configuration, arc current, and background pressure.

5.1 Contributions

In this work target evaporation and plasma formation are coupled in laser-target interaction and arc discharges to obtain the evaporation rate and species distribution self-consistently. The existing individual models corresponding to surface evaporation, fluid dynamics, electromagnetics, nucleation, and nanoparticle growth are coupled and a simulation software is developed. Simulation results are validated with experiments. Following are the more specific contributions:

1. Knudsen layer self-consistent model is successfully implemented to laser ablation. The issue for implementation was finding the thickness of hydrodynamic layer and the fluid properties at its outer edge. This issue is resolved in this work by introducing the parameter η to estimate the thickness of hydrodynamic layer (HL) based on ionization layer scale (Sec. 3.2.1).

2. Optimum wavelength of laser beam is obtained for the ablation of Al, Cu and Ti metals (Sec. 3.4). This is useful for energy optimization of laser beam.

3. Self-consistent arc discharge model is developed. Simulations are carried out without using the experimental data of anode evaporation as input to the fluid domain. Though the usage of experiment results as input seems to provide more accurate distribution of species, it is not possible to specify the velocity of the vapor. Flow velocity is an important parameter which influences the growth of nanoparticles.

4. The methodology for estimating the nanoparticle growth in dynamic plasma is specified (Sec. 4.5) and the growth model used for the stationary nanotubes[97] is extended to moving nanotubes (Eq. (4.27)). Nanoparticle growth analysis in arc discharges is carried out, for the first time, using the actual distribution of velocity, temperature, and species.

5. Hot chamber arc discharge method is proposed to maximize the growth of nanoparticles (Sec. 4.8). In comparison to the conventional arc discharge method, under the same conditions other than chamber wall temperature, nanoparticle growth analysis shows two to three orders of magnitude increase in the length.

5.2 Future work

1. The fluid solver has to be extended to 3D coordinates to simulate a) the interaction of multiple arcs b) rotating arc c) gliding arc, and d) the influence of external magnetic field. These studies are useful to enhance the growth of nanoparticles.

2. Vapor condensation on the walls has to be implemented to estimate the growth

of nanoparticles on solid surfaces, especially in the cathode deposit.

3. Knudsen layer self-consistent model has to be extended for two dimensional case with charged particles. This can be implemented to arc-discharges to improve the accuracy of anode evaporation rate calculations. This model is also quite useful for modeling plasma etching of semi-conductors and biological tissues.

4. Nanoparticle distribution models have to be developed for estimating size distribution and production rate. Thermostructural analysis of hot chamber configuration with mountings is required before testing the method in laboratory.

Bibliography

Bibliography

[1] Park, H., *Directed Energy Weapons Testing Raises Issues*, No. ada323342, Army Test and Evaluation Command Aberdeen Proving Ground Md, 1997.

[2] Weise, T., Jung, M., Langhans, D., and Gowin, M., "Overview of directed energy weapon developments," *Electromagnetic Launch Technology, 2004. 2004 12th Symposium on*, IEEE, 2004, pp. 483–489.

[3] Sprangle, P., Penano, J., Ting, A., Hafizi, B., and Gordon, D., "Propagation of Short, High-Intensity Laser Pulses in Air," *J. Directed Energy*, Vol. 1, No. 1, 2003, pp. 92.

[4] Semak, V. and Miller, T., "Modeling of Laser Charring and Material Removal in Fiberglass Materials," *J. Directed Energy*, Vol. 2, No. 1, 2006, pp. 97.

[5] Weichel, H., "Laser Beam Propagation in the Atmosphere, Vol," *TT03 of the Tutorial Text (SPIE, Bellingham, Wash., 1989)*.

[6] Amoruso, S., Armenante, M., Bruzzese, R., Spinelli, N., Velotta, R., and Wang, X., "Emission of prompt electrons during excimer laser ablation of aluminum targets," *Applied physics letters*, Vol. 75, 1999, pp. 7.

[7] Zel'dovich, Y. and Raizer, Y., *Physics of shock waves and high-temperature hydrodynamic phenomena*, Dover books on physics, Dover Publications, 2002.

[8] Lide, D. and Frederikse, H., *CRC handbook of chemistry and physics: a ready-reference book of chemical and physical data*, No. v. 76 in CRC Handbook of Chemistry & Physics, CRC Press, 1995.

[9] Bogaerts, A. and Chen, Z., "Effect of laser parameters on laser ablation and laser-induced plasma formation: A numerical modeling investigation," *Spectrochimica Acta Part B: Atomic Spectroscopy*, Vol. 60, No. 9-10, 2005, pp. 1280–1307.

[10] Barthélemy, O., Margot, J., Chaker, M., Sabsabi, M., Vidal, F., Johnston, T., Laville, S., and Le Drogoff, B., "Influence of the laser parameters on the space and time characteristics of an aluminum laser-induced plasma," *Spectrochimica Acta Part B: Atomic Spectroscopy*, Vol. 60, No. 7-8, 2005, pp. 905–914.

[11] Hudson, R., *Infrared system engineering*, Wiley series in pure and applied optics, Wiley-Interscience, 1969.

[12] Keidar, M., Kim, M., and Boyd, I., "Electromagnetic reduction of plasma density during atmospheric reentry and hypersonic flights," *Journal of Spacecraft and Rockets*, Vol. 45, No. 3, 2008, pp. 445–453.

[13] Keidar, M., Kundrapu, M., Kim, M., Boyd, I., Jones, C., and Mork, B., "Approaches to mitigate disruption of telemetry during directed energy testing," *44th Annual International Telemetering Conference, San Diego, CA, October 2008*, ITC, 2008, pp. 483–489.

[14] Kim, M., Keidar, M., and Boyd, I., "Electrostatic Manipulation of a Hypersonic Plasma Layer: Images of the Two-Dimensional Sheath," *Plasma Science, IEEE Transactions on*, Vol. 36, No. 4, 2008, pp. 1198–1199.

[15] Rybak, J. and Churchill, R., "Progress in reentry communications," *Aerospace and Electronic Systems, IEEE Transactions on*, , No. 5, 1971, pp. 879–894.

[16] Salvetat, J., Briggs, G., Bonard, J., Bacsa, R., Kulik, A., Stöckli, T., Burnham, N., and Forró, L., "Elastic and shear moduli of single-walled carbon nanotube ropes," *Physical Review Letters*, Vol. 82, No. 5, 1999, pp. 944–947.

[17] Martel, R., Schmidt, T., Shea, H., Hertel, T., and Avouris, P., "Single-and multi-wall carbon nanotube field-effect transistors," *Applied Physics Letters*, Vol. 73, 1998, pp. 2447.

[18] Choi, W., Chung, D., Kang, J., Kim, H., Jin, Y., Han, I., Lee, Y., Jung, J., Lee, N., Park, G., et al., "Fully sealed, high-brightness carbon-nanotube field-emission display," *Applied Physics Letters*, Vol. 75, 1999, pp. 3129.

[19] Baughman, R., Zakhidov, A., and De Heer, W., "Carbon nanotubes–the route toward applications," *Science*, Vol. 297, No. 5582, 2002, pp. 787.

[20] Keidar, M., Levchenko, I., Arbel, T., Alexander, M., Waas, A., and Ostrikov, K., "Magnetic-field-enhanced synthesis of single-wall carbon nanotubes in arc discharge," *Journal of Applied Physics*, Vol. 103, 2008, pp. 094318.

[21] Terrones, M., "Science and technology of the twenty-first century: synthesis, properties, and applications of carbon nanotubes," *Annual Review of Materials Research*, Vol. 33, No. 1, 2003, pp. 419–501.

[22] Volotskova, O., Levchenko, I., Shashurin, A., Raitses, Y., Ostrikov, K., and Keidar, M., "Single-step synthesis and magnetic separation of graphene and carbon nanotubes in arc discharge plasmas," *Nanoscale*, Vol. 2, No. 10, 2010, pp. 2281–2285.

[23] Levchenko, I., Volotskova, O., Shashurin, A., Raitses, Y., Ostrikov, K., and Keidar, M., "The large scale production of graphene flakes using magnetically-enhanced arc discharge between carbon electrodes," *Carbon*, 2010.

[24] Iijima, S. et al., "Helical microtubules of graphitic carbon," *nature*, Vol. 354, No. 6348, 1991, pp. 56–58.

[25] Journet, C., Maser, W., Bernier, P., Loiseau, A., Lamy de La Chapelle, M., Lefrant, S., Deniard, P., Lee, R., and Fischer, J., "Large-scale production of single-walled carbon nanotubes by the electric-arc technique," *Nature*, Vol. 388, No. 6644, 1997, pp. 756–757.

[26] Keidar, M., Shashurin, A., Li, J., Volotskova, O., Kundrapu, M., and Zhuang, T., "Arc plasma synthesis of carbon nanostructures: where is the frontier?" *Journal of Physics D: Applied Physics*, Vol. 44, 2011, pp. 174006.

[27] Ostrikov, K. and Murphy, A., "Plasma-aided nanofabrication: where is the cutting edge?" *Journal of Physics D: Applied Physics*, Vol. 40, 2007, pp. 2223.

[28] Keidar, M., Boyd, I., and Beilis, I., "On the model of Teflon ablation in an ablation-controlled discharge," *Journal of Physics D: Applied Physics*, Vol. 34, 2001, pp. 1675.

[29] Langmuir, I., "The vapor pressure of metallic tungsten," *Physical Review*, Vol. 2, No. 5, 1913, pp. 329.

[30] Anisimov, S., "Vaporization of metal absorbing laser radiation," *Soviet Journal of Experimental and Theoretical Physics*, Vol. 27, 1968, pp. 182.

[31] Keidar, M., Fan, J., Boyd, I., and Beilis, I., "Vaporization of heated materials into discharge plasmas," *Journal of Applied Physics*, Vol. 89, 2001, pp. 3095.

[32] Anisimov, S. and Khokhlov, V., *Instabilities in Laser-matter interaction*, CRC Press, 1995.

[33] Chen, F., *Introduction to Plasma Physics and Controlled Fusion: Plasma physics*, Introduction to Plasma Physics and Controlled Fusion, Plenum Press, 1984.

[34] Torrisi, L., Gammino, S., Andò, L., and Laska, L., "Tantalum ions produced by 1064 nm pulsed laser irradiation," *Journal of applied physics*, Vol. 91, No. 7, 2002, pp. 4685–4692.

[35] Gusarov, A., Gnedovets, A., and Smurov, I., "Gas dynamics of laser ablation: Influence of ambient atmosphere," *Journal of Applied Physics*, Vol. 88, 2000, pp. 4352.

[36] Dushman, S., *Scientific foundations of vacuum technique*, 1962 (various printings), Wiley, 1962.

[37] Zhang, Z., Han, Z., and Dulikravich, G., "Numerical simulation of laser induced plasma during pulsed laser deposition," *Journal of Applied Physics*, Vol. 90, 2001, pp. 5889.

[38] Toro, E., *Riemann solvers and numerical methods for fluid dynamics: a practical introduction*, Springer, 2009.

[39] Keidar, M., Boyd, I., and Beilis, I., "Ionization and ablation phenomena in an ablative plasma accelerator," *Journal of applied physics*, Vol. 96, 2004, pp. 5420.

[40] Zhang, Z. and Gogos, G., "Theory of shock wave propagation during laser ablation," *Physical Review B*, Vol. 69, No. 23, 2004, pp. 235403.

[41] Amoruso, S., Bruzzese, R., Vitiello, M., Nedialkov, N., and Atanasov, P., "Experimental and theoretical investigations of femtosecond laser ablation of aluminum in vacuum," *Journal of applied physics*, Vol. 98, 2005, pp. 044907.

[42] Colombier, J., Combis, P., Bonneau, F., Le Harzic, R., and Audouard, E., "Hydrodynamic simulations of metal ablation by femtosecond laser irradiation," *Physical Review B*, Vol. 71, No. 16, 2005, pp. 165406.

[43] Le Drogoff, B., Vidal, F., Von Kaenel, Y., Chaker, M., Johnston, T., Laville, S., Sabsabi, M., and Margot, J., "Ablation of aluminum thin films by ultrashort laser pulses," *Journal of Applied Physics*, Vol. 89, 2001, pp. 8247.

[44] Claeyssens, F., Henley, S., and Ashfold, M., "Comparison of the ablation plumes arising from ArF laser ablation of graphite, silicon, copper, and aluminum in vacuum," *Journal of applied physics*, Vol. 94, 2003, pp. 2203.

[45] Jeong, S., Greif, R., and Russo, R., "Shock wave and material vapour plume propagation during excimer laser ablation of aluminium samples," *Journal of Physics D: Applied Physics*, Vol. 32, 1999, pp. 2578.

[46] Colao, F., Lazic, V., Fantoni, R., and Pershin, S., "A comparison of single and double pulse laser-induced breakdown spectroscopy of aluminum samples* 1," *Spectrochimica Acta Part B: Atomic Spectroscopy*, Vol. 57, No. 7, 2002, pp. 1167–1179.

[47] Körner, C., Mayerhofer, R., Hartmann, M., and Bergmann, H., "Physical and material aspects in using visible laser pulses of nanosecond duration for ablation," *Applied Physics A: Materials Science & Processing*, Vol. 63, No. 2, 1996, pp. 123–131.

[48] Dou, K., Knobbe, E., Parkhill, R., and Wang, Y., "Surface texturing of aluminum alloy 2024-T3 via femto-and nanosecond pulse excimer laser irradiation," *Selected Topics in Quantum Electronics, IEEE Journal of*, Vol. 6, No. 4, 2000, pp. 689–695.

[49] Semerok, A., Salle, B., Wagner, J., and Petite, G., "Femtosecond, picosecond, and nanosecond laser microablation: Laser plasma and crater investigation," *Laser and Particle Beams*, Vol. 20, No. 1, 2002, pp. 67–72.

[50] Margreiter, D., Deutsch, H., and M
"ark, T., "A semiclassical approach to the calculation of electron impact ionization cross-sections of atoms: from hydrogen to uranium," *International Journal of Mass Spectrometry and Ion Processes*, Vol. 139, 1994, pp. 127–139.

[51] Kim, Y. and Stone, P., "Ionization of boron, aluminum, gallium, and indium by electron impact," *Physical Review A*, Vol. 64, No. 5, 2001, pp. 052707.

[52] Beilis, I., "Parameters of the kinetic layer of arc-discharge cathode region," *Plasma Science, IEEE Transactions on*, Vol. 13, No. 5, 1985, pp. 288–290.

[53] Krishnan, S. and Nordine, P., "Analysis of the optical properties of liquid aluminum," *Physical Review B*, Vol. 48, 1993, pp. 4130–4131.

[54] Child, C., "Discharge from hot CaO," *Physical Review (Series I)*, Vol. 32, No. 5, 1911, pp. 492.

[55] Keidar, M. and Brown, I., "Sheath expansion in a drifting, nonuniform plasma," *Journal of Vacuum Science & Technology B: Microelectronics and Nanometer Structures*, Vol. 17, 1999, pp. 2648.

[56] Farhat, S., Hinkov, I., and Scott, C., "Arc process parameters for single-walled carbon nanotube growth and production: Experiments and modeling," *Journal of Nanoscience and Nanotechnology*, Vol. 4, No. 4, 2004, pp. 377–389.

[57] Bilodeau, J., Pousse, J., and Gleizes, A., "A mathematical model of the carbon arc reactor for fullerene synthesis," *Plasma chemistry and plasma processing*, Vol. 18, No. 2, 1998, pp. 285–303.

[58] Hsu, K., Etemadi, K., and Pfender, E., "Study of the free-burning high-intensity argon arc," *Journal of Applied Physics*, Vol. 54, No. 3, 1983, pp. 1293–1301.

[59] Murphy, A., Tanaka, M., Yamamoto, K., Tashiro, S., Sato, T., and Lowke, J., "Modelling of thermal plasmas for arc welding: the role of the shielding gas properties and of metal vapour," *Journal of Physics D: Applied Physics*, Vol. 42, 2009, pp. 194006.

[60] Patankar, S., *Numerical heat transfer and fluid flow*, Series in computational methods in mechanics and thermal sciences, Taylor & Francis, 1980.

[61] Chapman, S. and Cowling, T., *The mathematical theory of non-uniform gases: an account of the kinetic theory of viscosity, thermal conduction, and diffusion in gases*, Cambridge Mathematical Library, Cambridge University Press, 1991.

[62] Itikawa, Y., "Effective collision frequency of electrons in atmospheric gases," *Planetary and Space Science*, Vol. 19, No. 8, 1971, pp. 993–1007.

[63] Frost, L., "Conductivity of seeded atmospheric pressure plasmas," *Journal of Applied Physics*, Vol. 32, No. 10, 1961, pp. 2029–2036.

[64] Dunn, G. and Eagar, T., "Calculation of electrical and thermal conductivities of metallurgical plasmas," *WRC Bulletin*, , No. 357, 1990.

[65] Itikawa, Y., "Momentum-transfer cross sections for electron collisions with atoms and molecules," *Atomic Data and Nuclear Data Tables*, Vol. 14, No. 1, 1974, pp. 1–10.

[66] Banks, P., "Collision frequencies and energy transfer electrons," *Planetary and Space Science*, Vol. 14, No. 11, 1966, pp. 1085–1103.

[67] Haidar, J., "Non-equilibrium modelling of transferred arcs," *Journal of Physics D: Applied Physics*, Vol. 32, 1999, pp. 263.

[68] Park, J., Heberlein, J., Pfender, E., Candler, G., and Chang, C., "Two-Dimensional Numerical Modeling of Direct-Current Electric Arcs in Nonequilibrium," *Plasma Chemistry and Plasma Processing*, Vol. 28, No. 2, 2008, pp. 213–231.

[69] Price, D., "Vapor pressure determination by thermogravimetry," *Thermochimica acta*, Vol. 367, 2001, pp. 253–262.

[70] Shpil'rain, E., Belova, A., Shkermontov, V., Mozgovoi, A., and Skovorod'ko, S., "Experimental Investigation of the Pressure of Saturated Vapors of Liquid Alloys of Alkali Metals at High Temperatures: Na–Cs System," *High Temperature*, Vol. 39, No. 4, 2001, pp. 629–633.

[71] Kundrapu, M. and Keidar, M., "Laser ablation of metallic targets with high fluences: Self-consistent approach," *Journal of Applied Physics*, Vol. 105, No. 8, 2009, pp. 083302–083302.

[72] Boxman, R. and Goldsmith, S., "Model of the anode region in a uniform multicathode-spot vacuum arc," *Journal of applied physics*, Vol. 54, No. 2, 1983, pp. 592–602.

[73] Beilis, I., Keidar, M., Boxman, R., and Goldsmith, S., "Theoretical study of plasma expansion in a magnetic field in a disk anode vacuum arc," *Journal of applied physics*, Vol. 83, 1998, pp. 709.

[74] Hirschfelder, J., Curtiss, C., and Bird, R., *Molecular theory of gases and liquids*, Structure of matter series, Wiley, 1954.

[75] Morgan, J. and Schiff, H., "Diffusion coefficients of O and N atoms in inert gases," *Canadian Journal of Chemistry*, Vol. 42, No. 10, 1964, pp. 2300–2306.

[76] Pousse, J., Chervy, B., Bilodeau, J., and Gleizes, A., "Thermodynamic and transport properties of argon/carbon and helium/carbon mixtures in fullerene synthesis," *Plasma chemistry and plasma processing*, Vol. 16, No. 4, 1996, pp. 605–634.

[77] Shashurin, A., Keidar, M., and Beilis, I., "Voltage-current characteristics of an anodic arc producing carbon nanotubes," *Journal of Applied Physics*, Vol. 104, No. 6, 2008, pp. 063311–063311.

[78] Keidar, M. and Beilis, I., "Modeling of atmospheric-pressure anodic carbon arc producing carbon nanotubes," *Journal of Applied Physics*, Vol. 106, No. 10, 2009, pp. 103304–103304.

[79] Keidar, M., Shashurin, A., Volotskova, O., Raitses, Y., and Beilis, I., "Mechanism of carbon nanostructure synthesis in arc plasma," *Physics of Plasmas*, Vol. 17, 2010, pp. 057101.

[80] Meyyappan, M., *Carbon nanotubes: science and applications*, CRC Press, 2005.

[81] Waldorff, E., Waas, A., Friedmann, P., and Keidar, M., "Characterization of carbon nanotubes produced by arc discharge: Effect of the background pressure," *Journal of applied physics*, Vol. 95, 2004, pp. 2749.

[82] Yudasaka, M., Sensui, N., Takizawa, M., Bandow, S., Ichihashi, T., and Iijima, S., "Formation of single-wall carbon nanotubes catalyzed by Ni separating from Y in laser ablation or in arc discharge using a C target containing a NiY catalyst," *Chemical physics letters*, Vol. 312, No. 2-4, 1999, pp. 155–160.

[83] Iijima, S., Ajayan, P., and Ichihashi, T., "Growth model for carbon nanotubes," *Physical review letters*, Vol. 69, No. 21, 1992, pp. 3100–3103.

[84] Zhou, D. and Chow, L., "Complex structure of carbon nanotubes and their implications for formation mechanism," *Journal of applied physics*, Vol. 93, 2003, pp. 9972.

[85] Gavillet, J., Loiseau, A., Journet, C., Willaime, F., Ducastelle, F., and Charlier, J., "Root-growth mechanism for single-wall carbon nanotubes," *Physical review letters*, Vol. 87, No. 27, 2001, pp. 275504.

[86] Louchev, O., Kanda, H., Rosén, A., and Bolton, K., "Thermal physics in carbon nanotube growth kinetics," *The Journal of chemical physics*, Vol. 121, 2004, pp. 446.

[87] Gamaly, E. and Ebbesen, T., "Mechanism of carbon nanotube formation in the arc discharge," *Physical Review B*, Vol. 52, No. 3, 1995, pp. 2083.

[88] Levchenko, I., Ostrikov, K., Keidar, M., and Cvelbar, U., "Modes of nanotube growth in plasmas and reasons for single-walled structure," *Journal of Physics D: Applied Physics*, Vol. 41, 2008, pp. 132004.

[89] Keidar, M., "Factors affecting synthesis of single wall carbon nanotubes in arc discharge," *Journal of Physics D: Applied Physics*, Vol. 40, 2007, pp. 2388.

[90] Keidar, M., Levchenko, I., Arbel, T., Alexander, M., Waas, A., and Ostrikov, K., "Increasing the length of single-wall carbon nanotubes in a magnetically enhanced arc discharge," *Applied Physics Letters*, Vol. 92, 2008, pp. 043129.

[91] Hirth, J. and Pound, G., *Condensation and evaporation: nucleation and growth kinetics*, Progress in materials science, Pergamon Press, 1963.

[92] Abraham, F., *Homogeneous nucleation theory: the pretransition theory of vapor condensation*, Advances in theoretical chemistry: Supplement, Academic Press, 1974.

[93] Knauer, W., "Formation of large metal clusters by surface nucleation," *Journal of applied physics*, Vol. 62, No. 3, 1987, pp. 841–851.

[94] Atkins, P., *Physical Chemistry*, W H Freeman & Co, 1997.

[95] Hihara, T. and Sumiyama, K., "Formation and size control of a Ni cluster by plasma gas condensation," *Journal of applied physics*, Vol. 84, 1998, pp. 5270.

[96] Li, J., Volotskova, O., Shashurin, A., and Keidar, M., "controlling diamter distribution of catalyst nanoparticles in arc discharge," *Journal of Nanoscience and Nanotechnology*, Vol. 11, 2011, pp. 1–6.

[97] Louchev, O., Sato, Y., and Kanda, H., "Morphological stabilization, destabilization, and open-end closure during carbon nanotube growth mediated by surface diffusion," *Physical Review E*, Vol. 66, No. 1, 2002, pp. 011601.

[98] Chapra, S. and Canale, R., *Numerical Methods for Engineers*, McGraw-Hill Higher Education, 2010.

[99] Capitelli, M., Capitelli, F., and Eletskii, A., "Non-equilibrium and equilibrium problems in laser-induced plasmas," *Spectrochimica Acta Part B: Atomic Spectroscopy*, Vol. 55, No. 6, 2000, pp. 559–574.

[100] Bates, D., Kingston, A., and McWhirter, R., "Recombination between electrons and atomic ions. I. Optically thin plasmas," *Proceedings of the Royal Society of London. Series A. Mathematical and Physical Sciences*, Vol. 267, No. 1330, 1962, pp. 297.

[101] Gomes, A., "Criteria for partial LTE in an argon thermal discharge at atmospheric pressure; validity of the spectroscopically measured electronic temperature," *Journal of Physics D: Applied Physics*, Vol. 16, 1983, pp. 357.

[102] Sheppard, E., "Ionizational nonequilibrium and ignition in plasma accelerators," 1994.

[103] Mitchner, M. and Kruger Jr, C., "Partially ionized gases," 1973.

[104] Owano, T., Kruger, C., and Beddini, R., "Electron-ion three body recombination coefficient of argon," *Space Manufacturing 8-Energy and Materials from Space*, Vol. 1, 1991.

[105] Ghia, U., Ghia, K., and Shin, C., "High-Re solutions for incompressible flow using the Navier-Stokes equations and a multigrid method," *Journal of computational physics*, Vol. 48, No. 3, 1982, pp. 387–411.

Appendices

Appendix A

Material properties

A.1 Vapor Pressure

Vapor pressure p_0 is calculated using Eq. A.1 based on the free energy change for evaporation.[36]

$$p_0 = 0.133 exp\left[2.3\left(A - \frac{B}{T_0}\right)\right] \tag{A.1}$$

where, T_0 is the surface temperature. Constants A and B are depends upon heat of vaporization of a material. The corresponding values for the material used in this work are shown in Table A.1.

A.2 Specific heat

The specific heat of the mixture is obtained from the values corresponding to the individual species using mass fraction averaging method 2.6. Since the specific heat varies with temperature, the specific heat of individual species corresponding to the

Material	A	B
Al	11.79	15940
Cu	11.96	16980
Ti	12.50	23230
C	15.73	40030
Ni	12.75	20960
Y	12.43	21970

Table A.1: Constants A and B for vapor pressure calculation using Eq. A.1

given temperature is considered for averaging. Besides this variation, average specific heat $\bar{c_p}$ is used in Eq. (4.10) to simplify the enthalpy calculations. Equation (A.2) shows the relationship.

$$\bar{c_p} = \frac{1}{T_1} \int_0^{T_1} c_p T dT \tag{A.2}$$

When it comes to the numerical implementation, it is cumbersome to perform the above shown calculation at all temperatures in the domain. This is simplified by using the pre-calculated values. The average specific heat is calculated for all the species in wide temperature range and stored in an array. The temperature variation is considered in the intervals of 100 K. Searching the array is made easy this way: for any given temperature the integer value of the quotient can be used to locate the average specific heat. The remainder, if necessary, can be used to linearly interpolate between specific heat corresponding to the current quotient and that of the immediate integer.

A.3 Electrical conductivity

In reality, the arc is generated between the electrodes due to avalanche ionization starting with very few stray electrons accelerated due to the potential difference between the electrodes. This process is not simulated here. The arc is simulated in macroscopic view point. The energy source for the plasma generation in the arc discharges is Joule heating (j^2/σ). Initially the background gas is at room temperature and is not conductive. Hence an initial value, $\sigma_{initial}$, is assumed for electrical conductivity, to start the arc. Here, this initial value is considered equal to the arc current which is specified as input. Once the arc is operational, σ is recalculated at every iteration to obtain its actual value based on the local temperature and species densities according to Eq. (4.2).

During the initial stages of the solution, σ varies quite drastically due to strong coupling to almost all the parameters in the arc region. Anode evaporation depends on the surrounding fluid temperature as well due to conduction from the neutrals. The evaporated species concentration in the arc region influences the thermophysical properties of the fluid and hence its temperature. The temperature and species concentration influences σ and the latter in turn influences the former due to joule heating. Drastic variation in σ between successive iterations, not only demands smaller time step but also destabilized the convergence. In order avoid this instability, the lower limit of electrical conductivity σ_l is decreased exponentially during the initial stages of the solution as given in Eq. (A.3).

$$\sigma_l = \sigma_0 + (\sigma_{initial} - \sigma_0) exp(-t\beta) \tag{A.3}$$

where, σ_0 is the minimum limit considered in this work. t is time and β is a constant to adjust the duration up to which exponential variation is required to get a stable convergence.

The variation of σ along z-direction and at $r = R_a/2$ for case-0 (Table 4.1)is shown in Fig. A.1. The minimum limit, $\sigma_0 = 2$ and the coefficient, $\beta = 0.5$ gives 6 s as the time until which σ_l varies exponentially as shown in Fig. 1.1(a). Figure 1.1(b) shows the evolution of σ from $t = 0.1$ to 20 s. From the its initial value, $\sigma_{initial} = 60$ (S/m), the electrical conductivity self adjusts to its actual value on the upper side and adjusts on the lower side according the exponential variation (Fig.1.1(a)) until t = 6 s. From $t = 10$ s onwards, no variation in σ is observed. The variation of σ at the anode tip is shown in Fig. 1.1(c), which is higher than σ_0.

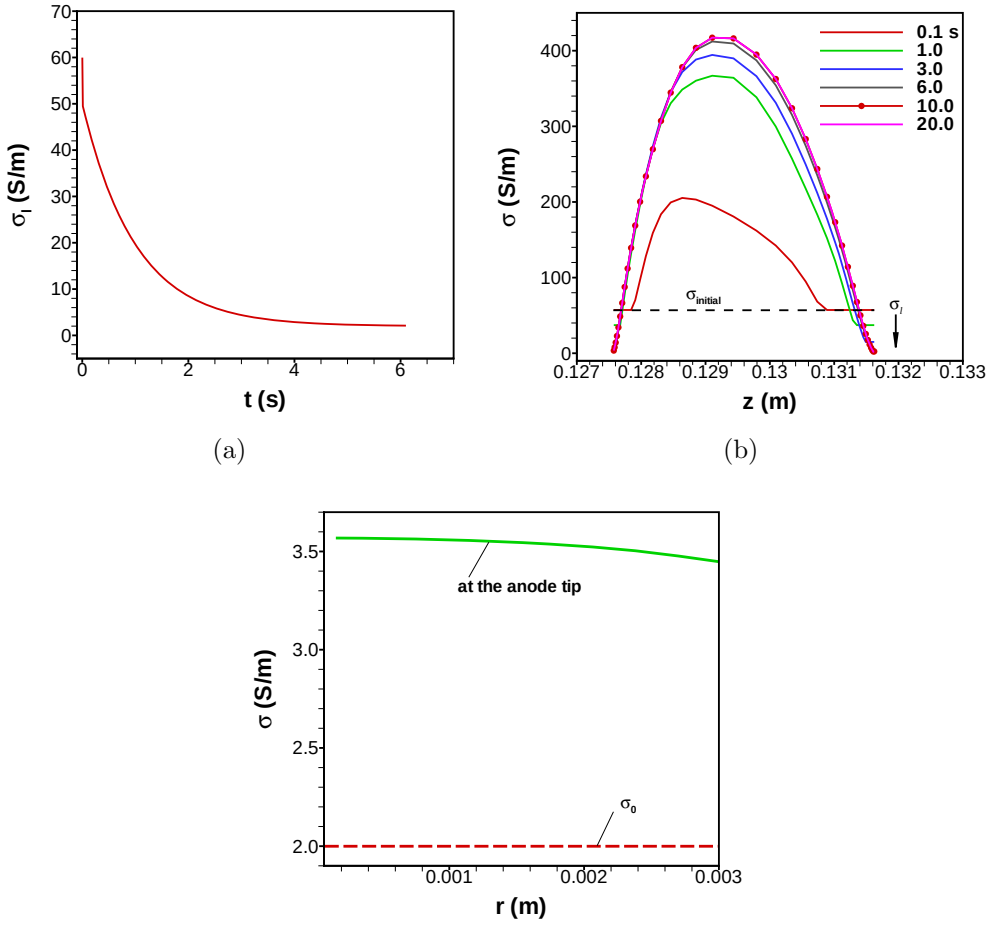

Figure A.1: Variation of electrical conductivity along the z-direction at $r = R_a/2$ for different time instances. Arc current is 60 A, inter-electrode gap 4 mm, and background pressure is 68 kPa. (a) exponential variation of σ_l, (b) evolution of σ with time, and (c) *sigma* at the anode tip.

Appendix B

Collisional Radiative and Saha models

Plasma is said to be in equilibrium if the rate of ionization is balanced by the rate of recombination. The time required to reach equilibrium, τ_i is an important parameter in judging the nature of plasma for the analysis. The characteristic time of ionization equilibrium can be compared with that of characteristic time of change of fluid properties (in particular velocity and temperature), t_c to adapt equilibrium or non-equilibrium ionization calculations. These characteristic times can be approximated beforehand using the relations $t_i = (n_a S_{ac})^{-1}$ and $t_c = d/u$. Where n_a is the number density of atoms, d is characteristic dimension and u is the flow velocity at the point of interest.[99]

Ionization fractions of equilibrium plasmas in local thermodynamic equilibrium can be obtained using Saha equation. For nonequilibrium plasmas, the energy exchange between various excited levels has to be considered to obtain rate coefficients. Collisional radiative (CR) model is widely used for obtaining these rate constants.[100;101;102] CR model combines the collisional and radiative processes to obtain ionization and recombination coefficients.

Here, the ionization fractions obtained using Saha equation are compared with the results from 3 non equilibrium models for the inert gas Argon, in the density range of 10^{18}–10^{24} m^{-3} and temperature range of 3000–27000 K.

B.1 Ionization rate and equilibrium

The ionization rate equation neglecting radiation can be written as

Process	Equation
Excitation to higher level	$e + A_j \rightarrow e + A_k$ $e + A_k \rightarrow e + A_l$
De-excitation to lower level	$e + A_k \rightarrow e + A_j$ $e + A_l \rightarrow e + A_k$
Ionization	$e + A_k \rightarrow e + e + A^+$
Recombination	$e + e + A^+ \rightarrow e + A_k$
Decay	$A_k \rightarrow A_k + h\nu_{jk}$ $A_l \rightarrow A_k + h\nu_{kl}$
Photoionization	$A_k + h\nu_{kc} \rightarrow e + A^+$
Recombination	$e + A^+ \rightarrow A_k + h\nu_{kc}$

Table B.1: Collisional and radiative processes. The excited level of interest is k. The two levels j and l are in the neighborhood of k such that $j < k < l$. A is atom and e is electron. c is continuum (next ion). $\nu_{jk} = \nu_k$ - ν_j.

$$\frac{dn_e}{dt} = n_e n_a S_{ac} - {n_e}^2 n_i S_{ca} \tag{B.1}$$

$$\frac{{n^0}_e {n^0}_i}{{n^0}_a} = \frac{S_{ac}}{S_{ca}} = S\left(k, T_e\right) = \left(\frac{2\pi m_e k_B T_e}{h^2}\right)^{3/2} \frac{2g_i}{g_k} exp\left(-\frac{E_{kc}}{k_B T_e}\right) \tag{B.2}$$

where, the superscript 0 represents equilibrium values, g is the degeneracy of the level, E_{kc} is the energy difference between continuum ion and level k of the atom, m_e is electron mass, and T_e is electron temperature.

B.2 Collisional Radiative (CR) model

The current model is considered from Refs.[102;103]. The main advantage of this model is that it includes the effects of excited states on the ionization and recombination rates without actually solving the continuity equation of different states. Various collisional and radiative processes considered in this model are summarized in Table B.1.

By combining all these processes, the rate equation for excited population can be given as

$$\frac{dn_k}{dt} = n_e^2 n_i \sum_{j \neq k} \left[\frac{(\delta_j - \delta_k) S_{kj}}{S(k, T_e)} - \delta_k S_{ck} \right] - {n_e}^2 n_i S_{ca}$$
$$+ n_e n_i \left[\sum_{l>k} \frac{\delta_l A_{lk} \beta_{lk}}{S(l, T_e)} - \sum_{j<k} \frac{\delta_k A_{kj} \beta_{kj}}{S(k, T_e)} \right]$$
$$+ n_e n_i \left[A_{ck} \beta_{ck} + \sum_{l>k} \frac{A_{lk} \beta_{lk}}{S(l, T_e)} - \sum_{j<k} \frac{A_{kj} \beta_{kj}}{S(k, T_e)} \right] \tag{B.3}$$

where, $\delta_k = (n_k / n_k^0) - 1$ is degree of nonequilibrium at level k, A_{mn} is Einsteins probability for radiative transition, β_{mn} is radiative escape factor, and S_{mn} is excitation or de-excitation rate coefficient. m and n are any two different quantum levels.

The rate equation for electron density is now given by,

$$\frac{dn_e}{dt} = n_e n_a S(1, T_e) \sum_k \chi_k S_{ck} - {n_e}^3 \sum (\chi_k - \psi_k) S_{ck} - n_e^2 \sum_k A_{ck} \beta_{ck} \tag{B.4}$$

where, χ_k and ψ_k are related to δ_k, by the relation $\delta_k = \chi_k(\bar{\beta}, n_e, T_e)\delta_1 + \psi_k(\beta, \bar{n_e}, T_e)$. $\bar{\beta}$ is matrix of radiative escape factors β_{mn}. It has to be noted here that ψ_k is entirely due to radiative processes.

By assuming quasi steady state solution (excited state species are dynamically balanced) and χ_k, ψ_k are independent of plasma state, two sets of equations are available to calculate the coefficients χ_k and ψ_k.

$$0 = \sum_{j \neq k} \left[\frac{(\chi_j - \chi_k) S_{kj}}{S(k, T_e)} - \chi_k S_{ck} \right] + \sum_{l>k} \frac{\chi_l A_{lk} \beta_{lk}}{n_e S(l, T_e)} - \sum_{j<k} \frac{\delta_k A_{kj} \beta_{kj}}{n_e S(k, T_e)} \tag{B.5}$$

$$0 = \sum_{j \neq k} \left[\frac{(\psi_j - \psi_k) S_{kj}}{S(k, T_e)} - \psi_k S_{ck} \right] + \sum_{l>k} \frac{\psi_l A_{lk} \beta_{lk}}{n_e S(l, T_e)} - \sum_{j<k} \frac{\psi_k A_{kj} \beta_{kj}}{n_e S(k, T_e)} + \frac{A_{ck} \beta_{ck}}{n_e} + \sum_{l>k} \frac{\psi_l A_{lk} \beta_{lk}}{n_e S(l, T_e)} - \sum_{j<k} \frac{A_{k,j} \beta_{kj}}{n_e S(k, T_e)} \tag{B.6}$$

By comparing Eqs. (B.4) and (B.1), we can express the rate constants for ionization and recombination as:

$$S_{ac} = S(1, T_e) \sum_k \chi_k S_{ck} \tag{B.7}$$

$$S_{ca} = \sum \left[(\chi_k - \psi_k) S_{ck} + \frac{A_{ck} \beta_{ck}}{n_e} \right] \tag{B.8}$$

The excitation de-excitation coefficients, S_{mn} can calculated using Drawin cross section as follows

$$S_{jk} = 32 f_{jk} \gamma_1 \left(\frac{\pi a_0 E_1^H c}{m_e} \right)^2 \left(\frac{m_e}{2\pi k_B T_e} \right)^{3/2} I_{jk} \tag{B.9}$$

$$S_{kc} = (21.28) \xi_k \gamma_1 \left(\frac{\pi a_0 E_1^H c}{m_e} \right)^2 I_{kc} \tag{B.10}$$

where, a_0 is Bohr radius ($5.292 \times 10^{-11} m$) and E_{1c}^H is ionization energy of Hydrogen atom ($13.6 eV$), γ_1 is an adjustable constant.

The oscillator function

$$f_{kl} = \frac{A_{lk}}{\nu_{kl}^2} \frac{g_l}{g_k} \frac{\varepsilon_0 m_e c^3}{2\pi e^2}$$

and

$$f_{lk} = \frac{g_k}{g_l} f_{kl}$$

$$I_{mn} = \int_1^{\inf} f_m(u, \theta_{mn}) B(u) u du$$

where, $u = E_e/E_{mn}$ and $\theta_{mn} = k_B T_e/E_{mn}$,

$$f(u, \theta_{mn}) = \left(\frac{m_e}{2\pi k_B T_e}\right)^{3/2} exp\left(-\frac{u}{\theta_{mn}}\right)$$

is the normalized energy of the free electron and

$$B(u) = \frac{u-1}{u} ln(1.25\beta_2 u)$$

is the ionization and excitation cross section shape function proposed by Drawin.

B.2.1 Three level CR model

Ground state, first excited state and continuum are considered to evaluate the rate constants. $\chi_1 = 1$ and $\psi_1 = 0$ by definition. From Eqs. (B.5) and (B.6),

$$\chi_2 = \frac{S_{21}}{S_{21} + S_{2c} + A_{21}\beta_{21}/n_e}$$

$$\psi_2 = \frac{-A_{21}\beta_{21} + A_{c2}\beta_{c2} S(2, T_e)}{n_e(S_{21} + S_{2c} + A_{21}\beta_{21}/n_e)}$$

now, Rate constants are given as

$$S_{ac} = S\left(1, T_e\right)\left(\chi_1 S_{c1} + \chi_2 S_{c2}\right)$$

$$S_{ca} = S_{c1} + \left(\chi_2 - \psi_2\right) S_{c2} + \left(A_{c1}\beta_{c1} + A_{c2}\beta_{c2}\right)/n_e$$

B.2.2 Rate constants using multilevel CR model

The equations for rate constants for high density Ar framed by Sheppard[102] and Owano[104] are given by Eqs. (B.11) and (B.12).

$$S_{ca}^{Sheppard} = 8.25 \times 10_{-42} exp\left(\frac{ln(T_e/1000)}{0.6144}\right) \tag{B.11}$$

$$S_{ca}^{Owano} = 3.3 \times 10_{-44}\left(\frac{135300}{T_e} + 2\right) exp\left(\frac{47800}{T_e}\right) \tag{B.12}$$

These equations are framed by fitting curve to the results obtained using multi lvel CR model. Ionization rate constant can be obtained using overall micro-reversibility condition for collisionally dominated plasmas $\frac{S_{ac}}{S_{ca}} = S(1, T_e)$.

B.3 Comparison

The ionization fractions of Ar are obtained using three level CR model and compared with those obtained using the equations given by Sheppard, Owano and Saha. The inputs required for three level CR model: Einsteins probabilities (s^{-1}), $A_{c1} = 5.09 \times 10^5$, $A_{c2} = 9.09 \times 10^5$, $A_{21} = 2.5 \times 10^8$; radiative factors $\beta_{c1} = \beta_{c2} = 1$, $\beta_{21} = 0.01$; degeneracies $g_1 = 1$, $g_2 = 12$, $g_c = 6$; energies $E_1 = 0$ (ground sate), $E_2 = 11.648\ eV$, $E_c = 15.767\ eV$.

The comparisons are shown in Fig. B.1 for four different densities with tem-

perature varying from 3000 K to 27000 K. Figure shows that, for higher densities ($> 10^{22}$) all the models predict the same ionization fractions. While at low densities ($< 10^{22}$), equations given by Sheppard, Owano and Saha gives almost same ionization but much higher than that obtained using three level CR model. This is because; the three equations are suitable for high density plasmas in which ionization is dominated by collisions. So at low densities, 3 level or multilevel CR model is more suitable. But at higher temperatures($> 15000\ K$), even at low densities, the results of three level CR model are close to those obtained using the other three equations.

For high energy laser ablation, the temperature is greater than 15000 K and for arc discharges the density is greater than 10^{22}. Hence, Saha equation is preferred.

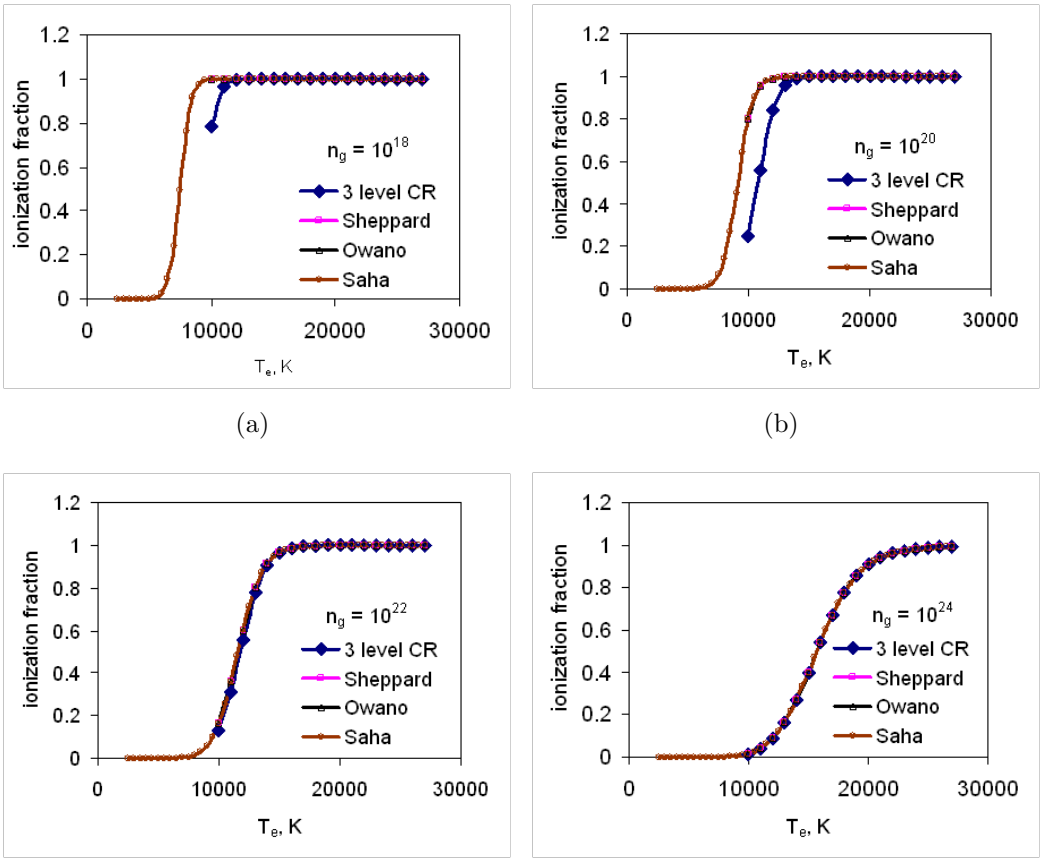

Figure B.1: Comparison of collisional radiative models with Saha ionization. Ionization fraction of Ar obtained using 4 models is compared for temperatures varying form 3000 to 27000 K. Comparison is made for 4 different densities (a)10^{18}, (b) 10^{20}, (c) 10^{22}, and (d) 10^{24} m^{-3}

Appendix C

Euler equation solver

Flow solver: Here the solution scheme and Euler equations and validation results with standard test cases are presented.

C.1 Godunov method

$$\mathbf{U}_t + \mathbf{F}\left(\mathbf{U}\right)_z = \mathbf{R},$$

$$\mathbf{U} = \begin{pmatrix} \rho \\ \rho v \\ E \end{pmatrix}, \quad \mathbf{F} = \begin{pmatrix} \rho v \\ \rho v^2 + p \\ v\left(E + p\right) \end{pmatrix}, \quad \mathbf{R} = \begin{pmatrix} 0 \\ 0 \\ \dot{q} \end{pmatrix} \tag{C.1}$$

The governing equations (C.1), are discretized using Godunov method. The grid convention is shown in Fig. C.1. The resulting set of discretized equations are given below (Eqs. (C.2).

$$\mathbf{U}_i^{n+1} = \mathbf{U}_i^n + \frac{\Delta t}{\Delta z}\left(\mathbf{F}_{i-1/2}^n - \mathbf{F}_{i+1/2}^n\right) + \Delta t \mathbf{R}_i \tag{C.2}$$

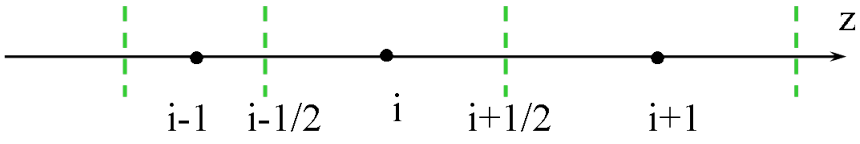

Figure C.1: Grid convention for discretized Euler equations

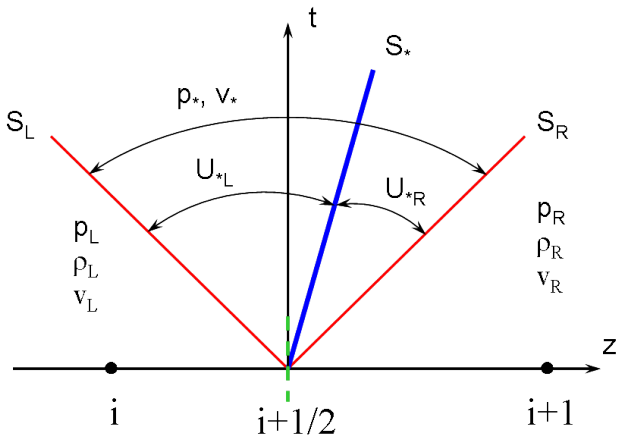

Figure C.2: HLLC approximate Riemann solver showing the left, right and middle wave speeds

C.2 Flux calculations

The interface fluxes are evaluated using HLLC approximate Riemann solver. Figure C.2 shows the, three waves left, right and contact with speeds S_L, S_R and S_* respectively. HLLC fluxed are given in terms of wave speeds and the states U_L, U_{*L}, U_{*R}, and U_R. The wave speed are estimated from the pressure and velocity in the star region. The HLLC fluxes are given in Eq. (C.3) and states are given in Eq. (C.4).

$$\mathbf{F}^{hllc}_{i+\frac{1}{2}} = \begin{cases} \mathbf{F}_L & if \quad 0 \leq S_L, \\ \mathbf{F}_{*L} = \mathbf{F}_L + S_L\left(\mathbf{U}_{*L} - \mathbf{U}_L\right) & if \quad S_L \leq 0 \leq S_*, \\ \mathbf{F}_{*R} = \mathbf{F}_R + S_R\left(\mathbf{U}_{*R} - \mathbf{U}_R\right) & if \quad S_* \leq 0 \leq S_R, \\ \mathbf{F}_R & if \quad 0 \geq S_R. \end{cases} \tag{C.3}$$

$$\mathbf{U}_{*K} = \rho_K \left(\frac{S_K - u_K}{S_K - S_*}\right) \begin{pmatrix} 1 \\ S_* \\ \frac{E_K}{\rho_K} + (S_* - u_K)\left[S_* + \frac{p_K}{\rho_K(S_K - u_K)}\right] \end{pmatrix} \tag{C.4}$$

for $K = L, R$

C.2.1 Pressure-velocity based wave speed

$$S_L = v_L - a_L q_L, S_* = v_*, S_R = u_R + a_R q_R \tag{C.5}$$

$$where,$$

$$q_K = \begin{cases} 1 & if \quad p_* \leq p_K \\ \left[1 + \frac{\gamma+1}{2\gamma}(p_*/p_K - 1)\right]^{1/2} & if \quad p_* > p_K \end{cases}$$

The following procedure is adopted for calculating p_* and v_*.

Primitive variable Riemann solver (PVRS)

$$\begin{aligned} lp_{pv} &= \frac{1}{2}(p_L + p_R) - \frac{1}{2}(v_L - v_R)\bar{\rho}\bar{a}, \\ v_{pv} &= \frac{1}{2}(v_L + v_R) - \frac{1}{2}\frac{(p_R - p_L)}{\bar{\rho}\bar{a}} \\ &where, \\ \bar{\rho} = (\rho_L + \rho_R)/2, \bar{a} &= (a_L + a_R)/2 \end{aligned} \tag{C.6}$$

Two rarefaction Riemann solver (TRRS)

$$\begin{aligned} p_{tr} &= \left[\frac{a_L + a_R - (\gamma-1)/2(v_R - v_L)}{a_L/p_L^x + a_R/p_R^x}\right]^{\frac{1}{x}}, \\ v_{tr} &= \frac{P_{LR}v_L/a_L + u_R/a_R + \frac{2(P_{LR}-1)}{(\gamma-1)}}{P_{LR}/a_L + 1/a_R} \\ &where, \\ P_{LR} = \left(\frac{p_L}{p_R}\right)^x, \; x &= \frac{\gamma-1}{2\gamma} \end{aligned} \tag{C.7}$$

Two shock Riemann solver (TSRS)

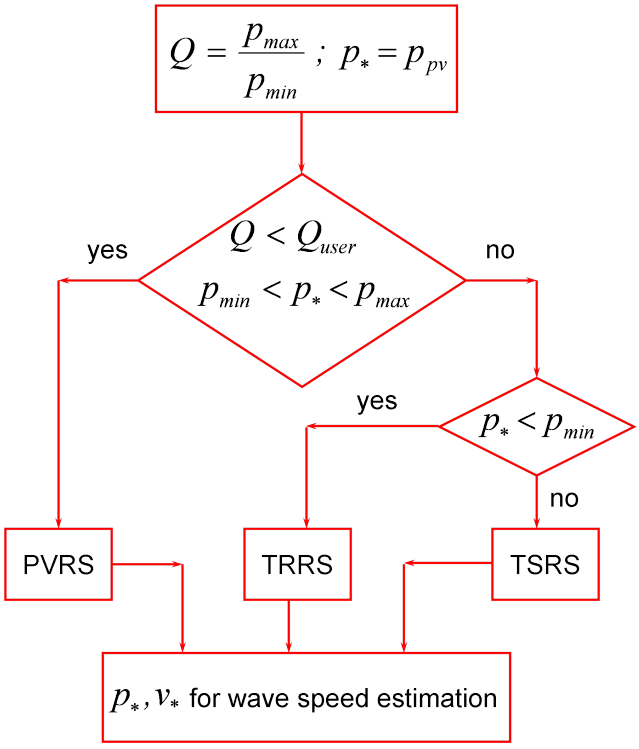

Figure C.3: Adaptive scheme for pressure and velocity calculations in the star region

$$p_{ts} = \frac{g_L(p_0)p_L + g_R(p_0)p_R - \Delta v}{g_L(p_0) + g_R(p_0)},$$
$$v_{ts} = (v_L + v_R)/2 + [(p_{ts} - p_R)g_R(p_0) - (p_{ts} - p_L)g_L(p_0)] \tag{C.8}$$
$$where,$$
$$g_K(p) = \left(\frac{A_K}{p + B_K}\right)^{1/2}, \; p_0 = max(0.p_{pv})$$
$$A_K = \frac{2}{(\gamma+1)\rho_K}, \; B_K = \left(\frac{\gamma-1}{\gamma+1}\right)p_K$$

PVRS, TRRS, and TSRS are combined together to obtain p_* and v_* as shown in Fig. C.3. $p_{min} = min(p_L, p_R)$ and $p_{max} = max(p_L, p_R)$. $Q_{user} = 2$ is considered as suggested in Ref.[38]

The set of discretized equations for mass, momentum, and energy (Eqs. (C.2))are solved used tri-diagonal matrix algorithm (TDMA), also known as Thomas algorithm.

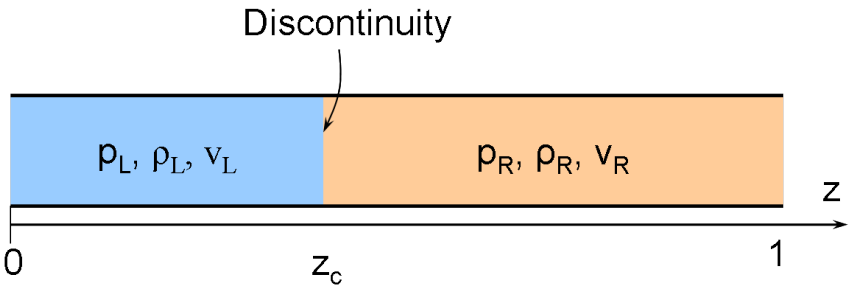

Figure C.4: Riemann problem: The discontinuity is located at z_c at time t = 0.

case	ρ_L	v_L	p_L	ρ_R	v_R	p_R
1	1.0	0.75	1.0	0.125	0.0	0.1
2	1.0	0.0	1000.0	1.0	0.0	0.01

Table C.1: Euler equation solver validation test cases

C.3 Validation

The flow solver is validated with the analytical results for the following test cases. Figure C.4 shows fluid at two different states separated at an arbitrary location z_c. The test cases are given in Table C.1. The comparison of density, velocity, pressure, and specific internal energy with the analytical solution for the two test cases is shown in Figs. C.5 and C.6 respectively.

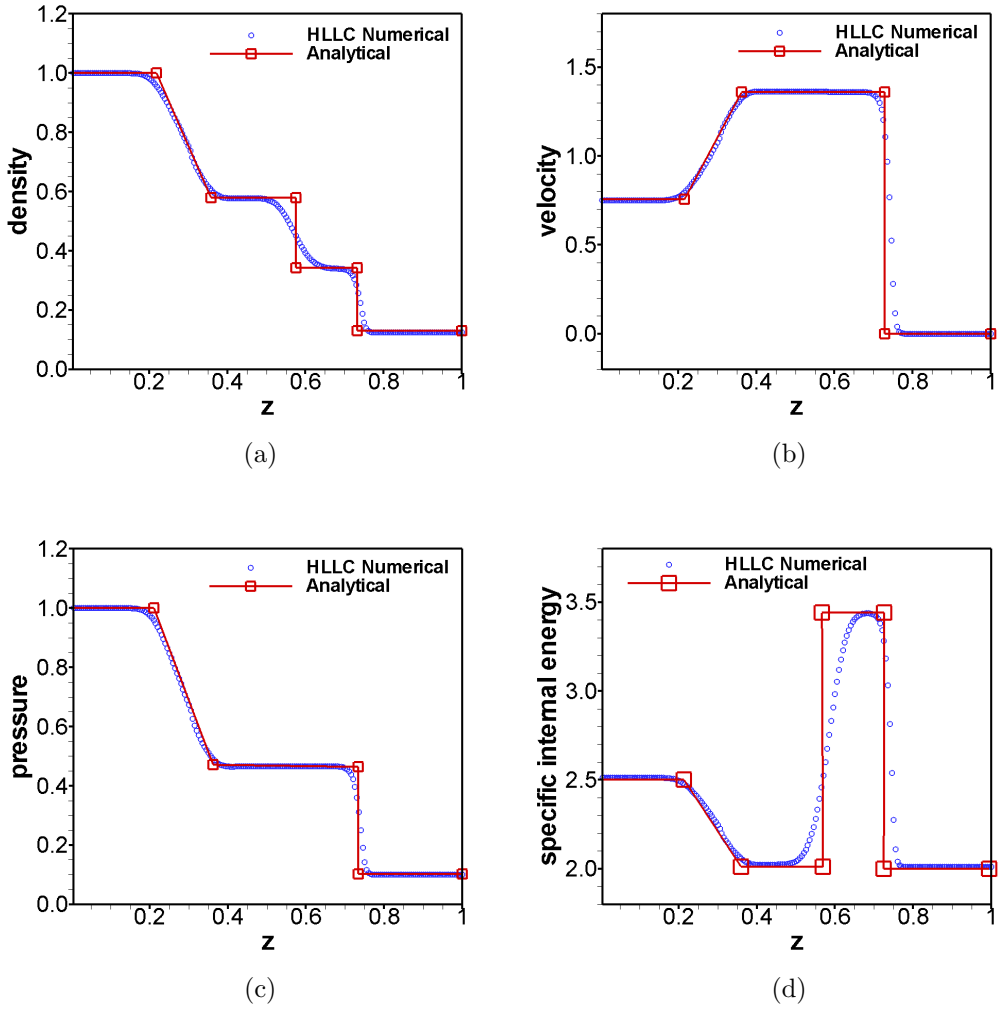

Figure C.5: Validation of Euler equation solver for case-1. At t=0, the discontinuity was at z = 0.3. Solution is shown at t = 0.2

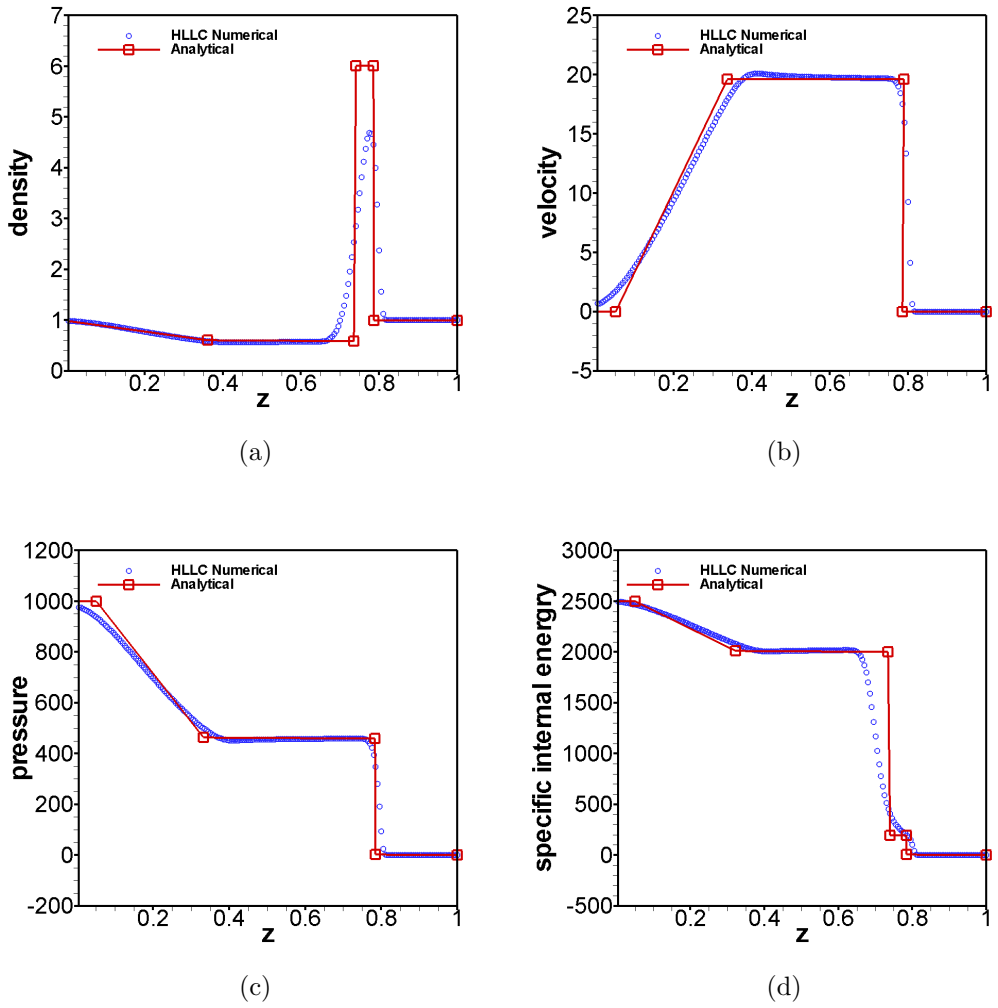

Figure C.6: Validation of Euler equation solver for case-2. At t = 0, discontinuity was at z = 0.5. The solution is shown at t = 0.012

Appendix D

Navier-Stokes equation solver

The general transport equation is given in Eq. D.1.

$$\frac{\partial}{\partial t}(\rho\phi) + \frac{1}{r}\frac{\partial}{\partial r}(r\rho u\phi) + \frac{\partial}{\partial z}(\rho v\phi) = \frac{1}{r}\frac{\partial}{\partial r}\left(r\Gamma_\phi\frac{\partial\phi}{\partial r}\right) + \frac{\partial}{\partial z}\left(\Gamma_\phi\frac{\partial\phi}{\partial z}\right) + S_\phi \qquad \text{(D.1)}$$

Staggered grid is used here as shown in the Fig. D.1. Velocities are represented on staggered grid (red triangle is for radial component and blue square is for axial component)and all the remaining variables are represented by main grid (green circles). Equation (D.2) shows the discretized form of Eq. (D.1) with respect to the main grid. The density on the interfaces is obtained using linear interpolation. All the diffusion coefficients are obtained using harmonic mean.

$$a_{I,J}\phi_{I,J} = a_{I+1,J}\phi_{I+1,J} \; + \; a_{I-1,J}\phi_{I-1,J} \; + \; a_{I,J+1}\phi_{I,J+1} \; + \; a_{I,J-1}\phi_{I,J-1} \; + \; b \qquad \text{(D.2)}$$

where,

$$a_{I+1,J} = D_{i,J}A\left(|P_{i,J}|\right) \; + \; max(-F_{i,J}, 0)$$

$$a_{I-1,J} = D_{i-1,J}A\left(|P_{i-1,J}|\right) \; + \; max(F_{i-1,J}, 0)$$

$$a_{I,J+1} = D_{I,j}A\left(|P_{I,j}|\right) \; + \; max(-F_{I,j}, 0)$$

$$a_{I,J-1} = D_{I,j-1}A\left(|P_{I,j-1}|\right) \; + \; max(F_{I,j-1}, 0)$$

$$a^0_{I,J} = \rho^0_{I,J}\frac{r_I\Delta r_I\Delta z_J}{\Delta t}$$

$$F_{i,J} = (\rho_{i,J} u_{i,J}) r_i \Delta z_J, \;\; F_{i-1,J} = (\rho_{i-1,J} u_{i-1,J}) r_{i-1} \Delta z_J$$

$$F_{I,j} = (\rho_{I,j} v_{I,j}) r_I \Delta r_I, \;\; F_{I,j-1} = (\rho_{I,j-1} v_{I,j-1}) r_I \Delta r_I$$

$$D_{i,J} = \frac{\Gamma_{i,J}}{(\Delta r_I + \Delta r_{I+1})/2} r_i \Delta z_J$$

$$D_{i-1,J} = \frac{\Gamma_{i-1,J}}{(\Delta r_{I-1} + \Delta r_I)/2} r_{i-1} \Delta z_J$$

$$D_{I,j} = \frac{\Gamma_{I,j}}{(\Delta z_J + \Delta z_{J+1})/2} r_I \Delta r_I$$

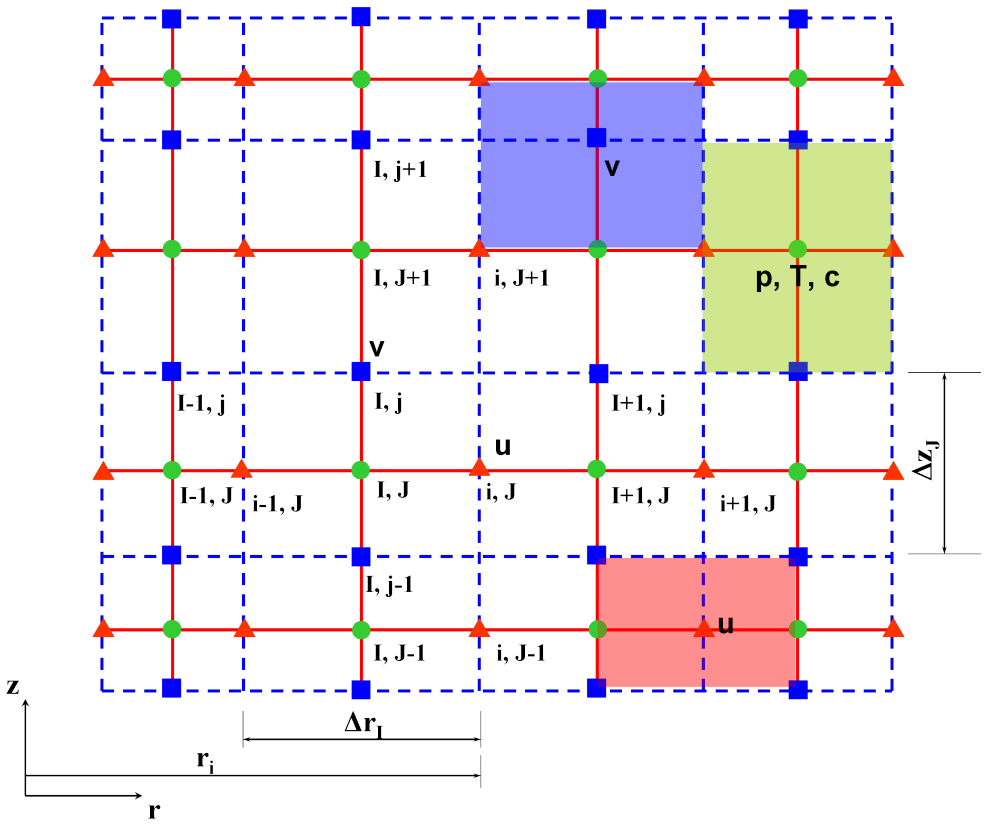

Figure D.1: Staggered grid notation for fluid solver. The red triangles represent grid location for radial velocity (u), blue squares are for axial component of velocity (v), and the green dots are grid location for all the remaining parameters (p,T,c,..). control volumes are shown by the respective color shading

$$D_{I,j-1} = \frac{\Gamma_{I,j-1}}{(\Delta z_{J-1} + \Delta z_J)/2} r_I \Delta r_I$$

$$P_{i,J} = \frac{F_{i,J}}{D_{i,J}} \; and \; so \; on$$

$$A(|P|) = \begin{cases} 1 - 0.5\,|P| & central\ difference \\ 1 & upwind \\ max(0, (1 - 0.1\,|P|)^5) & power\ law \end{cases}$$

D.1 SIMPLER Algorithm

The discretized momentum equations (Eqs. (4.8) and (4.9)) are given in Eqs. (D.3). The velocities are then substituted in discretized form of continuity equation(Eq. (4.7)) to obtain discretized equation for pressure. The pseudo velocities ($\hat{u}$and $\hat{v}$) exist in the source term b of the discrete pressure equation, Eq. (D.4). Further details are found in Ref.[60]

$$u_{i,J} = \underbrace{\left(a_{i-1,J}u_{i-1,J} + a_{i+1,J}u_{i+1,J} + a_{i,J-1}u_{i,J-1} + a_{i,J+1}u_{i,J+1}\right)/\left(a_{i,J}\right)}_{\hat{u}_{i,J}}$$

$$+ d_{i,J}\left(p_{I,J} - p_{I+1,J}\right) \qquad \text{(D.3a)}$$

$$v_{I,j} = \underbrace{\left(a_{I-1,j}v_{I-1,j} + a_{I+1,J}v_{I+1,J} + a_{I,j-1}v_{I,j-1} + a_{I,j+1}v_{I,j+1}\right)/\left(a_{i,J}\right)}_{\hat{v}_{i,J}}$$

$$+ d_{I,j}\left(p_{I,J+1} - p_{I,J}\right) \qquad \text{(D.3b)}$$

where,

$$d_{i,J} = \frac{A_{i,J}}{a_{i,J}}, \qquad d_{I,j} = \frac{A_{I,j}}{a_{I,j}}, \; ...$$

A is the area of the control volume face and the coefficient a is obtained as per Eq.(D.2).

$$a_{I,J}p_{I,J} = a_{I+1,J}p_{I+1,J} + a_{I-1,J}p_{I-1,J} + a_{I,J+1}p_{I,J+1} + a_{I,J-1}p_{I,J-1} + b \quad \text{(D.4)}$$

where,

$$a_{I+1,J} = \rho_{i,J}d_{i,J}r_i\Delta z_J,\ a_{I-1,J} = \rho_{i-1,J}d_{i-1,J}r_{i-1}\Delta z_J$$

$$a_{I,J+1} = \rho_{I,j}d_{I,j}r_I\Delta r_I,\ a_{I,J-1} = \rho_{I,j-1}d_{I,j-1}r_I\Delta r_I$$

$$b = \frac{\rho^0_{I,J} - \rho_{I,J}}{\Delta t} + (\rho_{i-1,J}r_{i-1}\Delta z_J\hat{u}_{i-1,J} - \rho_{i,J}r_i\Delta z_J\hat{u}_{i+1,J}) + (\rho_{I,j-1}r_I\Delta r_I\hat{v}_{I,j-1} - \rho_{I,j}r_I\Delta r_I\hat{v}_{I,j})$$

The linear equations (D.2) and (D.4) are solved using Gauss-Seidel line-by-line method. Axial direction sweep is considered here. The Tridiagonal matrix along each line is solved using Thomas algorithm, which is a direct method.

D.1.1 Algorithm

1. velocity is considered from the initial condition
2. $\hat{u}$ and $\hat{v}$ are evaluated using Eq. (D.3)
3. pressure equation, Eq. (D.4) is solved to obtain p at all grid points
4. momentum equations, Eq. (D.3) are solved using p to obtain approximate velocities u^* and v^*
5. Equation (D.4) is solved, this time, using u^* and v^* instead $\hat{u}$ and $\hat{v}$. The obtained solution of pressure is called pressure correction, p'
6. The velocity is corrected using the relations $u_{i,J} = u^*_{i,J} + d_{i,J}$ ($p_{I,J}$ - $p_{I+1,J}$) and $v_{I,j} = v^*_{I,j} + d_{I,j}$ ($p_{I,J}$ - $p_{I,J+1}$)

7. steps 2–6 are repeated until convergence is met

D.2 Solution steps

Here segregated approach is used, to avoid the complications associated with source terms arising due to electromagnetic fields in energy equation. The main difficulty arises from the evaluation of electrical conductivity which is dependent on neutral and ion densities and temperature. Initially the electrical conductivity is assumed to a constant value throughout the domain and solved for electric potential. Then the electrical conductivity is updated to its actual values using the existing species density and temperature distribution.

1. Thermophysical properties are evaluated with the existing values of temperature and species density
2. velocity field is obtained using SIMPLER algorithm
3. evaporation rate is calculated
4. species transport equations are solve to find the mass fraction distribution of all the neutral species
5. SAHA equation is solved to obtain the ion density of different species and electron density
6. curent continuity is solved to obtain the potential field. current flux and magnetic field distribution are obtained.
7. Energy equation is solved to obtain the temperature distribution
8. density is updated

Figure D.2 shows the comparison of flow field inside lid driven unit cavity with the results given by Ghia et al.[105]. The comparison of X and Y velocity components is shown in Fig. D.3. Central difference and power law schemes are compared with the values given by Ghia et al.[105]. It has to noted here that the cylindrical coordinate equations in the solver are reduced to Cartesian coordinates by equating $r = 1$ in the governing equation, Eq. (D.1) and deactivating $\tau_{\theta\theta}$ from the radial momentum Eq. (4.8).

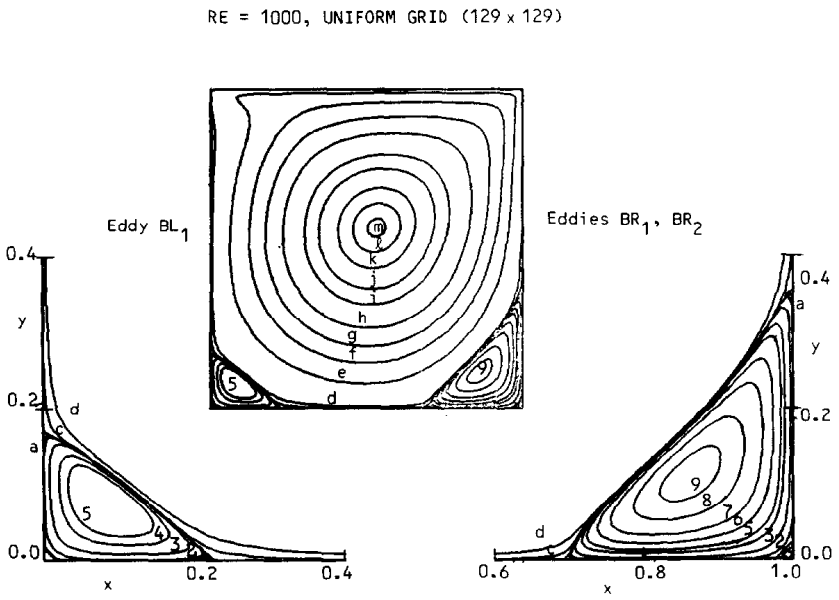

(a)

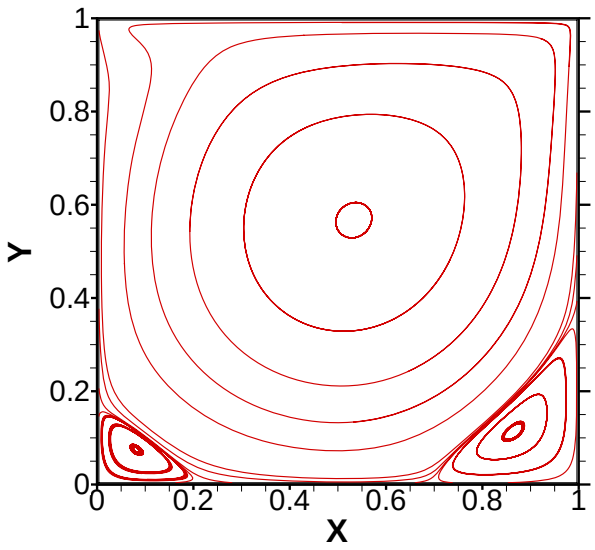

(b)

Figure D.2: Velocity contours in lid driven cavity with Re = 1000. Velocity contours are compared with those from Ref[105] (a)velocity contours from reference (b) contours from present solver

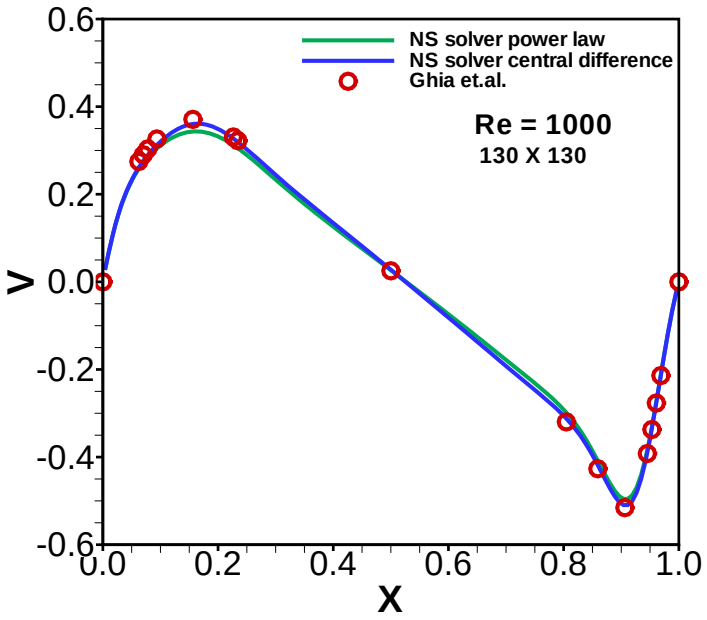

(a)

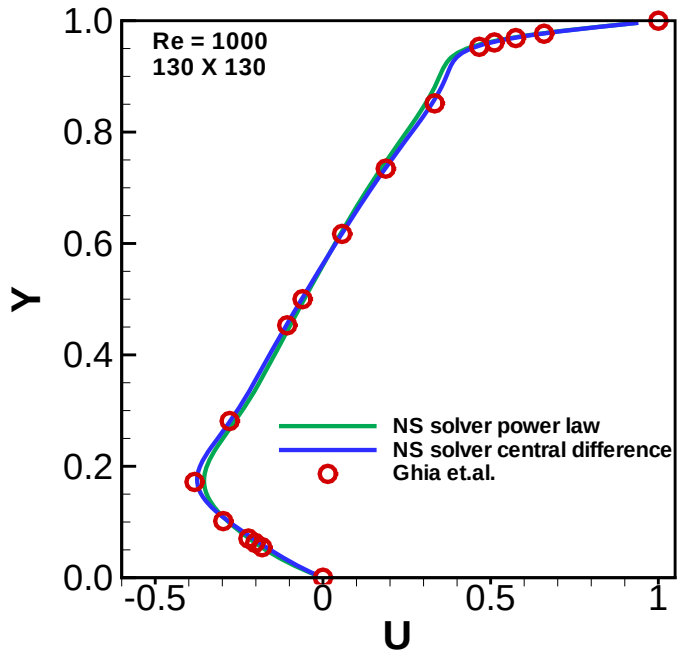

(b)

Figure D.3: Validation of NS equation solver: Lid driven unit cavity with Re = 1000. The central and power law schemes are compared with the results of Ref[105] (a) comparison of Y-velocity component along a line passing through the center of cavity and normal to Y direction (b) comparison of X-velocity component along a line passing through the center of cavity and normal to X direction